Tidal phase differences in multi-branch systems and their effect on salt intrusion

Johannes de Wilde

Tidal phase differences in multi-branch systems and their effect on salt intrusion

by

Johannes de Wilde

in partial fulfilment of the requirements for the degree of

Master of Science

in Civil Engineering

at the Delft University of Technology (TU Delft),

to be defended publicly on Friday, March 22, 2024 at 11:00 AM.

Student number:	4715535	
Project duration:	June 26, 2023 – March 22, 2024	
Chair committee:	Prof. Dr. J. D. Pietrzak,	Delft University of Technology
Thesis committee:	Dr. Ir. W. M. Kranenburg,	Delft University of Technology & Deltares
	Dr. Y. Huismans,	Delft University of Technology & Deltares
	Dr. Ir. B. C. van Prooijen,	Delft University of Technology
	Ir. G. G. Hendrickx,	Delft University of Technology

Cover: Hollandsche IJsselkering (Rijkswaterstaat, 2021)

Preface

This research concludes my Master of Science program in Hydraulic Engineering at the Delft University of Technology. This thesis was conducted at the knowledge institute Deltares. I am grateful for the opportunity to do my thesis at this company and I enjoyed the shared enthusiasm for hydrodynamics.

This thesis would not be possible without the help of my graduation committee. First, I would like to thank Wouter Kranenburg for his regular help. You gave me lots of new insights during my thesis and your feedback and enthusiasm were really wonderful. Thank you Ymkje Huismans for the time you made for me, your creative ideas and the feedback you gave. I appreciate the meetings we had with the three of us, where I learned a lot and was challenged to thrive. Next, I want to thank Julie Pietrzak for chairing the committee, for her great input during the committee meetings and for the time you took to help me improve my report. Thank you Gijs Hendrickx for the ideas you shared during the committee meetings and the time you took to review and help me write my report. Thanks to Bram van Prooijen for your insights during the latest committee meetings.

I want to thank the Hydrodynamics and Forecasting department at Deltares for their interest in my project. At last, I want to thank my mom and dad for always cheering for me and your endless support and love. I want to thank my brother, friends and roommates as I am blessed with your support!

Johannes de Wilde
Delft, March 2024

Abstract

The Hollandsche IJssel plays an important role in the freshwater provision of the province Zuid-Holland. Consequently, for Rijkswaterstaat it is key that salt intrusion is minimal in the Hollandsche IJssel. Recent studies noted that salt intrusion in the Hollandsche IJssel is limited due to a phase difference between tidal velocities in the main channel, the Nieuwe Maas, and the side channel, the Hollandsche IJssel. Earlier research investigated the impact of phase differences between branches and found it can lead to increased dispersion in the main channel, through a process known as tidal trapping. At the same time, this phase difference can prevent the saltiest water from entering the side channel, as was found at the Hollandsche IJssel. Because of this role, it is relevant to find out how this phase difference may be influenced by sea level rise, more extreme river discharges and particularly how it depends on the geometry of the main and the side channels. Especially the latter could help Rijkswaterstaat to minimize salt intrusion at locations relevant to freshwater intake, such as the Hollandsche IJssel.

The main objective of this thesis is to investigate how the geometry of the side and main channel influences the tidal phase difference between these two channels, and how this may impact the salt dispersion in the side channel. For this, an analytical model is developed describing harmonic wave propagation in multi-branch systems and this is used next to results from a 3D numerical model for the Rhine Meuse Delta (RMM3D). First, the influence of changes in geometry and forcing is systematically investigated for a network containing a single junction. This shows that the length and depth of the side channel are the most significant variables. The depth is one of the main variables impacting friction, which governs the type of wave which can form in the system. A decrease in friction allows a wave to transform into a standing wave pattern as the return wave becomes more important, while increased friction transforms it into a propagating wave. The length also controls the type of wave which can form as it determines the distance along which the friction can work. Additionally, the length also governs potential resonance in the side channel.

Next, the phase differences of the M2, M4 and M6 tide are determined for the junction with the Hollandsche IJssel in the Rhine Meuse Delta (RMD) based on the RMM3D model. The main tidal constituent regarding tidal trapping was found to be M2. However, this does not fully represent the time difference between flow reversal at the Hollandsche IJssel and the Nieuwe Maas, which was found to be around 75 minutes. Additionally, the phase difference at the Lek was investigated. For the M2 tide at the Hollandsche IJssel and Lek, a phase difference of 55° and 31° was found, respectively. These phase differences prevent salt intrusion in the respective side channels. The inflow of the side channels starts while the main channel still flows to the sea during the ebb. At this moment, the salt concentrations in the main channel have already returned to background levels. So, a larger phase difference allows for more fresh water to enter. Additionally, an earlier outflow of the side channel prevents more of the saltiest water of the main channel from entering at the end of the flood. Thus, a larger phase difference at the Hollandsche IJssel is more effective against salt intrusion.

Subsequently, the multi-branch RMD is modelled with the analytical model. This is used to investigate possibilities to further limit salt intrusion at the previously mentioned junctions by changing the phase difference. A first estimate of the impact of the phase difference on the salt intrusion in the side channel is made by assuming the phase difference solely shifts the discharge signal of the side channel. So, based on the salt concentrations in the Nieuwe Maas and the inflow patterns of the Hollandsche IJssel and Lek, the first estimate showed the possibility of reducing the salt transport into the side channel by increasing the phase difference.

Consequently, a comparison is made between the Hollandsche IJssel and the Lek to explore the necessary adjustments in geometry for a 10-minute increase in phase difference. For the Hollandsche IJssel, the only possibility is reducing the length by 10 km, as the current phase difference between the water level and discharge in the Hollandsche IJssel is already close to 90°. The first estimate of the salt intrusion shows a reduced salt flux into the Hollandsche IJssel up to 25% on average. The

Lek only required a 4 km reduction in length to achieve an increase of 10 minutes in phase difference and showed a 15% decrease of the salt flux into the Lek. The gradient of the salt concentrations in the Nieuwe Maas can explain the difference in salt flux reduction. At the Hollandsche IJssel, the salt concentrations increase more quickly compared to the Lek. So, a shift in the discharge results in a larger decrease in salt concentration entering the Hollandsche IJssel compared to the Lek.

For the Lek, more possible solutions were found to increase the phase difference by 10 or even 20 minutes. Additionally, it is expected that the change in phase difference at the Lek has a significant impact on the salt dispersion in the Nieuwe Maas, while it is expected to be limited for the Hollandsche IJssel. This is caused by the four times larger volume of the Lek and the fact that the current phase difference of the Lek is not located near the maximum value of the dispersion coefficient for tidal trapping. So, an increased phase difference of 10 minutes at the Lek increases the dispersion coefficient for tidal trapping by 19%.

Contents

List of Figures

List of Tables

Nomenclature

List of acronyms

Abbreviation	Definition
HIJ	Hollandsche IJssel
KWA	Klimaatbestendige Wateraanvoer
NM	Nieuwe Maas
PSU	Practical salinity unit
RMD	Rhine Meuse Delta
SJN	Single junction network

List of symbols

Symbol	Definition	Unit
A	Cross section	[m^2]
A_c	Conveyance cross-section	[m^2]
A_{tide}	Tidal amplitude	[m]
B	Width of the free surface	[m]
C^+	Integration constant in positive direction	[-]
C^-	Integration constant in negative direction	[-]
c	Wave speed	[m/s]
c_0	Wave speed without friction	[m/s]
c_f	Friction coefficient	[-]
d	Depth	[m]
F_R	Resistance force per unit length	[N/m]
F_s	Salt flux	[kg/s]
f	Parts of the rewritten four-pole equations	[rad]
f_θ	Part dependent on phase difference of dispersion coefficient of MacVean and Stacey (2011)	[-]
g	Gravitational acceleration	[m/s^2]
$K_{trap,A}$	Dispersion coefficient for tidal trapping by MacVean and Stacey (2011)	[m^2/s]
$K_{trap,D}$	Dispersion coefficient for tidal trapping by Okubo (1973)	[m^2/s]
k	Wave number	[rad/m]
k_0	Wave number without friction	[rad/m]
k_{trap}	Characteristic residence time of substance in the trap	[s^{-1}]
L	Length	[m]
l	Length	[m]
P_w	Wet perimeter	[m]
P	Propagation constant	[rad^2/m^2]
p	Propagation constant	[rad/m]
Q	Discharge	[m^3/s]
$\hat{Q}$	Amplitude discharge	[m^3/s]
$\tilde{Q}$	Complex amplitude discharge	[m^3/s]
R	Hydraulic radius	[m]
r	Ratio trap volume to to main channel volume	[-]
S	Salinity	[mg/L]

Symbol	Definition	Unit
s_0	Tidally averaged cross-sectional salinity	[PSU]
T	Tidal period	[s]
t	Time	[s]
$\hat{U}_m$	Velocity amplitude in the main channel	[m/s]
U	Cross-sectionally averaged flow velocities	[m/s]
V	Volume	[m^3]
x	Stream wise component	[m]
$\tilde{Z}$	Complex variable	[m]
α	Phase lag	[rad]
ϵ	Ratio of salt mass trapped in the side channel compared to the main channel	[-]
η	Fluctuations of the water level	[m]
$\hat{\eta}$	Amplitude of the fluctuations of the water level	[m]
$\tilde{\eta}$	Complex amplitude of the fluctuations of the water level	[m]
θ	Phase difference	[$^\circ$]
κ	Factor for linearized resistance	[s^{-1}]
λ	Wave length	[m]
ρ	Density	[kg/m^3]
σ	Ratio of resistance to inertia	[-]
τ	Shear stress	[N/m^2]
ϕ	Phase	[$^\circ$]
ω	Tidal radian frequency	[s^{-1}]

List of subscripts

Subscript	Definition
f	Fluvial
m	Main channel
s	Side channel
t	Tidal

Part I

Background information and literature

1 Introduction

Estuaries form prime locations for human settlement. Currently, about 60% of the worlds population lives on the coast and along estuaries (Lindeboom, 2002). The protected coastal waters of estuaries allow for economic development through harbours and transport routes. In addition, estuaries form breeding and nursing grounds, sustaining a high level of food production (Mateus et al., 2008), combined with freshwater availability by rivers.

An estuary forms a region where inland freshwater systems exchange water with a saltier marine environment (Nijs et al., 2011), allowing salt water to reach further inland. Salt intrusion impacts multiple aspects of society, for instance, agriculture, nature and drinking water. A higher salinity impacts agriculture by a significant decrease in yield or it prevents the growth of certain crops. The saltwater can reach agricultural grounds via irrigation or groundwater. The same problems arise in nature. Flora and fauna shifts occur as species used to freshwater are exposed to more saline water. The problems with drinking water occur when it is extracted from surface water, as it can only be extracted when the salinity concentrations are low (TwynstraGudde and HydroLogic, 2019).

In the future salt intrusion will be further impacted by climate change. Sea level rise will shift the location of the transition between fresh and saltwater upstream. This means salt intrusion will reach further inland and impact a larger area. Additionally, river discharges are also impacted by climate change. Climate change will cause more extreme river discharges. Thus even lower discharges can occur, which offer less counterpressure against the incoming tide. Again this allows saltwater to travel further inland (TwynstraGudde and HydroLogic, 2019). Consequently, it is important to understand the causes of salt intrusion and how it can be prevented.

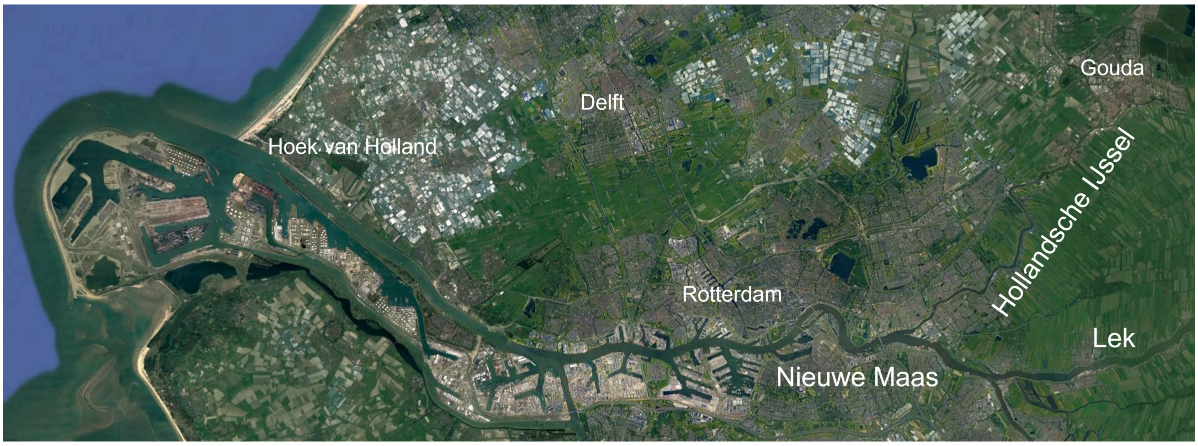

Figure 1.1: Overview Hollandsche IJssel. Figure retrieved from Google Earth Pro (2022)

Salt intrusion is a worldwide challenge faced in many deltas and estuaries, as is the case for the Rhine Meuse Delta (RMD). The Hollandsche IJssel plays an important role in the freshwater provision of the province Zuid-Holland. Consequently, for Rijkswaterstaat it is key that salt intrusion is minimal in the Hollandsche IJssel. Earlier studies noted that currently, salt intrusion in the Hollandsche IJssel is limited due to a phase difference between tidal velocities in the main channel, the Nieuwe Maas and the side channel, the Hollandsche IJssel (Kuijper, 2015, 2016; Laan et al., 2021). This phase difference can prevent the saltiest water from entering the side channel. Because of this role, it is relevant to find out how this phase difference may be influenced by sea level rise, more extreme river discharges and particularly how it depends on the geometry of the main and the side channels. Especially the impact of geometry could help Rijkswaterstaat minimize salt intrusion at locations, such as the Hollandsche IJssel.

To better understand the origin of salt intrusion in the Rhine Muese Delta, it is useful to understand what type of estuary it is. Estuaries are divided into different categories and they can be classified based on their circulation and stratification patterns. Hansen and Rattray Jr. (1966) divided them into four categories: salt-wedge, with a large river discharge and weak tidal forcing; strongly satisfied, with moderate to large river discharge and weak to moderate tidal forcing; partially stratified, with weak to moderate river discharge and moderate to strong tidal forcing; and well mixed, with weak river discharge and strong tidal forcing.

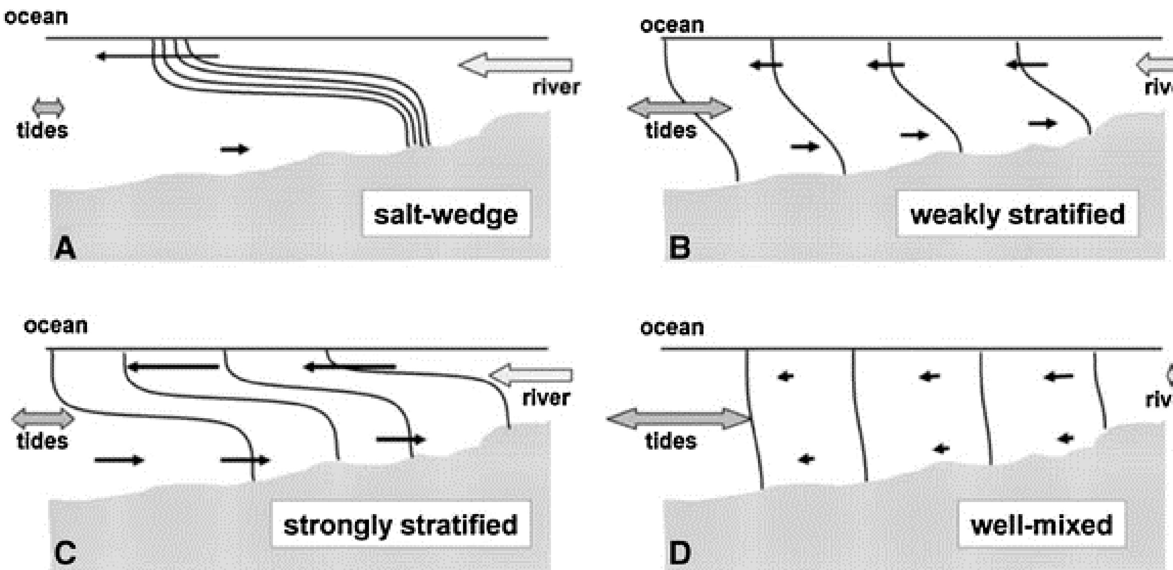

Figure 1.2: Estuary classification by circulation and stratification patterns. **(a)** Large river discharge and weak tidal forcing result in salt-wedge estuaries. **(b)** Weakly stratified or partially stratified estuaries result from moderate to strong tidal forcing and weak to moderate river discharge. **(c)** Moderate to large river discharge and weak to moderate tidal forcing result in strongly stratified estuaries. **(d)** Strong tidal forcing and weak river discharge result in vertically mixed estuaries. Figure retrieved from Valle-Levinson (2010)

The Rhine Meuse Delta is located in the west of the Netherlands, and it is the region where the rivers Rhine and Meuse reach the North Sea, see figure 1.3. The RMD can generally be classified as strongly stratified to partially stratified (Kranenburg et al., 2022). However, during above-average river discharge, the Rhine Meuse Delta shows a distinct salt wedge (Nijs et al., 2011). At the entrance of the estuary, the salt intrusion is dominated by an exchange flow (Nijs et al., 2011). Kranenburg et al. (2022) also noted that an estuary exchange flow dominates downstream, but in addition, found that tidal dispersion dominates upstream in the Nieuwe Maas.

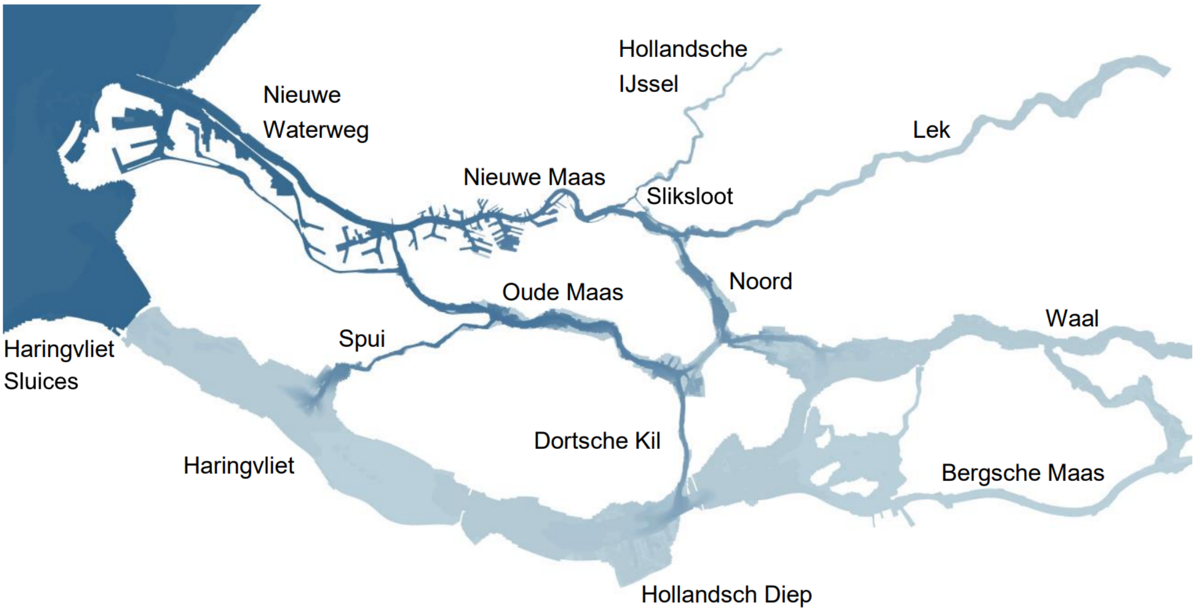

Figure 1.3: Overview of the Rhine Meuse Delta. Figure retrieved from Tiessen et al. (2016)

The Rhine Meuse Delta has two connections to the sea, the Nieuwe Waterweg and the Haringvliet. The main connection to the sea is the Nieuwe Waterweg, which is practically always open. This exit is only blocked when the Maeslant Barrier closes. The Haringvliet is closed off at the seaside with the Haringvliet Sluices. The opening and closure of the Haringvliet Sluices depend on the river discharge in the Rhine at Lobith. During high discharges and thus high water levels in the rivers, the sluices open and discharge the excess water. During periods of low river discharges, the Haringvliet Sluices remains closed to store as much water as possible (Rijkswaterstaat, n.d.[a]). In addition, it steers fresh water to the north side of the RMD, which offers additional counterpressure to reduce salt intrusion into the Rhine Meuse Delta during low river discharges (Friocourt et al., 2020).

The Rhine Meuse Delta is, in the present day, mostly an engineered river delta. The rivers are guided to the sea by dikes and embankments. The water level and discharge are controlled via many weirs, locks and pumping stations. This keeps waterways usable for shipping during dry periods. Additionally, it allows for a well-managed freshwater distribution across the Netherlands. (Rijkswaterstaat, n.d.[b]).

The freshwater availability is very important. The area surrounding the Rhine Meuse Delta is the most densely populated and intensively used region of the Netherlands (Huismans et al., 2017). In Zuid-Holland, the Hollandsche IJssel plays a key role in the freshwater provision. Additionally, it has an important function in the water supply and disposal for the surrounding water authorities (Werkgroep Slim Watermanagement, Rijn-Maasmonding, 2019). The same can be said about the Lek. It is an important part of the freshwater provision for its surrounding water authorities, including multiple drink water inlets (Werkgroep Slim Watermanagement, Rijn-Maasmonding, 2021).

The current functions of the Hollandsche IJssel and Lek make salt intrusion in those areas unwanted. As mentioned previously, salt intrusion is dominated by different processes depending on the location in the Rhine Meuse Delta. The two main processes of estuary exchange flow and tidal dispersion are further elaborated.

At the mouth of the Rhine Meuse Delta, the salt intrusion is mainly driven by an estuary exchange flow, which is predominantly made up of gravitational circulation. This is an inflow of denser saltwater at the bed and an outflow of freshwater at the surface, caused by density differences. An exchange flow causes strong stratification, as the interface between fresh and saltwater becomes small and the salinity gradient becomes large.

Stratification can be decreased by turbulence. This mixes the salt and fresh water in the water column and decreases the salinity gradient. Turbulence can be generated at the bottom or by a velocity gradient over the vertical which introduces shear stresses. Thus, the amount of stratification is dependent on which process is dominant. A salt wedge can form in an estuary when the river discharge is dominant, as the river is a major source of buoyancy and an estuary becomes well mixed when mixing forces like the tide become dominant (Simpson, 1997).

Further inland in the Rhine Meuse Delta, tidal dispersion acts to transport salt into the estuary. Tidal dispersion is among other things caused by the presence of floodplains, harbours and side channels (Fischer, 1976). The dispersion of salt in the main channel caused by harbours and side channels is called tidal trapping. The main driver of tidal trapping is a phase difference between the tidal velocities in the side and main channel.

The impact of side channels in estuaries on the dispersion of salt or other substances has been a research topic before. Okubo (1973) developed a mathematical model to quantify the dispersion due to tidal trapping. This method was a parametrization and does not explicitly represent the physics of the exchange process, but showed reasonable agreement with observed values (Okubo, 1973). MacVean and Stacey (2011) followed up on the research and improved the formulation for tidally forced scenarios. Both of them focused on the dispersion of salt in the main channel. In addition, the phase difference also prevents the saltiest water from entering the side channel, limiting salt intrusion, as was found at the Hollandsche IJssel.

Both Okubo (1973) and MacVean and Stacey (2011) included the geometry of the side and main channel in a broad manner. They used a parameter related to the ratio of side channel volume to main channel volume. Thus, the impact of the length, width and depth of the side and main channel is not individually discussed.

The main objective of this study is to investigate the impact of side and main channel geometry on the phase difference driving tidal trapping, and how this impacts the salt dispersion in the side channel. For this, an analytical model is developed, which describes the propagation of a harmonic wave in a multi-branch system. First, the impact of changes in the geometry and forcing are systematically investigated in a network containing a single junction. So, we can investigate how the geometry influences the flow characteristics and the tidal phase difference between a side and main channel. With the results of a more detailed numerical model of the Rhine Meuse Delta (RMM3D), the phase difference is determined for the junctions Hollandsche IJssel, Nieuwe Maas and the Lek, Nieuwe Maas. In addition, data analysis on these model results tries to derive connections between the phase difference and its impact on salt intrusion. Our objective is to investigate how the tidal phase differences influence salt intrusion in the multi-branch system of the Rhine Meuse Delta. Finally, the RMD is modelled with the analytical model to investigate if it is possible to alter the phase difference to minimize the salt intrusion in a side channel.

This thesis is organized as follows. Chapter 2 and 3 present the relevant literature, which includes the theory of tidal trapping and the derivation of the equations for the analytical model. Next, the development of the analytical model is presented in chapter 4, followed in chapter 5 by the results of changes in the geometry and forcing on the phase difference in a single junction network. Chapter 6 gives additional information about the Rhine Meuse Delta and what is currently known about salt intrusion in the Hollandsche IJssel. In chapter 7 the phase differences at the Hollandsche IJssel are determined. Chapter 8 describes the modelling of the Rhine Meuse Delta in the analytical model and how this is used to optimize the phase difference. Next, the impact of the phase difference on salt intrusion is determined in chapter 9. At last, the discussion and conclusion are treated in sections 10 and 11. Each chapter contains a conclusion stating the most important findings from that chapter.

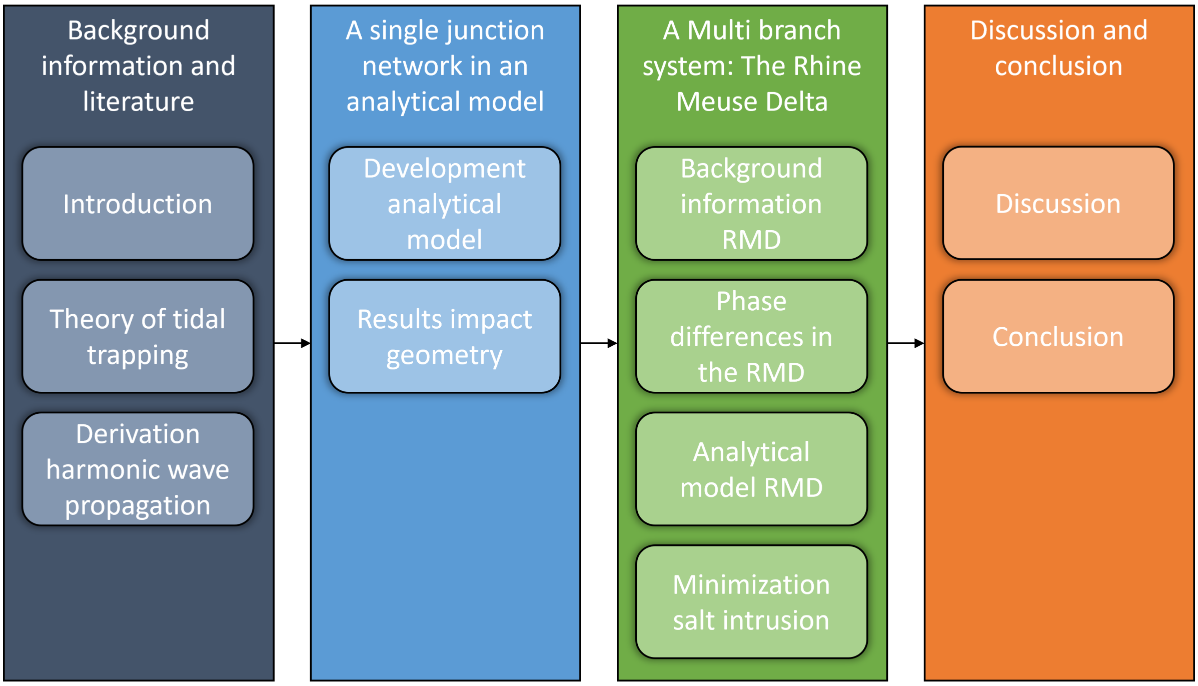

Figure 1.4: Reading guide

2 Theory of tidal trapping

This chapter describes the mechanism of salt intrusion by tidal trapping. Furthermore, it gives an overview of two descriptions of dispersion due to tidal trapping from literature.

2.1. Tidal trapping mechanism

Tidal trapping is the mechanism where shoals, side channels, harbours and other basins give rise to longitudinal dispersion of salt in the main channel (Garcia et al., 2022; Schijf and Schönfeld, 1953). This mechanism originates from a phase difference in tidal velocities between a main and a side channel.

The impact of friction becomes important for determining the phase difference. Regions with relatively high resistance lose a significant amount of momentum. These regions are typically shallower or have more vegetation, such as a side channel. Due to the loss of momentum, the flows in these regions can respond quickly to changes in the barotropic pressure gradient (MacVean and Stacey, 2011).

The main channel is deeper and therefore less influenced by friction. So, as the tide changes from flood to ebb, the barotropic pressure gradient first needs to overcome the flow's inertia before the flow changes its direction. Thus as the tide reverses on ebb, the side channel begins to flow back into the main channel, while the main channel continues to flood (MacVean and Stacey, 2011).

Tidal trapping can be shown in a conceptual schematic, as is done in figure 2.1. This schematic shows the impact of the phase difference between a side channel and the main channel. It causes a salinity anomaly due to fresher water in the main channel and prevents the saltiest water from travelling into the creek (Garcia et al., 2022).

During ebb, the fresher creek outflow reduces the amount of salt transported to the sea in the downstream area of the creek, compared to the salt transported upstream by the flood tide. This results in a net landward transport of salt over a tidal cycle. However, this inland transport is balanced by the river's flow to the sea (Garcia et al., 2022).

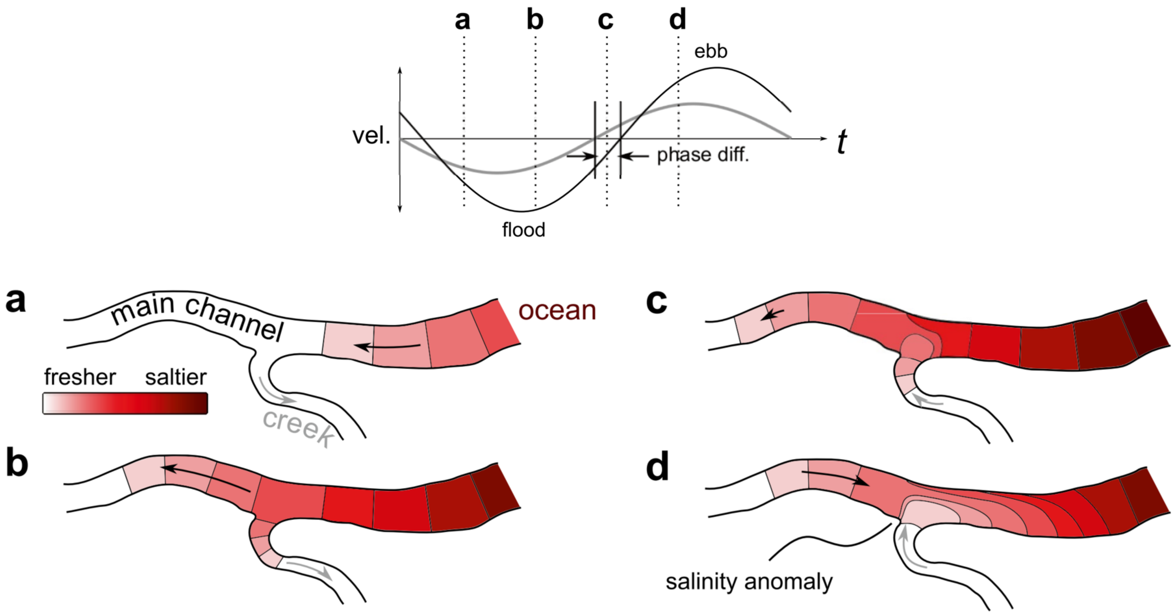

Figure 2.1: Conceptual schematic of tidal trapping. The time series shows the relative velocity magnitude of the main channel (black) and the creek (grey) and the phase difference between the two. **(a)** Salt is carried into the main channel during flood tide. **(b)** The saltwater fills the creek from the main channel, causing an axial salinity gradient. **(c)** The tide reverses and causes the creek to flow back into the main channel while the inertia prevents the main channel from reversing, preventing the saltiest water from going into the creek. **(d)** The flow in the main channel reverses, and the fresher water from the creek causes a negative salinity anomaly in the main channel. Figure retrieved from Garcia et al. (2022)

2.2. Dispersion coefficient for tidal trapping

In this section, two analytical dispersion coefficients for tidal trapping are discussed. One derived by Okubo (1973) and one derived by MacVean and Stacey (2011).

2.2.1. Dispersion coefficient according to Okubo (1973)

Okubo (1973) developed a theoretical model for the entrapment phenomenon. However, the knowledge about the hydrodynamical features associated with this phenomenon was limited. Thus, the exchange process between the main channel and the traps had to be simplified by parameterizing it.

To minimize mathematical efforts, Okubo (1973) restricted the analysis to one-dimensional diffusion. Furthermore, he represented the exchange between the traps and the main channel as source and sink terms. The depth for both the main channel and the trap is uniform. This resulted in the following analytical expression for trapping dispersion in the main channel (Okubo, 1973).

$$K_{trap,D} = \frac{r\hat{U}_m^2}{\omega}\left(\frac{\frac{\omega}{k_{trap}}}{2(1+r)^2\cdot(1+r+\frac{\omega}{k_{trap}})}\right) \tag{2.1}$$

Where $K_{trap,D}$ is the dispersion coefficient due to tidal trapping, r is the ratio of the trap volume to the main channel volume, ${k_{trap}}^{-1}$ is the characteristic residence time of a substance in the trap, $\hat{U}_m$ is the tidal velocity amplitude in the main channel and $\omega = \frac{2\pi}{T}$ is the tidal radian frequency with T equal to the tidal period.

The work of Okubo (1973) shows the dependency of trapping on the geometry and the exchange timescale of the trap. Furthermore, Okubo (1973) found a typical value of k_{trap} in the order of 10^{-4} s^{-1} and applied it to the Mersey River estuary. Where he found a reasonable agreement for equation 2.1. However, Okubo (1973) also states that precise knowledge of the exchange mechanism would replace k_{trap} with more appropriate parameters.

2.2.2. Dispersion coefficient according to MacVean and Stacey (2011)

MacVean and Stacey (2011) noted that the formulation of Okubo (1973) has its limits in certain use cases. Problems arise in the case of advective exchange between the main channel and the traps, as the formulation is based on diffusive exchange. An example of advective exchange is a trap which fills and drains with the tide.

The problems arising are twofold. First, the formulation of Okubo (1973) does not consider the strength of the tidal advection, which drives the exchange. Secondly, the phase difference between the response of the trap and that of the channel to the tidal pressure gradient is not included.

MacVean and Stacey (2011) used a similar analysis as Okubo (1973). For a set of idealized cases with different scenarios of horizontal mixing, they calculated the effective dispersion rate. In the end, they came to the following formulation of the tidal trapping dispersion for a well-mixed branching channel system.

$$K_{trap,A} = \frac{\epsilon \hat{U}_m^2}{\omega}\left[\sin\alpha\cos\alpha\left(\frac{3\cos\alpha + 32\sin\alpha}{12\pi}\right)\right] \tag{2.2}$$

Where ϵ is the salt mass trapped in the side channel compared to the main channel and α is the phase lag between the flow into the trap and the flow in the main channel, expressed in radians.

MacVean and Stacey (2011) compared their formulation of the tidal trapping dispersion to the one made by Okubo (1973). They noted that for a trap filling and draining with the tidal period, the formulation of Okubo (1973) overestimates the dispersion significantly.

The parameters ϵ and r can be related to one another. Garcia et al. (2022) used the following relation based on the tidally averaged cross-sectional salinity (s_0).

$$\epsilon = r\left(\frac{s_{0,\text{side channel}}}{s_0}\right) \quad \text{with} \quad \frac{s_{0,\text{side channel}}}{s_0} \approx 0.9 \tag{2.3}$$

Garcia et al. (2022) calculated an empirical estimate of the tidal trapping dispersion and compared it to the formulations of Okubo (1973) and MacVean and Stacey (2011). They noted that the characteristic residence time (k_{trap}) for a branching channel system should be at a maximum half a tidal period. That corresponds to the largest difference between a particle entering and exiting the trap and a particle remaining in the main channel. Furthermore, at least there should be a velocity phase difference between the side and main channel. Garcia et al. (2022) further concluded that in case the appropriate exchange timescale is selected, the formulations of Okubo (1973) and MacVean and Stacey (2011) are nearly equivalent (Garcia et al., 2022).

2.3. Conclusion

Tidal trapping is driven by a phase difference between the tidal velocities in the main and side channel, where the phase of the side channel is ahead of the main channel. Differences in geometry or friction properties between the main and side channels typically cause this phase difference. The fresher side channel outflow reduces the amount of salt transported back to the sea, resulting in a net inland transport of salt. In addition, the phase difference prevents the saltiest water in the main channel, arriving near the end of the flood, from entering the side channel and reduces salt intrusion in this branch. The impact of tidal trapping on the main channel has been described by Okubo (1973) and MacVean and Stacey (2011) with a dispersion coefficient. Both formulations give nearly equivalent results, given a correctly selected exchange timescale. The advantage of MacVean and Stacey (2011) is the direct use of the phase difference between flow in the main and side channels.

3 Derivation harmonic wave propagation

The previous chapter showed that tidal trapping is driven by a phase difference between tidal velocities, typically caused by differences in the geometry of the main and side channels. Accurately modelling the process of tidal trapping requires a method to determine the propagation of the tide into a system of channels with different geometries. This can be achieved by modelling the tide as a harmonic wave, propagating in a network of prismatic channels. In addition, as the goal is to gain insight into the impact of the geometry on the phase difference, we choose to use an analytical model. As an analytical model can give additional information about the underlying processes.

This chapter describes the derivation of the formulas needed to represent the tide in a multi-branch system. The method originates from Lorentz (1926) and here the derivation by Battjes and Labeur (2017) is followed. Section 3.1 describes the derivation of the two most important equations of the analytical model, which are the mass balance and momentum balance. In section 3.2, the solution for harmonic wave propagation is derived and written in a complex matrix notation. Section 3.3 treats how this method can be implemented in a network. At last, a few non-linear effects are discussed in section 3.4.

3.1. Equations of motion

This section describes the derivation of the basic equations, which will be used for discharge and water level calculations inside channels. First, the mass balance is derived, followed by the momentum balance.

3.1.1. Mass balance

Consider a control volume of water with a length Δx and a cross-section containing the entire wet area, see figure 3.1. Due to the free surface of a natural water system, the pressure variation is limited, meaning there is not enough pressure to create density variations. So, the water inside this control volume can be considered incompressible. This reduces the mass balance to a volume balance and is called the continuity equation.

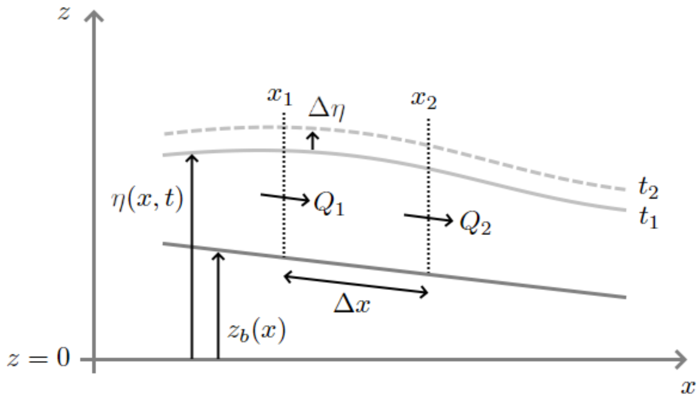

Figure 3.1: Longitudinal transect of an open channel

A volume of water passing a cross-section in a certain time is defined as the discharge (Q) or the volume flux. The net increase in the volume of the control volume in a short time interval Δt is as follows:

$$(Q_1 - Q_2)\Delta t = -\Delta Q \Delta t \tag{3.1}$$

Suppose that the inflow Q_1 is larger than the outflow Q_2. The difference between the two is stored in the control volume. This results in a control volume increase by ΔV, which can be expressed in a change in cross-sectional area and length: $\Delta V = \Delta A \cdot \Delta x$. Equating the storage to the net inflow and taking the limit for $\Delta t \to 0$ and $\Delta x \to 0$ results in:

$$\frac{\partial A}{\partial t} + \frac{\partial Q}{\partial x} = 0 \tag{3.2}$$

The storage results in a rise of the free surface by $\Delta\eta$. So, the change in the cross-sectional area can be rewritten in terms of the increase in the free surface and the width of the free surface, resulting in $\Delta A = \Delta\eta \cdot B$. Thus, equation 3.2 can be written as follows:

$$B\frac{\partial \eta}{\partial t} + \frac{\partial Q}{\partial x} = 0 \tag{3.3}$$

3.1.2. Momentum balance

The momentum balance is derived from the Euler equations, which are for an ideal (inviscid) fluid of constant density. Next, vertical accelerations are neglected, as the piezometric head is considered uniform over the vertical for long waves. Furthermore, the forcing is considered uniform in the cross-section, as lateral variations in the free surface can be neglected due to the small net effect on the large-scale streamwise motion. In the end, only the streamwise component x remains. To turn this into a one-dimensional model, the values must be averaged over the cross-section. As the forcing is uniform and resistance is neglected for now, the Euler equation in a streamwise direction can also be applied to cross-sectionally averaged flow velocities U.

$$\frac{DU}{Dt} = \frac{\partial U}{\partial t} + U\frac{\partial U}{\partial x} = -g\frac{\partial \eta}{\partial x} \tag{3.4}$$

For the Euler equation, the resistance was neglected, but wall shear stress is important. The resistance force per unit length F_r depends on the averaged shear stress $\overline{\tau}$ along the wet perimeter and the wet perimeter P_w itself. The shear stress can be rewritten as a function of the velocity U, the density ρ and the friction coefficient c_f.

$$F_r = \overline{\tau} P_w = \rho c_f |U| U P_w \tag{3.5}$$

This can be rewritten as a resistance per unit mass by dividing by ρA_c, with A_c being the conveyance cross-section, which is part of the cross-section that is responsible for transport.

$$\frac{F_r}{\rho A_c} = \frac{\rho c_f |U| U P_w}{\rho A_c} = c_f \frac{|U|U}{R} \tag{3.6}$$

Where R is the hydraulic radius of the channel. The resistance per unit mass can be subtracted from the left-hand side of equation 3.4.

$$\begin{aligned} \frac{DU}{Dt} = \frac{\partial U}{\partial t} + U\frac{\partial U}{\partial x} &= -g\frac{\partial \eta}{\partial x} - c_f \frac{|U|U}{R} \\ \Rightarrow \frac{\partial U}{\partial t} + U\frac{\partial U}{\partial x} &+ g\frac{\partial \eta}{\partial x} + c_f \frac{|U|U}{R} = 0 \end{aligned} \tag{3.7}$$

Multiplying equation 3.7 by A_c and equation 3.2 by U and adding these two together results in the momentum balance.

$$\left.\begin{aligned} A_c\frac{\partial U}{\partial t} + Q\frac{\partial U}{\partial x} + gA_c\frac{\partial \eta}{\partial x} + c_f\frac{A_c|U|U}{R} &= 0 \\ U\frac{\partial A}{\partial t} + U\frac{\partial Q}{\partial x} &= 0 \end{aligned}\right\} \frac{\partial Q}{\partial t} + \frac{\partial}{\partial x}\left(\frac{Q^2}{A_c}\right) + gA_c\frac{\partial \eta}{\partial x} + c_f\frac{|Q|Q}{A_c R} = 0 \tag{3.8}$$

3.1.3. Summary

The continuity equation and the momentum balance together are also called the one-dimensional shallow-water equations. They form the basis for computations of one-dimensional long-wave phenomena.

$$\underbrace{B\frac{\partial \eta}{\partial t}}_{\text{mass storage}} + \underbrace{\frac{\partial Q}{\partial x}}_{\text{discharge gradient}} = 0 \tag{3.9}$$

$$\underbrace{\frac{\partial Q}{\partial t}}_{\text{local acceleration}} + \underbrace{\frac{\partial}{\partial x}\left(\frac{Q^2}{A_c}\right)}_{\text{advective acceleration}} + \underbrace{gA_c\frac{\partial \eta}{\partial x}}_{\text{pressure gradient}} + \underbrace{c_f\frac{|Q|Q}{A_c R}}_{\text{resistance}} = 0 \tag{3.10}$$

3.2. Analytical solution for harmonic wave propagation

This section aims to derive an analytical solution for a harmonic wave based on the continuity equation and the momentum balance. First, the continuity equation and the momentum balance are combined to create the wave equation. Next, a general solution for the water level is derived. Followed by the general solution for the discharge. Then, the water level and the discharge at the channel's beginning are related to those at the other end. The resulting equations can be combined and joined with two boundary conditions to solve the unknown water level and discharge at the ends of the channel. Next, this is extended to multiple channels in a network. Finally, non-linear effects are discussed to better understand the limitations of this analytical solution.

3.2.1. The wave equation

The tide entering an estuary can be modelled analytically based on the previously explained mass and momentum balance. For low periodic long waves, like a tide, it is valid to use linear approximations. Thus, the advection of momentum can be neglected and the quadratic resistance term can be linearized.

Lorentz (1926) derived a linearization of the resistance. His formulation made it only dependent on Q and a friction coefficient κ, which has the dimension of s^{-1}. The linearization focused on the energy loss during a tidal cycle. The resulting energy loss should be the same as in the nonlinearized variant. This, however, introduced an accepted error in the time variation. The result of Lorentz was as follows:

$$c_f \frac{|Q|Q}{A_c R} \approx \kappa Q \quad \text{with} \quad \kappa = \frac{8}{3\pi} c_f \frac{\hat{Q}}{A_c R} \tag{3.11}$$

Where $\hat{Q}$ is the discharge amplitude. This value is often unknown beforehand but can be derived from the results. So, to find the final value of $\hat{Q}$ iterations are required. According to Lorentz (1926), a large change in the amplitude only results in a small change in the final result.

Combining the results of the equations 3.10 and 3.11, gives the following result:

$$\frac{\partial Q}{\partial t} + gA_c \frac{\partial \eta}{\partial x} + \kappa Q = 0 \tag{3.12}$$

The discharge Q can be eliminated from the equation by differentiating equation 3.9 with respect to t and equation 3.12 with respect to x and subtracting the momentum balance from the continuity equation. According to the assumption of long low waves, the variation of the free surface will be neglected for the parameters A_c and B, thus they do not vary with time. Furthermore, using prismatic channels means that the cross-section A_c does not change in the streamwise direction.

$$\frac{\partial B}{\partial t} = 0 \quad \text{and} \quad \frac{\partial A_c}{\partial t} = 0 \quad \text{and} \quad \frac{\partial A_c}{\partial x} = 0 \tag{3.13}$$

$$\left.\begin{array}{r} \frac{\partial}{\partial t}\left(B\frac{\partial \eta}{\partial t} + \frac{\partial Q}{\partial x}\right) = 0 \Rightarrow B\frac{\partial^2 \eta}{\partial t^2} + \frac{\partial^2 Q}{\partial x \partial t} = 0 \\ \frac{\partial}{\partial x}\left(\frac{\partial Q}{\partial t} + gA_c\frac{\partial \eta}{\partial x} + \kappa Q\right) = 0 \Rightarrow \frac{\partial^2 Q}{\partial t \partial x} + gA_c\frac{\partial^2 \eta}{\partial x^2} + \kappa\frac{\partial Q}{\partial x} = 0 \end{array}\right\} B\frac{\partial^2 \eta}{\partial t^2} - gA_c\frac{\partial^2 \eta}{\partial x^2} - \kappa\frac{\partial Q}{\partial x} = 0 \tag{3.14}$$

Next, the resistance term can be rewritten in terms of $\frac{\partial \eta}{\partial t}$, by again using the mass balance (equation 3.9). Furthermore, by dividing all terms with B, the parameters in front of the second term can be expressed in terms of the long-wave speed.

$$\frac{\partial Q}{\partial x} = -B\frac{\partial \eta}{\partial t} \quad \text{and} \quad c_0 = \sqrt{\frac{gA_c}{B}} \tag{3.15}$$

This results in the one-dimensional wave equation as stated in equation 3.16. This is known as the wave equation and is an important equation for describing waves.

$$\frac{\partial^2 \eta}{\partial t^2} - {c_0}^2\frac{\partial^2 \eta}{\partial x^2} + \kappa\frac{\partial \eta}{\partial t} = 0 \tag{3.16}$$

3.2.2. The general solution for the water level

The solution to the wave equation is in the form:

$$\eta(x,t) = \mathbb{R}\left(\tilde{\eta}(x)e^{i\omega t}\right) \tag{3.17}$$

Where ω is the tidal radian frequency and $\tilde{\eta}$ is the complex amplitude of the water level. Next, this is substituted into equation 3.16 and divided by the time factor $e^{i\omega t}$.

$$\frac{d^2\tilde{\eta}}{dx^2} + \frac{\omega^2 - i\omega\kappa}{{c_0}^2}\tilde{\eta} = 0 \tag{3.18}$$

The ratio of resistance to inertia or the relative resistance is dimensionless and defined as follows:

$$\sigma \equiv \frac{\kappa}{\omega} = \frac{8}{3\pi} c_f \frac{\hat{Q}}{\omega A_c R} \tag{3.19}$$

Substituting $\kappa = \sigma\omega$ and $k_0 = \dfrac{\omega}{c_0}$, which is the wave number in the absence of resistance, results in the following equation.

$$\frac{d\tilde{\eta}^2}{dx^2} + k_0^2 \left(1 - i\sigma\right) \tilde{\eta} = 0 \tag{3.20}$$

This is an ordinary differential equation and has a solution in the form of an exponential function and is substituted into equation 3.20.

$$\tilde{\eta}(x) = e^{P \cdot x} \quad \Rightarrow \quad P^2 + k_0^2 \left(1 - i\sigma\right) = 0 \tag{3.21}$$

This equation has two opposite, complex roots P_1 and $P_2 = -P_1$, denoted as p and $-p$ and this results in the general solution for $\tilde{\eta}(x)$.

$$\tilde{\eta}(x) = C^+ e^{-px} + C^- e^{px} = \tilde{\eta}^+(x) + \tilde{\eta}^-(x) \quad \text{with} \quad p = ik_0\sqrt{1 - i\sigma} \tag{3.22}$$

It represents two waves travelling in opposite directions when the time factor $e^{i\omega t}$ is included. The two complex integration constants are C^- and C^+. Both contain information about the amplitude and the phase of the wave. The values of the integration constants are determined by the boundary conditions.

3.2.3. The general solution for the discharge

The discharge also has an expected solution in the form of equation 3.17, but then depending on the discharge. Together with the general solution of $\tilde{\eta}(x)$, this can be substituted into the continuity equation (equation 3.9). In the end, this results in a general solution for the complex discharge $\tilde{Q}$.

$$\tilde{Q}(x) = \frac{i\omega B}{p} \left(C^+ e^{-px} - C^- e^{px}\right) \tag{3.23}$$

3.2.4. Complex amplitudes at the end of a prismatic channel

The relationships between the surface elevation and the discharge on one end of the channel will be expressed in terms of those at the other end. The starting point is equation 3.22 and 3.23. The factor $\frac{i\omega B}{p}$ is temporarily removed from the general solution of the discharge by introducing a new complex variable $\tilde{Z}$, with the dimension of a length.

$$\tilde{Z}(x) \equiv \frac{p}{i\omega B} \tilde{Q}(x) = C^+ e^{-px} - C^- e^{px} \tag{3.24}$$

For $x = 0$, the general solutions simplify to:

$$\tilde{\eta}(0) = \tilde{\eta}_0 = C^+ + C^- \quad \text{and} \quad \tilde{Z}(0) = \tilde{Z}_0 = C^+ - C^- \tag{3.25}$$

This makes it possible to express the integration constants in terms of $\tilde{\eta}_0$ and $\tilde{Z}_0$.

$$C^+ = \frac{\tilde{\eta}_0 + \tilde{Z}_0}{2} \quad \text{and} \quad C^- = \frac{\tilde{\eta}_0 - \tilde{Z}_0}{2} \tag{3.26}$$

Knowing the integration constants, it is possible to express the values of $\tilde{\eta}(x)$ and $\tilde{Z}(x)$ at $x = l$. However, as no specific boundary conditions are imposed here, this relation applies to any pair of cross-sections of a prismatic channel. Thus, l could also be replaced by x, indicating an arbitrary location.

$$\tilde{\eta}(l) = \tilde{\eta}_l = C^+ \cdot e^{-pl} + C^- \cdot e^{pl} = \frac{\tilde{\eta}_0 + \tilde{Z}_0}{2} \cdot e^{-pl} + \frac{\tilde{\eta}_0 - \tilde{Z}_0}{2} \cdot e^{pl} \tag{3.27}$$

$$\tilde{Z}(l) = \tilde{Z}_l = C^+ \cdot e^{-pl} - C^- \cdot e^{pl} = \frac{\tilde{\eta}_0 + \tilde{Z}_0}{2} \cdot e^{-pl} - \frac{\tilde{\eta}_0 - \tilde{Z}_0}{2} \cdot e^{pl} \tag{3.28}$$

Next, it can be rewritten in terms of hyperbolic functions and the resulting equations are also known as the four-pole equations.

$$\tilde{\eta}_l = \tilde{\eta}_0 \cdot \cosh pl - \tilde{Z}_0 \cdot \sinh pl \tag{3.29}$$

$$\tilde{Z}_l = -\tilde{\eta}_0 \cdot \sinh pl + \tilde{Z}_0 \cdot \cosh pl \tag{3.30}$$

These two equations have four unknowns, two water levels ($\tilde{\eta}_0, \tilde{\eta}_l$) and two variables related to the discharge ($\tilde{Z}_0, \tilde{Z}_l$). The variable p is known, given an initial estimate of $\hat{Q}$. These equations can be solved in combination with two boundary conditions.

3.2.5. Solution in matrix form

As stated in the previous section, two boundary conditions are needed to solve the four-pole equations. The first is at the sea side of the channel and is the forcing of the water level due to the tide. The second boundary condition is often based on the discharge at the end of the channel, at $x = l$. A special case is a semi-closed basin with no discharge at the end. However, here the most general situation is solved, so $\tilde{Z}_l \neq 0$.

The four-pole equations can be rewritten in terms of the unknown variables $\tilde{\eta}_l$ and $\tilde{Z}_0$. First, the formulation of $\tilde{\eta}_0$ is rewritten, and it will express $\tilde{\eta}_0$ as a function of the two unknowns.

$$\tilde{\eta}_l = \tilde{\eta}_0 \cdot \cosh pl - \tilde{Z}_0 \cdot \sinh pl \quad \Rightarrow \quad \tilde{\eta}_0 = \frac{\tilde{\eta}_l + \tilde{Z}_0 \cdot \sinh pl}{\cosh pl} = \tilde{\eta}_l \cdot \frac{1}{\cosh pl} + \tilde{Z}_0 \cdot \tanh pl \tag{3.31}$$

Next, the formulation of $\tilde{\eta}_0$ can be used in equation 3.30 to express $\tilde{Z}_l$ in terms of the unknowns.

$$\begin{aligned}
\tilde{Z}_l &= -\tilde{\eta}_0 \cdot \sinh pl + \tilde{Z}_0 \cdot \cosh pl = -\left(\tilde{\eta}_l \cdot \frac{1}{\cosh pl} + \tilde{Z}_0 \cdot \tanh pl\right) \cdot \sinh pl + \tilde{Z}_0 \cdot \cosh pl \\
&= -\tilde{\eta}_l \cdot \frac{\sinh pl}{\cosh pl} - \tilde{Z}_0 \cdot \frac{\sinh^2 pl}{\cosh pl} + \tilde{Z}_0 \cdot \frac{\cosh^2 pl}{\cosh pl} = \frac{-\tilde{\eta}_l \cdot \sinh pl + \tilde{Z}_0 \left(\cosh^2 pl - \sinh^2 pl\right)}{\cosh pl} \\
&= -\tilde{\eta}_l \cdot \tanh pl + \tilde{Z}_0 \cdot \frac{1}{\cosh pl}
\end{aligned} \tag{3.32}$$

Combining equation 3.31 and 3.32 and rewriting it in matrix form, gives a formulation in the form of $\boldsymbol{A}\vec{x} = \vec{b}$. These linear equations can be solved as all the unknowns are stated in the vector $\vec{x}$.

$$\begin{bmatrix} \frac{1}{\cosh pl} & \tanh pl \\ -\tanh pl & \frac{1}{\cosh pl} \end{bmatrix} \begin{bmatrix} \tilde{\eta}_l \\ \tilde{Z}_0 \end{bmatrix} = \begin{bmatrix} \tilde{\eta}_0 \\ \tilde{Z}_l \end{bmatrix} \tag{3.33}$$

The results of $\tilde{\eta}_l$ and $\tilde{Z}_0$ are most likely complex numbers containing information about the amplitude and the phase. This requires the results to be translated into real values. For the discharge, it is necessary to first convert $\tilde{Z}_0$ back to $\tilde{Q}_0$ by using the reverse of equation 3.24.

$$\begin{bmatrix} \dfrac{1}{\cosh pl} & \dfrac{p}{i\omega B} \cdot \tanh pl \\ -\dfrac{i\omega B}{p} \cdot \tanh pl & \dfrac{1}{\cosh pl} \end{bmatrix} \begin{bmatrix} \tilde{\eta}_l \\ \tilde{Q}_0 \end{bmatrix} = \begin{bmatrix} \tilde{\eta}_0 \\ \tilde{Q}_l \end{bmatrix} \tag{3.34}$$

Next, the modulus of $\tilde{\eta}_l$ and $\tilde{Q}_0$ are used to get the amplitude of the water level and discharge, respectively. Along with the argument, to determine the phase of both variables.

The boundary condition $\tilde{\eta}_0$ is given by the tide and in the form $A \cdot \cos(\frac{2\pi}{T})$, where A and T are the amplitude and period of the tide, respectively. $\tilde{Q}_l$ is the (complex) amplitude of the discharge. It is important to note that this is the amplitude of a periodic discharge, as the time dependency $e^{i\omega t}$ is not yet included. Furthermore, p can be calculated as it is based on system values.

3.3. Network of channels

The above formulas have been derived for a singular channel. It is also possible to connect multiple channels in series. For example, a long channel can be split into several adjacent sections to deal with changing geometry in a simplified manner. It is also possible for the channels to form a network structure so larger areas can be studied. To solve such a network, each channel junction, also called a note, requires the correct transition conditions.

The unknowns in the system are the complex amplitudes of the surface elevation and the discharge at the nodes. So for each section, there are four unknowns, two on both ends, as was the case in a single channel. Looking at a node in a network, this means that a node has two unknowns per connected section, so $2N$ unknowns for N sections. Each section or channel has two equations for the propagation in the channel as derived in the above sections. Thus, each node has one equation per connected section, meaning N equations per node.

Type	Unknowns	Equations	Boundary conditions	Transition conditions
Single section channel	4	2	2	0
Double section channel	8	4	2	2
Junction	12	6	3	3

Table 3.1: Required boundary and transition conditions for different network types

All internal nodes have two extra equations. First, the sum of the discharges towards the node is zero, assuming there is no storage at the node. Secondly, the water levels at the node should be equal for all N sections connected to the node. Furthermore, external nodes require boundary conditions as is the case for a single channel. In the end, this means there are as many independent equations as there are unknowns, meaning that the problem is well-posed and the solution is unique.

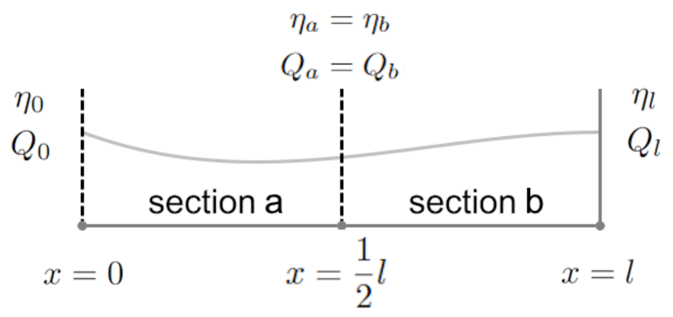

Figure 3.2: Two channel sections with three nodes and accompanying boundary and transition conditions

3.4. Non-linear effects

All non-linear effects are neglected in the above-mentioned method. This means all higher harmonics of the tide are ignored. These non-linear effects increase as the ratio of wave height to water depth increases. So, higher harmonics of for example the M2-tide, like the M4 and M6 are also called shallow-water tides. The shallow-water tides can become more important as the tide travels further landwards into the estuary.

The same problem arises with the inclusion of a constant river discharge. The combination of freshwater discharge and tidal forcing causes an increase in the linear and non-linear effects of the friction (Jay, 1991).

Part of this limitation can be overcome by changing the friction linearization in the model. The linearization of Lorentz is designed for a single harmonic wave with no additional river discharge. Mazure (1937) showed that the result of Lorentz could also be obtained by a harmonic analysis. This analysis is also applicable in case there is an additional freshwater discharge (Mazure, 1937). The discharge is split into two parts: Q_f and Q_t, a constant discharge and a tidally varying discharge, respectively. Mazure found the following constants for κ_f and κ_t (Dronkers et al., 1959):

$$\kappa_f = \begin{cases} \frac{c_f}{A_c R}\left(1.27\hat{Q}_t + 0.23\frac{Q_f^2}{\hat{Q}_t}\right) & \text{if} \quad Q_f \leq \hat{Q}_t \\ \frac{c_f}{A_c R}\left(Q_f + 0.5\frac{\hat{Q}_t^2}{Q_f}\right) & \text{if} \quad Q_f > \hat{Q}_t \end{cases} \tag{3.35}$$

$$\kappa_t = \begin{cases} \frac{c_f}{A_c R}\left(\frac{8}{3\pi}\hat{Q}_t + 1.15\frac{Q_f^2}{\hat{Q}_t}\right) & \text{if} \quad Q_f \leq \hat{Q}_t \\ \frac{c_f}{A_c R}\left(2 \cdot Q_f\right) & \text{if} \quad Q_f > \hat{Q}_t \end{cases} \tag{3.36}$$

Where $\hat{Q}_t$ is the tidal amplitude and Q_f is the freshwater discharge. A comparison between the friction formulation of Lorentz and Mazure is given in figure 3.3. It shows equal results in case of no freshwater discharge, and significantly improved results for additional freshwater discharge.

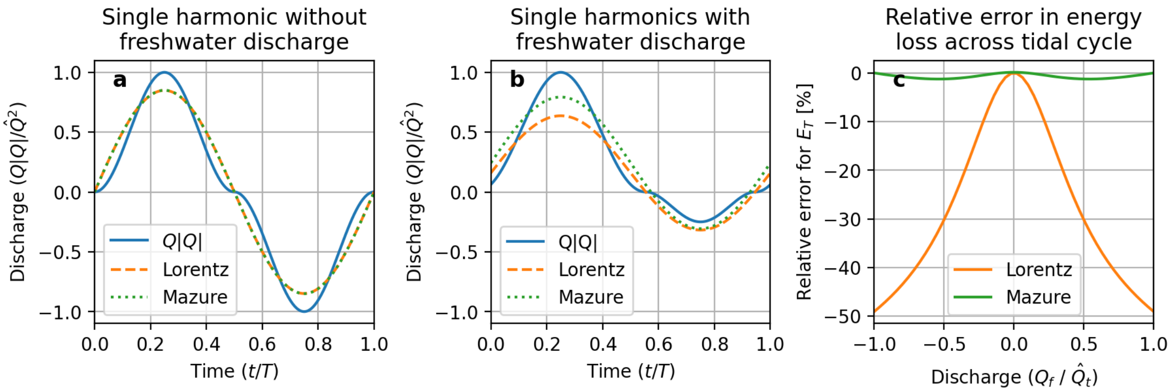

Figure 3.3: Comparison linearization quadratic velocity. **(a)** Linearization of single harmonic **(b)** Linearization of single harmonic with constant freshwater discharge $Q_f = \frac{1}{3}\hat{Q}_t$ **(c)** Comparison relative error in energy loss across a tidal cycle

3.5. Conclusion

In this chapter, the propagation of the tide is described with the wave equation, derived from the mass and momentum balance. The tide is considered to be a low, periodic, long wave, which makes it valid to use linear approximations. This neglects the advection term and linearizes the quadratic friction. In addition, a prismatic geometry is used, which means there is only a conveyance cross-section. For use in a multi-branch system, a combination of transition and boundary conditions is required to derive a unique solution. Adding boundary conditions such as a constant river discharge in combination with the tide, requires a different linearization of the friction. The linearization of Lorentz (1926) is derived for a single constituent of the tide, while the linearization of Mazure (1937) includes the interaction between tide and river discharge.

Part II

A single junction network in an analytical model

4 Development analytical model for tidal propagation

The previous chapters 2 and 3, showed the importance of the phase difference for tidal trapping and the derivation of the hydrodynamic formulations needed to model the tide in a multi-branch system. In this chapter, the previous derivation is used to develop an analytical model with which the impact of the geometry on the phase difference can be investigated. This chapter first describes the steps to develop the model and what variables are investigated in section 4.1. This is followed by the development of the model in section 4.2.

4.1. Methodology analytical model

To investigate how the geometry of the side channel influences the flow characteristics and the velocity phase difference between the main and side channels, a one-dimensional analytical model is developed. The analytical model is based on the formulations by Lorentz (1926). He used this model to determine the impact of the Zuiderzee closure. The formulations are derived from the continuity equation and the momentum balance and can be solved for each channel section in combination with 2 boundary or transition conditions.

The analytical model is a simplification of reality, with the following properties:

Strengths

- Low computational cost
- Uses prismatic geometry (L, B, d) of side channel
- Uses prismatic geometry (L, B, d) of main channel
- Linearized friction
- Multiple types of boundary conditions
  - Constant river discharge
  - Basic tidal forcing
- Complex networks possible with junctions and loops

Limitations

- Higher order harmonics of the tide cannot be included in a single calculation
- Energy losses at cross-section transitions are neglected
- Salinity is not included, thus no density-driven flows
- Complex three-dimensional flows are not modelled
- Complex geometry in the side and main channel is not possible
- The friction is linearized

First, an analytical model is made for a prismatic semi-closed channel, as can be seen in figure 4.1a. The boundary conditions are given by a zero discharge at the closed end and a tidally forced water level at the open end.

The model is extended to include multiple channel sections in series. The original semi-closed channel is split into 2 sections, see figure 4.1b. By keeping all remaining variables equal, the result should be identical to the original semi-closed channel and the implementation of the transition conditions can be verified.

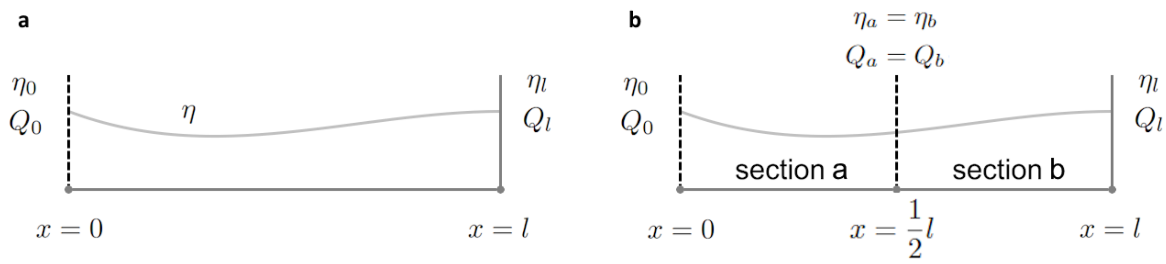

Figure 4.1: Schematization of the analytical models

Next, the model is extended to include junctions. A second semi-closed channel section is added to the split semi-closed channel, forming a second branch. This forms a single junction network (SJN).

The last extension to the analytical model is to include multiple channel sections forming a loop. This addition makes it possible to model the Rhine Meuse Delta in a simplified manner.

Multiple simulations will be run for the SJN model, to derive a generic insight into the impact of the geometry. For each model run a different parameter is varied. This includes the geometry of the side and main channel and different boundary conditions. An overview of all varied parameters and their tested range is given in the table below.

Variable	Symbol	Unit	Condition or configuration
Length side channel	L	km	$1 \leq L \leq 100$
Depth side channel	d_s	m	$2 \leq d_s \leq 10$
Depth main channel	d_m	m	$5 \leq d_m \leq 20$
Width side channel	B_s	m	$20 \leq B_s \leq 500$
Width main channel	B_m	m	$100 \leq B_m \leq 1200$
Friction coefficient side channel	$c_{f,s}$	m	$0.001 \leq c_{f,s} \leq 0.01$
Friction coefficient main channel	$c_{f,m}$	m	$0.001 \leq c_{f,m} \leq 0.01$
Discharge side channel	Q_s	m^3/s	$-50 \leq Q_s \leq 50$
Discharge main channel	Q_m	m^3/s	$-900 \leq Q_m \leq 0$
Tidal amplitude	A_{tide}	m	$0 \leq A_{\text{tide}} \leq 1$

Table 4.1: Multiple test conditions and configurations for the analytical model of the SJN

4.2. Development analytical model

This section describes in further detail how the transition conditions are implemented at a junction. Followed by the method on how to realize a constant discharge in combination with a tidal forcing. Then the set-up of the matrices is shown and the model is validated.

4.2.1. Transition conditions junction

The transition conditions differ slightly between a junction of 3 channel sections and two connected channel sections. The transition conditions for a junction are given below and rewritten, so all unknowns are located right from the equal sign.

$$\eta_a = \eta_b = \eta_c \quad \Rightarrow \quad \eta_a - \eta_b = 0 \quad \text{and} \quad \eta_b - \eta_c = 0 \tag{4.1}$$

$$Q_a = Q_b + Q_c \quad \Rightarrow \quad Q_a - Q_b - Q_c = 0 \tag{4.2}$$

For two connected channel sections, the transition conditions are as follows and also rewritten so all unknowns are located right from the equal sign.

$$\eta_a = \eta_b \quad \Rightarrow \quad \eta_a - \eta_b = 0 \tag{4.3}$$

$$Q_a = Q_b \quad \Rightarrow \quad Q_a - Q_b = 0 \tag{4.4}$$

4.2.2. Constant discharge boundary condition

The combination of freshwater discharge and tide cannot be calculated directly in the model. The analytical model calculates the propagation of a harmonic wave into a system of channels. Thus the results and supplied boundary conditions are single harmonic waves as well. To get around this problem the superposition principle can be used. It states that for a linear system, the net response is equal to the sum of the individual waves.

As stated in section 3.2.1, the system can be approximated as linear, thus the superposition principle can be applied. However, the friction formulation requires special attention. The total friction per channel section is calculated with the formulation of Mazure (1937) and depends both on the freshwater discharge and the tidal amplitude. For most scenarios, the tidal discharge amplitude will be larger than the freshwater discharge. So, the friction coefficient κ depends on the freshwater discharge and the tidal amplitude. When the discharge signal is split into two components in the model, the same friction coefficient should be used for both, see equation 4.5.

$$\kappa Q = \kappa \left(Q_f + Q_t\right) = \kappa Q_f + \kappa Q_t \quad \text{with} \quad \kappa = \frac{c_f}{A_c R}\left(\frac{8}{3\pi}\hat{Q}_t + 1.15\frac{Q_f^2}{\hat{Q}_t}\right) \tag{4.5}$$

The implementation of a constant boundary discharge requires approximating it as a single harmonic wave. This can be achieved by increasing the period of the boundary condition, $T \to \infty$. For relatively short durations, like the period of the M2 tide, this method will create a constant discharge at the boundary. Furthermore, the solution of the model has the shape of a cosine (equation 3.17), so no additional phase is required.

4.2.3. Matrices set-up

All Four-pole equations, transition and boundary conditions are rewritten into matrix form. This is done for a split semi-closed channel, see figure 4.1b. A single semi-closed channel requires only the four-pole equations and two boundary conditions to solve the scenario. The addition of a second channel section introduces four additional equations. The first two are the four-pole equations related to the new channel section. The other two, are the transition conditions of the water level and the discharge between the two channel sections. The ends of the first channel section are no longer the overall end of the network and thus the righthand side of the four-pole equation is moved in front of the equal sign as it is no longer a boundary condition. This is indicated by red squares in the matrix.

$$
\begin{array}{c}
\begin{array}{cc} \text{section a} & \qquad\qquad \text{section b} \end{array} \\
\begin{bmatrix}
f & f & 0 & 0 & 0 & 0 \\
-f & f & 0 & 0 & 0 & \boxed{-1} \\
0 & 0 & f & f & \boxed{-1} & 0 \\
0 & 0 & -f & f & 0 & 0 \\
1 & 0 & 0 & 0 & -1 & 0 \\
0 & 0 & 0 & 1 & 0 & -1
\end{bmatrix}
\end{array}
\begin{bmatrix}
\tilde{\eta}_{1a} \\ \tilde{Q}_0 \\ \tilde{\eta}_2 \\ \tilde{Q}_{1b} \\ \tilde{\eta}_{1b} \\ \tilde{Q}_{1a}
\end{bmatrix}
=
\begin{bmatrix}
\tilde{\eta}_0 \\ 0 \\ 0 \\ \tilde{Q}_2 \\ 0 \\ 0
\end{bmatrix}
\begin{array}{l}
\text{Four-pole equation} \\
\text{Four-pole equation} \\
\text{Four-pole equation} \\
\text{Four-pole equation} \\
\text{Water level transition condition} \\
\text{Discharge transition condition}
\end{array}
\tag{4.6}
$$

Matrix for two channels in series. f indicates parts of the rewritten four-pole equations. The dashed lines indicate which part of the matrix is related to a channel section. The red squares indicate the former righthand side of the rewritten four-pole equations.

The changes to the matrix caused by the creation of a junction and a loop can be seen in appendix A. Additionally, the validation of the implementation is also shown in the same append A.

4.3. Conclusion

In this chapter we developed an analytical model to describe tidal propagation in a multi-branch network. The developed analytical model has a low computational cost, includes a prismatic geometry, allows basic tidal and constant river discharge boundary conditions and can be used to represent complex networks with junctions and loops. The model is built up from a network of two channels in series to a single junction network and finally to a network which includes loops. These steps add additional segments to the matrix, which contains the equations, transition and boundary conditions. Each step is tested and validated against a known reference scenario. These tests showed that all additions to the matrix and there implementation in MATLAB are done correctly.

5

Impact of the geometry on the phase difference in a single junction network

Chapter 4 showed the set-up and validation of the analytical model for tidal propagation in a multi-branch system. This chapter systematically investigates the impact of the geometry on the phase difference, according to a single junction network created in the analytical model. This investigation is done to better understand how the phase difference is impacted by a single geometric variable and how the flow characteristics change. First, the configuration of the analytical model is explained in section 5.1. This is followed by a description of the results of the impact of each variable on the phase difference.

5.1. Configuration single junction network

A single junction network is created as a base scenario. The network is inspired by the Rhine Meuse Delta and the location of the Hollandsche IJssel. The side channel is located 37 km inland from the sea boundary. The main channel is continued for another 120 km, which is roughly the distance to Lobith. These and other system parameters can be found in table 5.1.

Variable	Value	Unit	Variable	Value	Unit
l_m	157	km	l_s	20	km
B_m	800	m	B_s	150	m
d_m	8.5	m	d_s	5	m
$A_{c,m}$	6800	m^2	$A_{c,s}$	750	m^2
$c_{f,m}$	0.005	-	$c_{f,s}$	0.005	-
$\tilde{Q}_{l,m}$	0	m^3/s	$\tilde{Q}_{l,s}$	0	m^3/s
$\tilde{\eta}_0$	0.8	m	l_{junc}	37	km

Table 5.1: System parameters of single junction network

The analytical model results are given for each node, with the node number as subscript. At a junction, the discharge has an additional letter in the subscript, as the results can vary with each section connected to the junction. The sections are labelled in order of lowest node numbers to highest node numbers.

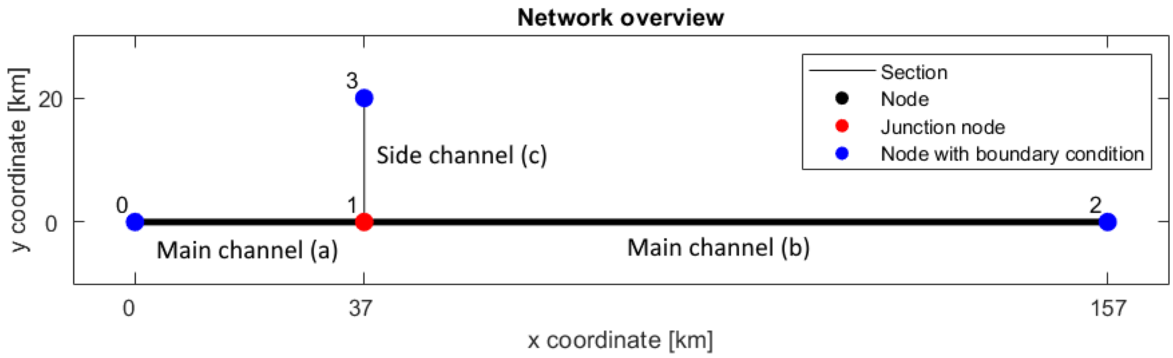

Figure 5.1: Network overview of the single junction analytical model.

The phase difference is defined as the difference in phase between the discharge from the side and the main channel. The main channel section between nodes 0 and 1 is chosen, as this is where the wave originates from, so $\theta = \phi_{Q_{1c}} - \phi_{Q_{1a}}$. The phase difference of the side channel is the difference in phase between the water level and the discharge of the side channel, thus $\theta_s = \phi_{\eta_1} - \phi_{Q_{1c}}$. The phase difference of the two main channel sections is the difference in phase between the water level and the discharge of the main channel. Thus for section a: $\theta_{m,a} = \phi_{\eta_1} - \phi_{Q_{1a}}$ and for section b: $\theta_{m,b} = \phi_{\eta_1} - \phi_{Q_{1b}}$.

The base scenario is used to determine the discharge at the nodes in the network. These results are further split up into the amplitude and the phase. As can be seen in figures 5.2 and 5.3, the amplitude of the discharge decreases in the main channel the further it travels into the network. Furthermore, a small jump can be seen at the junction as the discharge is split between both channels.

The phase of the discharge increases in the main channel as it travels further into the network. It also shows a small jump at the junction. The phase difference between the main and side channels is visible by the large jump from the main channel phase to the side channel phase. At the boundaries, the phase makes a significant jump due to the supplied boundary conditions. The complex discharge amplitude is forced to be 0, so this affects the phase as well. In the side channel, the phase of the discharge hardly changes along the length of the channel.

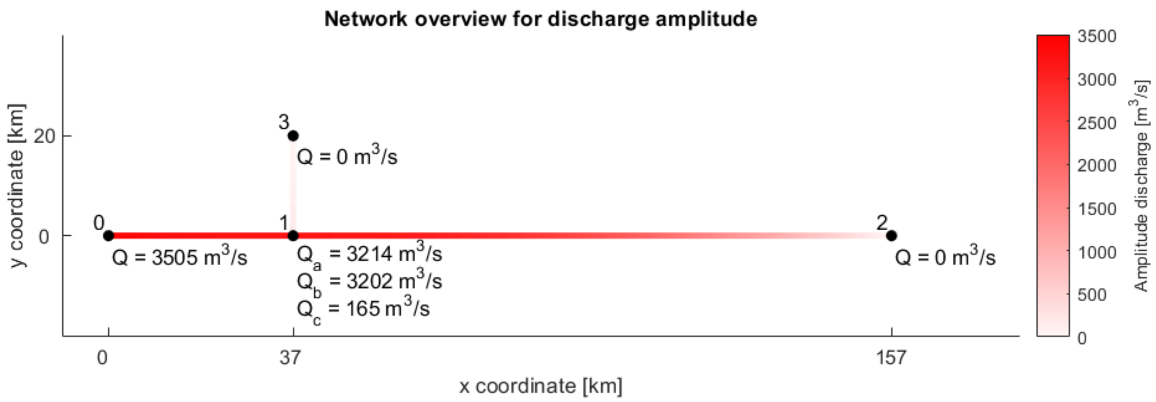

Figure 5.2: Discharge amplitudes across the base network

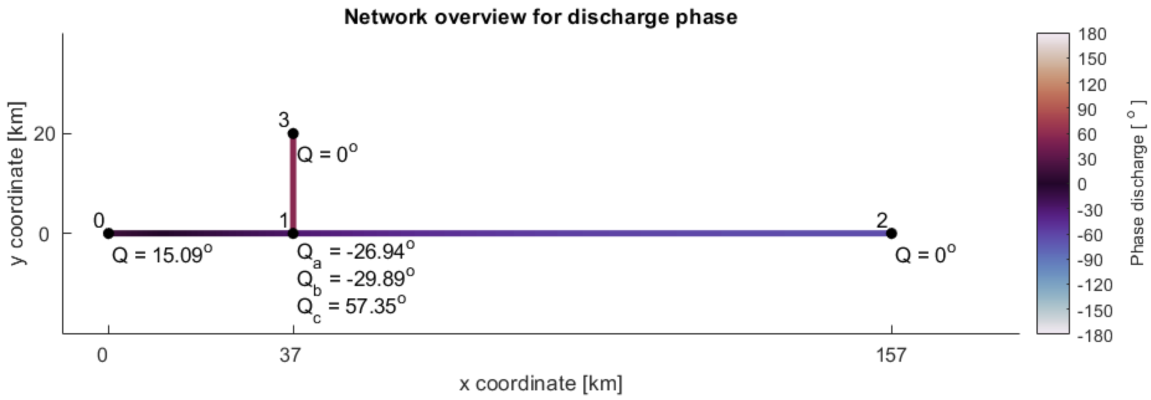

Figure 5.3: Discharge phase across the base network

The phases of the water level and discharge in the main channel after the junction decrease significantly. However, the phase of the water level decreases faster, which causes the phase difference between these two to increase towards -90°. Thus, the wave pattern in the main channel transforms from a propagating wave at the junction towards a standing wave at the closed end.

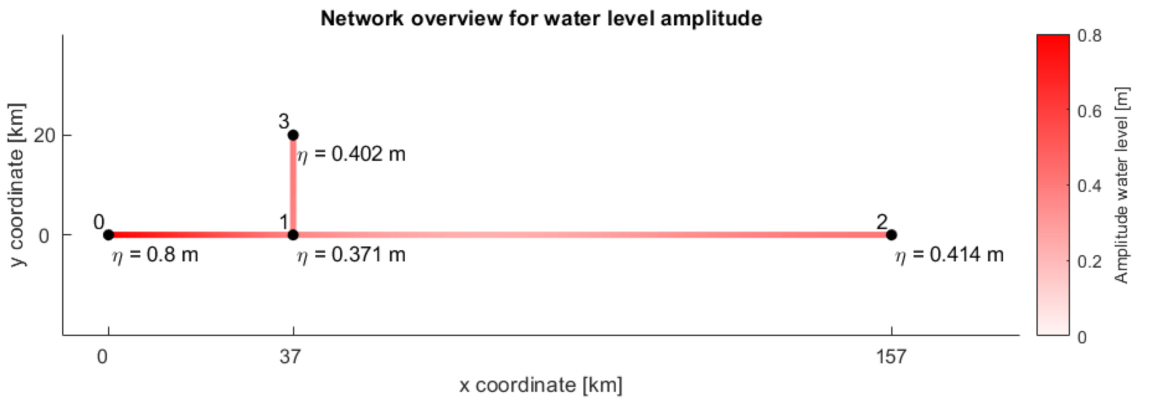

Figure 5.4: Water level amplitudes across the base network

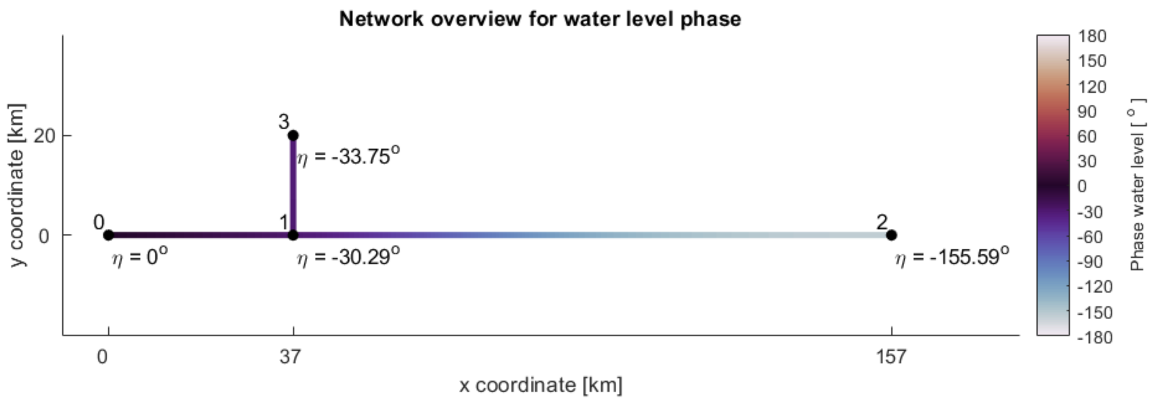

Figure 5.5: Water level phase across the base network

5.2. Variables side channel

This section describes the impact of variations in side channel properties on the phase difference. The properties will be treated in the following order: width, depth, length and friction coefficient.

Certain variables used in the formulation of the analytical model are used to understand the system's behaviour. These are the tidal discharge amplitude in a channel section $\hat{Q}_i$, the relative resistance σ_i and the amplification factor $\hat{\eta}_i/\hat{\eta}_1$. The relative resistance shows how the effective friction changes and when it dominates over the tidal forcing. The amplification factor is the ratio of the water level amplitude at the end of a channel section to the water level amplitude at the junction and is an indication of resonance.

The analytical model results are the sum of two wave systems, one travelling in the positive direction and one in the negative direction, as described in section 3.2.2. The ratio between these wave systems indicates if the wave system transforms to standing of propagating wave patterns.

5.2.1. Width

The impact of the width of the side channel on the phase difference is limited and shows a steady decline with increasing width. Most interestingly the change in phase difference is caused by a change in $\theta_{m,a}$, see figure 5.6a.

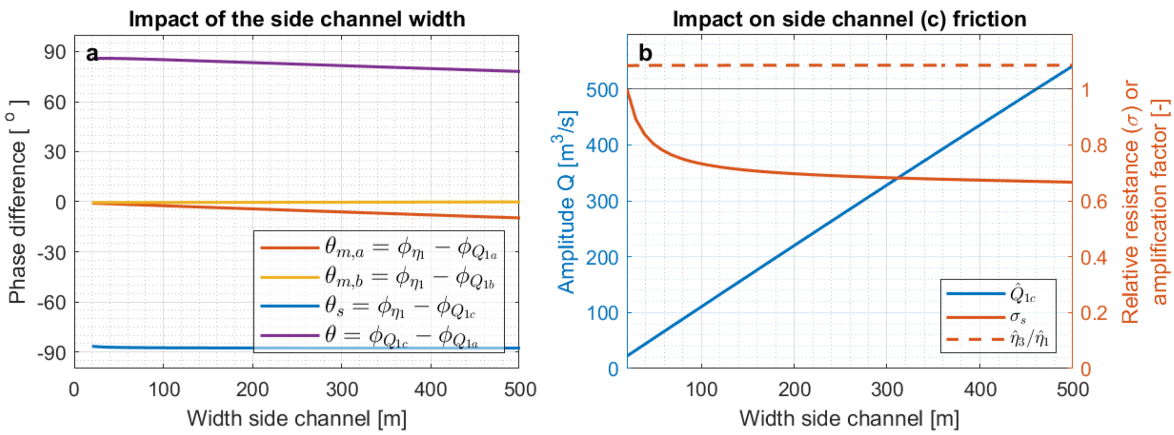

Figure 5.6: Overview of changing parameters for variable width side channel. **(a)** Overview of variations in phase differences. Including phase differences between water level and discharge for each branch at the junction and the phase difference between the discharges at the main and side channels. **(b)** Overview of variations in discharge amplitude, relative resistance and amplification factor for the section between nodes 1 and 3.

The increase in width of the side channel also increases the discharge in the side channel, as can be seen in figure 5.6b. The impact on the main channel is negligible as the changes in the discharge amplitude are around 1%. So, the tidal prism is hardly impacted, which can be explained by the relatively small surface area of the side channel compared to the main channel. The maximum surface area of the side channel is $10 \cdot 10^6$ m^2, while the main channel has a surface area of $125.6 \cdot 10^6$ m^2. So, the increased discharge of the side channel causes a shift in the phase of the main channel as its discharge becomes more significant and forces it towards the phase of the side channel.

The ratio between the wave systems in the side channel is only significantly impacted for small widths (figure 5.7c). For a narrow channel, the width becomes as important as the depth in determining the friction. Additionally, this shows that the width of a channel does not significantly impact the wave type in a channel, which is as expected.

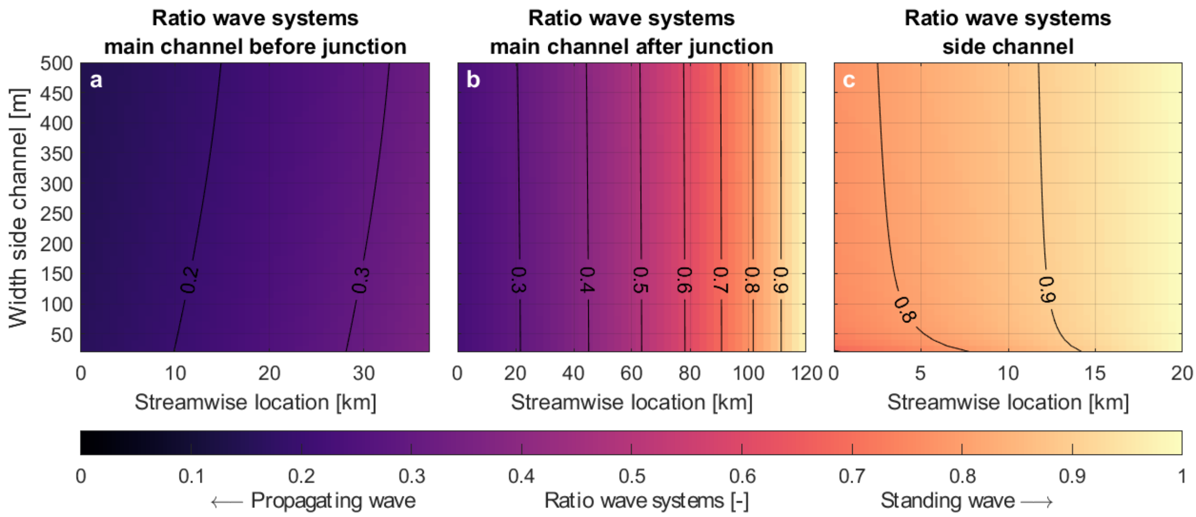

Figure 5.7: Ratio of the two underlying wave systems **(a)** Ratio wave systems between nodes 0 and 1. **(b)** Ratio wave systems between nodes 1 and 2. **(c)** Ratio wave systems between nodes 1 and 3.

5.2.2. Depth

The depth of the side channel only has a significant impact on the phase difference for small depths, see figure 5.8a. The increase in depth causes a decrease in friction in the side channel (figure 5.8b). This allows the formation of a standing wave pattern between the water level and the discharge of the side channel as the phase difference of the side channel goes towards 90° (figure 5.8a).

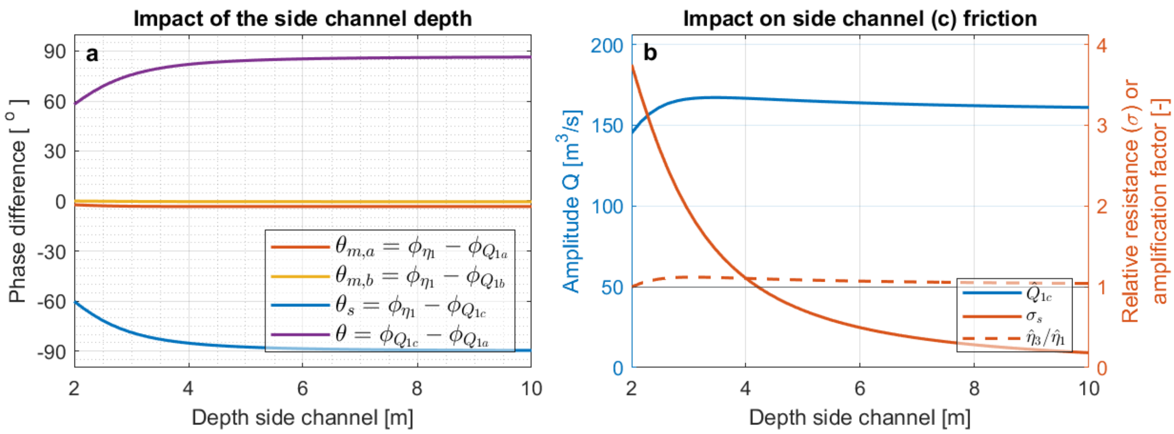

Figure 5.8: Overview of changing parameters for variable depth side channel. **(a)** Overview of variations in phase differences. Including phase differences between water level and discharge for each branch at the junction and the phase difference between the discharges at the main and side channels. **(b)** Overview of variations in discharge amplitude, relative resistance and amplification factor for the section between nodes 1 and 3.

This is also visible in figure 5.9c, as the ratio of the wave systems increases towards 1 as the depth increases. The discharge amplitudes in the main channel are not significantly impacted by the depth of the side channel, as only a change of around 1% occurs. Additionally, the discharge of the side channel is also hardly impacted, until the depth becomes very shallow and the friction becomes increasingly more dominant, which decreases the discharge.

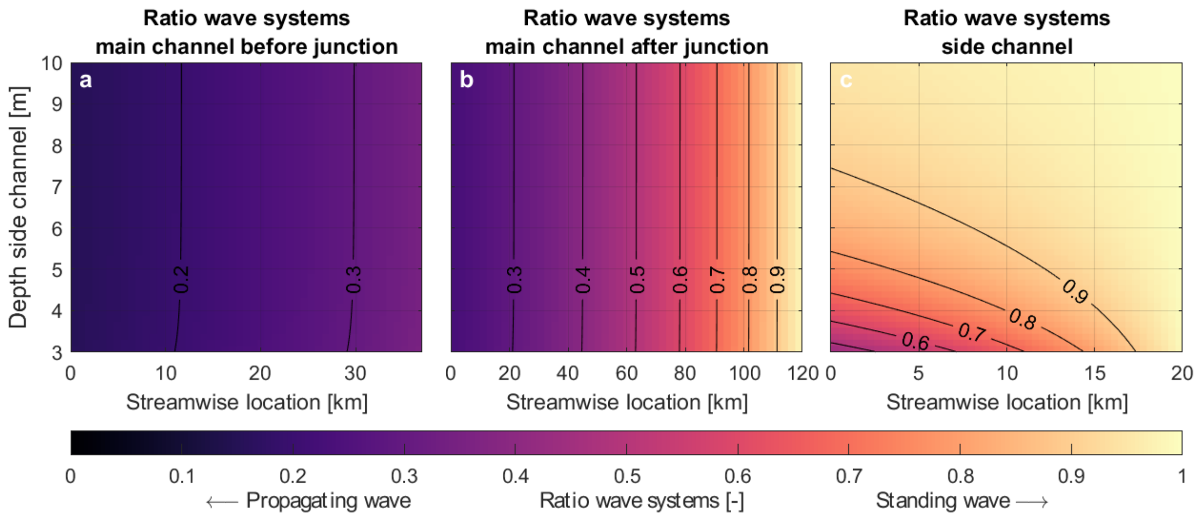

Figure 5.9: Ratio of the two underlying wave systems **(a)** Ratio wave systems between nodes 0 and 1. **(b)** Ratio wave systems between nodes 1 and 2. **(c)** Ratio wave systems between nodes 1 and 3.

5.2.3. Length

The length of the side channel shows the largest change in the phase difference, see figure 5.10a. The increase in side channel length causes an increase in discharge in the side channel, see figure 5.10d. However, the tidal prism entering the network does not change significantly as can be seen by the discharge amplitude in the main channel in figures 5.10b and c. Additionally, the increase in surface area of the side channel is relatively small, as it increases from an initial area of $3 \cdot 10^6$ m^2 to $15 \cdot 10^6$ m^2, while the main channel has a surface area of $125.6 \cdot 10^6$ m^2.

At a side channel length of around 40 km, the water level starts to resonate, as can be seen by the peak in the response factor of the side channel, see figure 5.10d. This matches with the theoretical quarter wavelength of the tide. For shallow water waves at a depth of 5 m, the wavelength equals 313 km, see equation 5.1. A quarter wavelength is 78 km and the distance from the sea to the end of the side channel is $37 + 40 = 77$ km. However, the main channel has a larger depth, which would increase the theoretical wavelength. In addition, the wavelength for which resonance occurs is smaller than the estimated wavelength as the friction reduces the phase speed of the wave (Battjes and Labeur, 2017).

$$\lambda = c \cdot T = \sqrt{g \cdot d} \cdot T = \sqrt{9.81 \cdot 5} \cdot 44700 = 313060 \text{ m} = 313 \text{ km} \tag{5.1}$$

The resonance has an impact on the phase difference of the main channel as well, as is visible in figure 5.10a by the valley in the phase difference $\theta_{m,a}$. This is most likely caused by the larger return wave of the water level, as can be concluded from the amplification factor in figure 5.10d. This forces the phase difference $\theta_{m,a}$ in the channel section between nodes 0 and 1 to become more like the side channel.

The increase in side channel length allows the friction to work along a larger distance, which will decrease the amplitude of the wave system, transforming the solution from a standing wave towards a propagating wave (figure 5.11c).

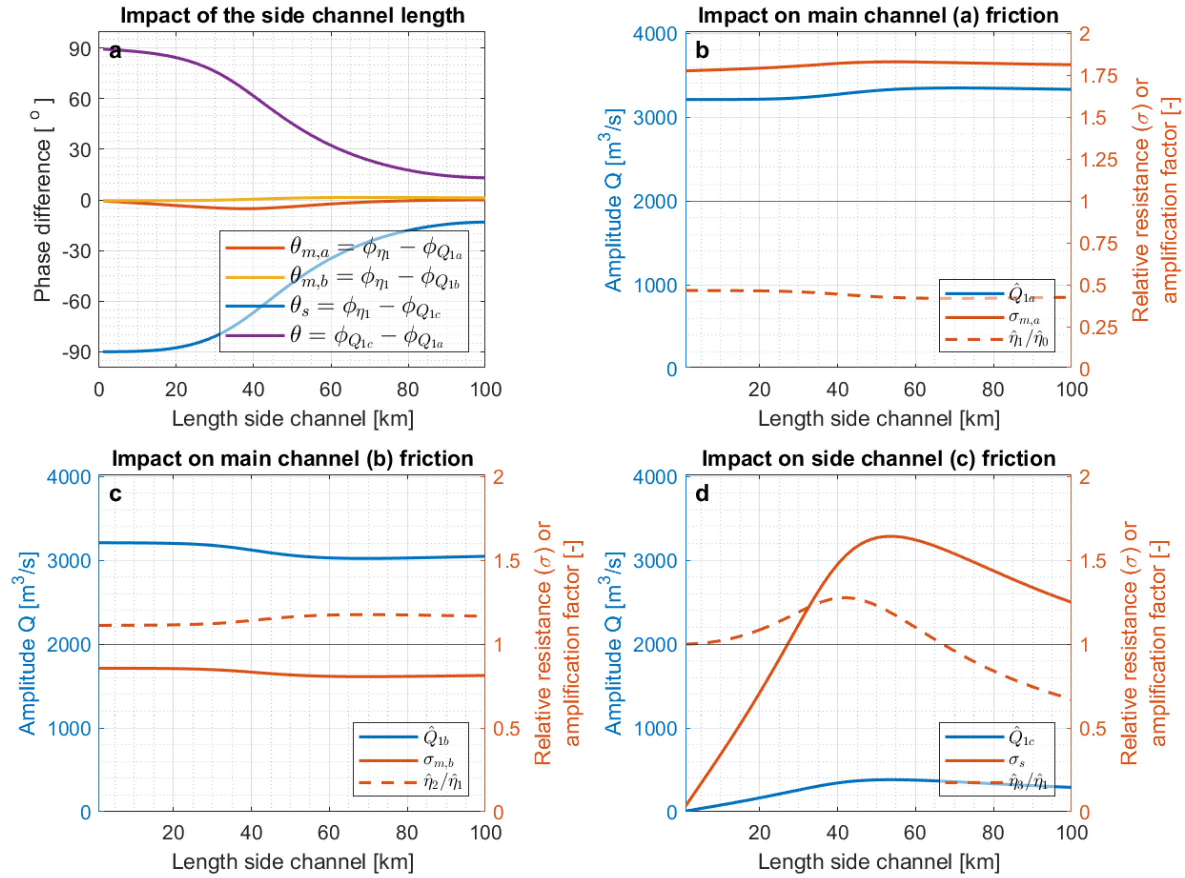

Figure 5.10: Overview of changing parameters for variable length side channel. **(a)** Overview of variations in phase differences. Including phase differences between water level and discharge for each branch at the junction and the phase difference between the discharges at the main and side channels. **(b)** Overview of variations in discharge amplitude, relative resistance and amplification factor for the section between nodes 0 and 1. **(c)** Overview of variations in discharge amplitude, relative resistance and amplification factor for the section between nodes 1 and 2. **(d)** Overview of variations in discharge amplitude, relative resistance and amplification factor for the section between nodes 1 and 3.

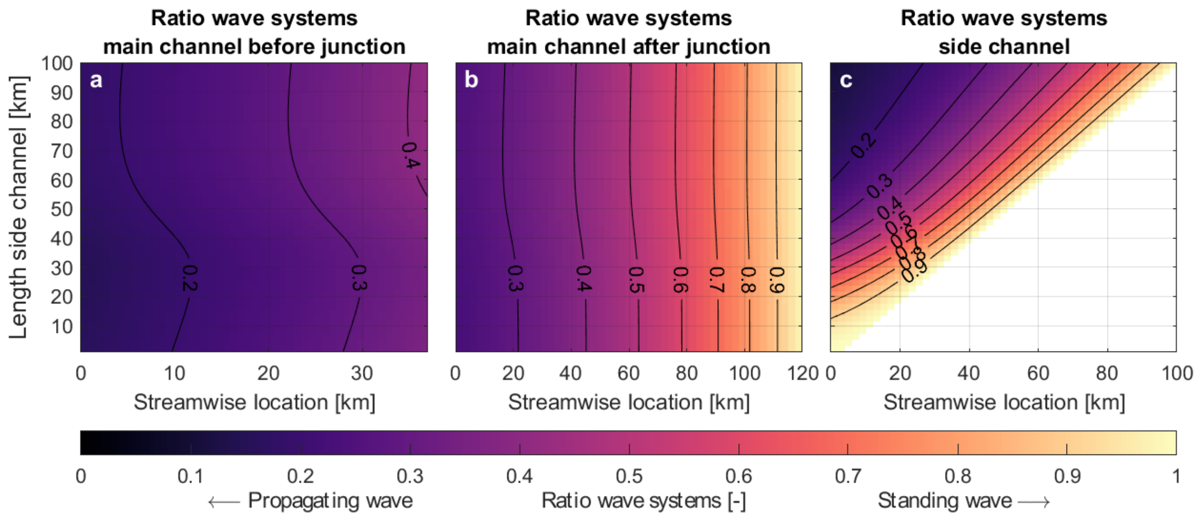

Figure 5.11: Ratio of the two underlying wave systems **(a)** Ratio wave systems between nodes 0 and 1. **(b)** Ratio wave systems between nodes 1 and 2. **(c)** Ratio wave systems between nodes 1 and 3.

5.2.4. Friction coefficient

The friction coefficient for the side channel is tested for a range between 0.001 and 0.01. This equates roughly to a Chezy friction coefficient of 100 and 30 m$^{1/2}$/s. Overall the change in friction resulted in hardly any change in the phase difference for this initial network as visible in figure 5.12a.

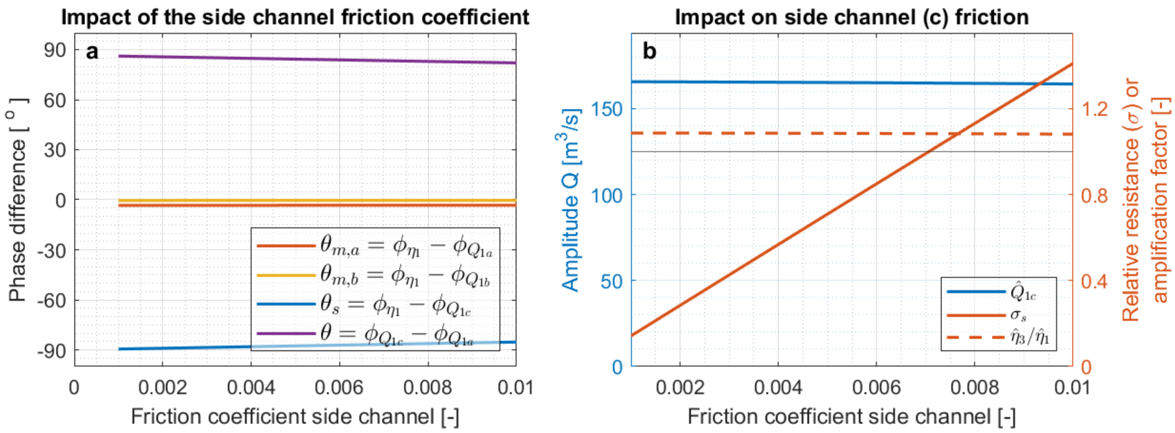

Figure 5.12: Overview of changing parameters for variable friction coefficient of the side channel. **(a)** Overview of variations in phase differences. Including phase differences between water level and discharge for each branch at the junction and the phase difference between the discharges at the main and side channels. **(b)** Overview of variations in discharge amplitude, relative resistance and amplification factor for the section between nodes 1 and 3.

The increase in friction (figure 5.12b) dampens the outgoing and returning waves in the side channel. This reduces the contribution of the returning wave toward the total solution (figure 5.13c), so it transforms into a propagating wave. However, the amplitude of the discharge in all channels changes by less than 1%, so the friction coefficient has no significant impact on the rest of the system.

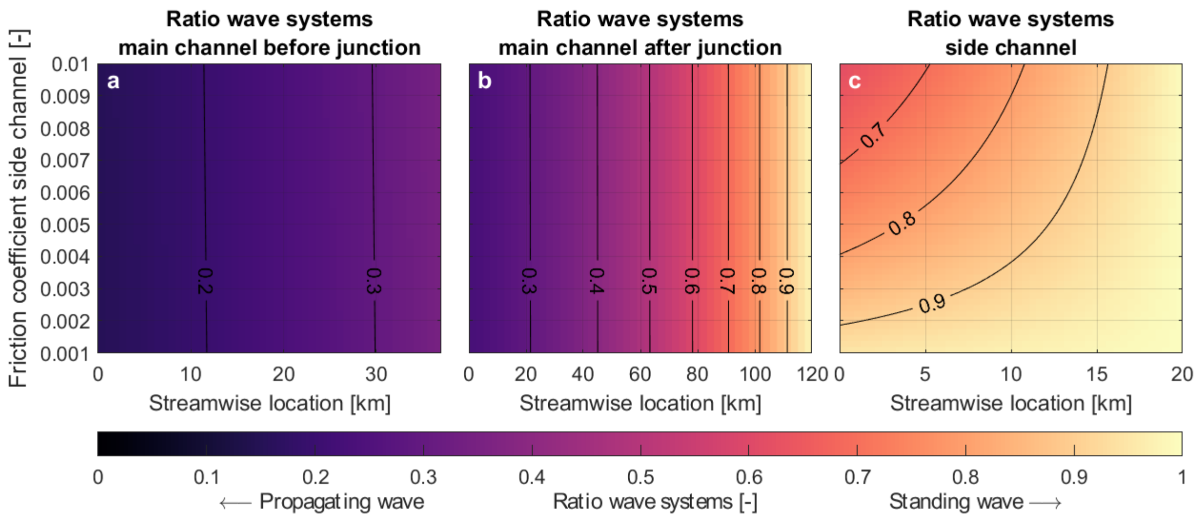

Figure 5.13: Ratio of the two underlying wave systems **(a)** Ratio wave systems between nodes 0 and 1. **(b)** Ratio wave systems between nodes 1 and 2. **(c)** Ratio wave systems between nodes 1 and 3.

5.3. Variables main channel

This section describes the impact of variations in main channel geometry on the phase difference. The properties will be treated in the following order: width, depth and friction coefficient. The length is not investigated for the main channel, as in reality, this is the connection to the remainder of the delta and does not change.

5.3.1. Width

The main channel width has only a noticeable impact on the main channel before the junction. The phase difference increases as the main channel becomes wider, see figure 5.14a. The discharge in the entire main channel increases linearly with the increase in width (figure 5.14b), as the tidal prism increases. The width has a significant impact on the tidal prism as it increases the surface area of the main channel from $15.7 \cdot 10^6$ m^2 to $188.4 \cdot 10^6$ m^2.

When the width of the main channel increases, the impact of the side channel becomes smaller. So, for smaller widths of the main channel, the phase difference between the discharges is forced towards the phase difference of the side channel, which reduces the phase difference.

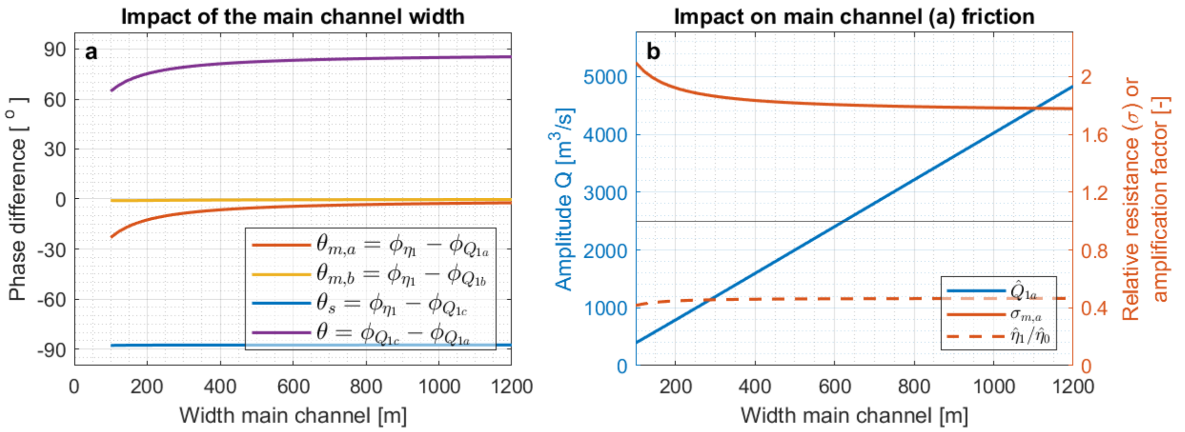

Figure 5.14: Overview of changing parameters for variable width main channel. **(a)** Overview of variations in phase differences. Including phase differences between water level and discharge for each branch at the junction and the phase difference between the discharges at the main and side channels. **(b)** Overview of variations in discharge amplitude, relative resistance, and amplification factor for the section between nodes 0 and 1.

The width of the main channel is shown to have little impact on the ratio of the wave systems in the main channel after the junction, see figure 5.15b. So, the propagating wave in the main channel remains propagating. The limited change in relative resistance is due to a balance between the increase in amplitude and the decrease in friction as the width increases. Additionally, the shift of the main channel before the junction towards the side channel is visible in figure 5.15a.

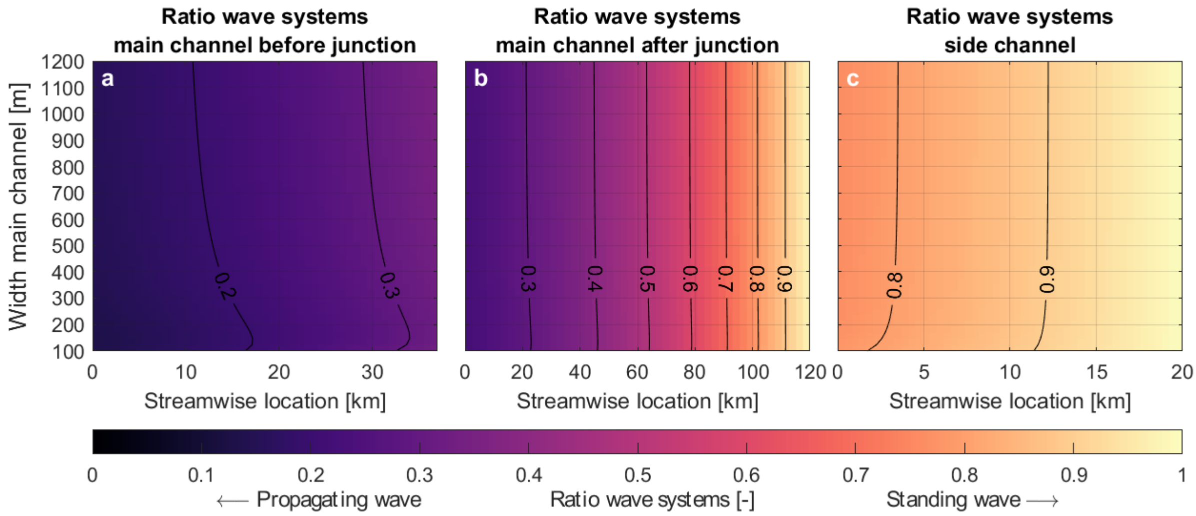

Figure 5.15: Ratio of the two underlying wave systems **(a)** Ratio wave systems between nodes 0 and 1. **(b)** Ratio wave systems between nodes 1 and 2. **(c)** Ratio wave systems between nodes 1 and 3.

5.3.2. Depth

The impact of the depth of the main channel is more significant for the phase difference. The increase in depth leads to an increase in the discharge in the main and side channels. In the main channel, the relative resistance decreases (figure 5.16b), thus the change in depth is more important than the change in discharge amplitude. Figure 5.16a shows that the increase in depth for a shallow channel results in an increase in the phase difference. However, as the amplification factor becomes larger than 1 in the main channel after the junction (figure 5.16c), the phase difference starts to decrease again as is visible in figure 5.16a.

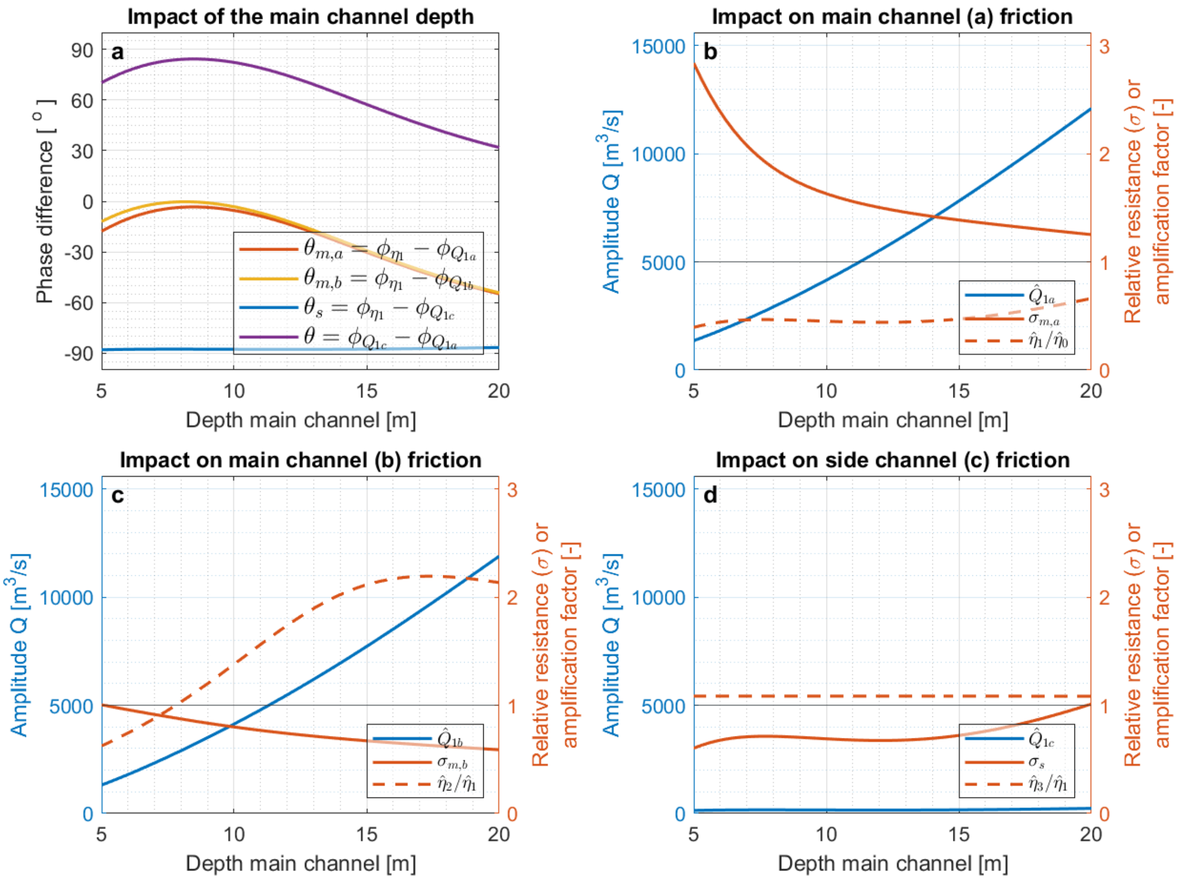

Figure 5.16: Overview of changing parameters for variable depth main channel. **(a)** Overview of variations in phase differences. Including phase differences between water level and discharge for each branch at the junction and the phase difference between the discharges at the main and side channels. **(b)** Overview of variations in discharge amplitude, relative resistance and amplification factor for the section between nodes 0 and 1. **(c)** Overview of variations in discharge amplitude, relative resistance and amplification factor for the section between nodes 1 and 2. **(d)** Overview of variations in discharge amplitude, relative resistance and amplification factor for the section between nodes 1 and 3.

Around a depth of 17 m resonance occurs in the main channel, as can be seen in the amplification factor of the main channel after the junction (figure 5.16c). This matches with the theoretical quarter wavelength. For shallow water waves, the wavelength is 577 km, see equation 5.2. Calculating the ratio of channel length to wavelength gives $L_m/\lambda = 0.27$. This is very close to a quarter wavelength for which resonance is expected. The difference between the two values can be attributed to the friction, which reduces the wave speed.

$$\lambda = c \cdot T = \sqrt{g \cdot d} \cdot T = \sqrt{9.81 \cdot 17} \cdot 44700 = 577253 \text{ m} = 577 \text{ km} \tag{5.2}$$

The impact of the decrease in friction which was mentioned previously, is also visible in the ratio of the wave systems. Both sides of the main channel transform in the direction of a standing wave pattern as the depth increases, see figures 5.17a and b.

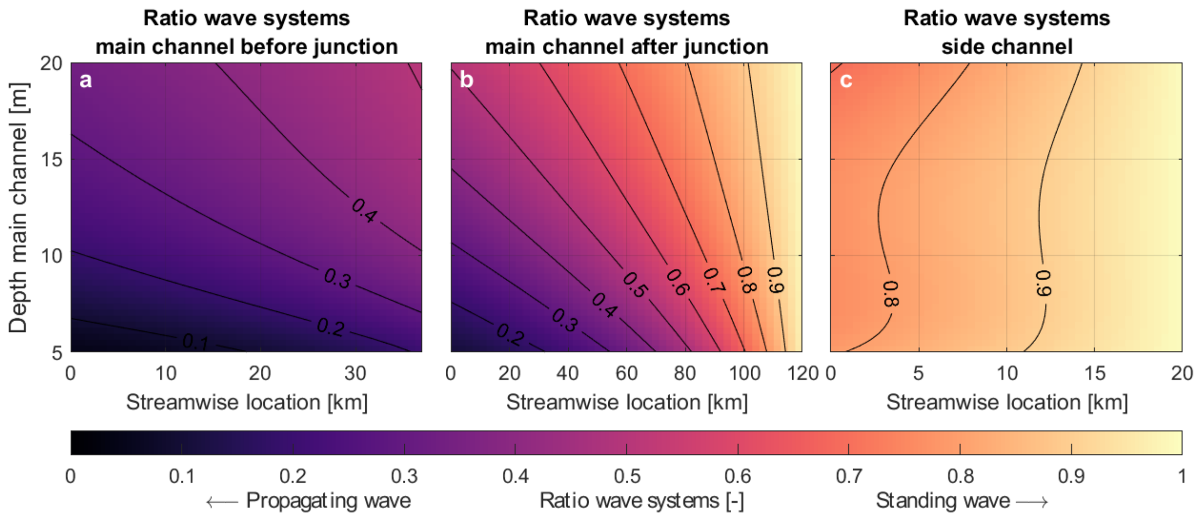

Figure 5.17: Ratio of the two underlying wave systems **(a)** Ratio wave systems between nodes 0 and 1. **(b)** Ratio wave systems between nodes 1 and 2. **(c)** Ratio wave systems between nodes 1 and 3.

5.3.3. Friction coefficient

The phase difference decreases as the phase differences $\theta_{m,a}$ and $\theta_{m,b}$ decrease for larger friction values (figure 5.18a). An increase in the friction coefficient results in a decrease in the discharge in the main channel, as can be seen in figures 5.18b and c. A higher relative resistance makes it harder for the tide to enter the system, decreasing the discharge.

Furthermore, a lower friction coefficient increases the importance of the return wave and allows for a standing wave pattern in the main channel after the junction (figure 5.19b). The greater return wave also increases the return wave in the main channel before the junction (figure 5.19a), making the total solution more like a standing wave.

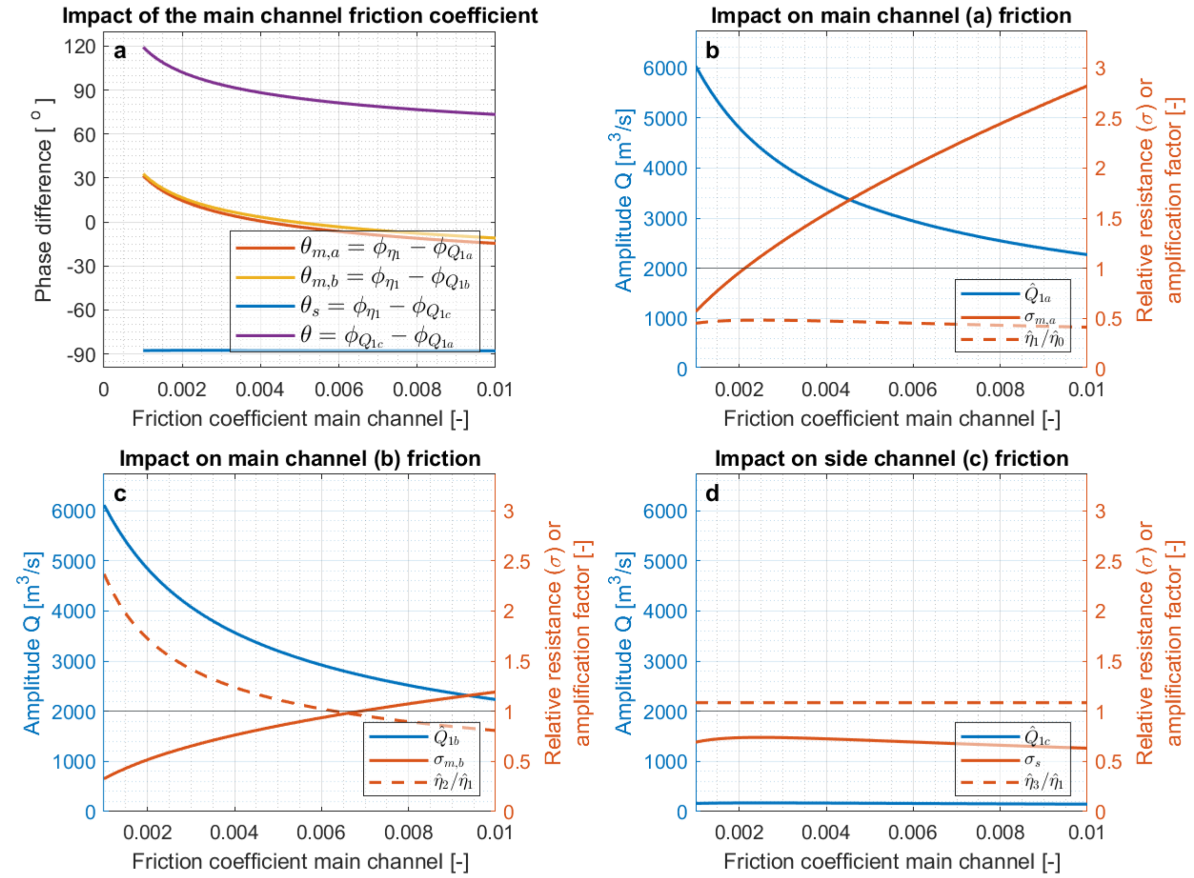

Figure 5.18: Overview of changing parameters for variable friction coefficient of the main channel. **(a)** Overview of variations in phase differences. Including phase differences between water level and discharge for each branch at the junction and the phase difference between the discharges at the main and side channels. **(b)** Overview of variations in discharge amplitude, relative resistance and amplification factor for the section between nodes 0 and 1. **(c)** Overview of variations in discharge amplitude, relative resistance and amplification factor for the section between nodes 1 and 2. **(d)** Overview of variations in discharge amplitude, relative resistance and amplification factor for the section between nodes 1 and 3.

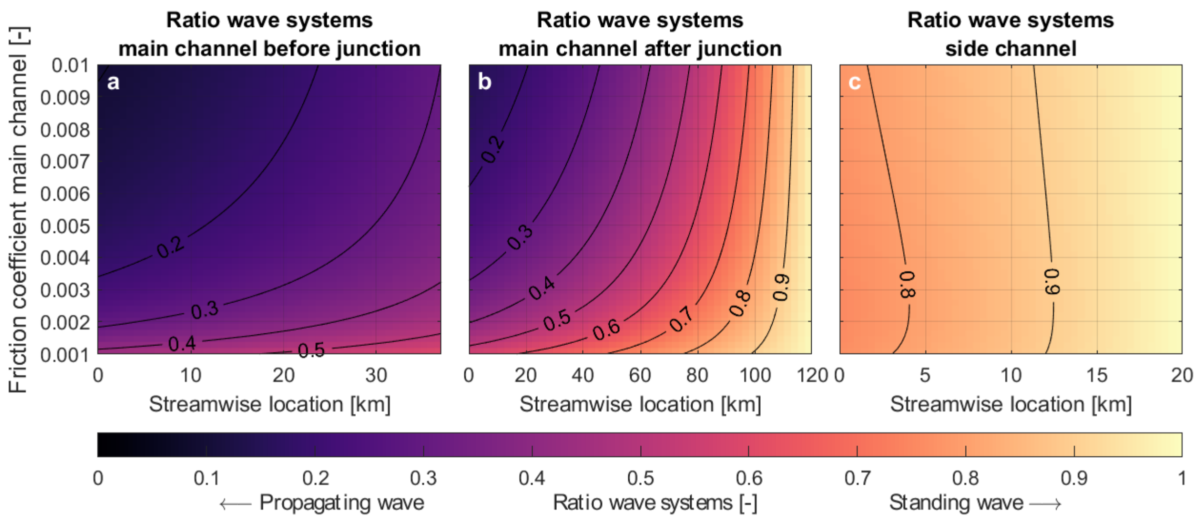

Figure 5.19: Ratio of the two underlying wave systems **(a)** Ratio wave systems between nodes 0 and 1. **(b)** Ratio wave systems between nodes 1 and 2. **(c)** Ratio wave systems between nodes 1 and 3.

5.4. Variables boundary conditions

This section describes the impact of variations in the boundary conditions on the phase difference. The boundary conditions will be treated in the following order: tidal amplitude, discharge at the end of the main channel and discharge at the end of the side channel.

5.4.1. Tidal amplitude

The change in the amplitude of the tide at the boundary is a representation of the spring-neap cycle of the tide. This process has a significant impact on the phase difference, see figure 5.20a. The increase in amplitude increases the tidal prism and thus the discharge in the main and side channels, as shown in figures 5.20b, c and d.

The phase difference in the main channel $\theta_{m,a}$ and $\theta_{m,b}$ are not approaching zero as these are at the junction and not at a channel end.

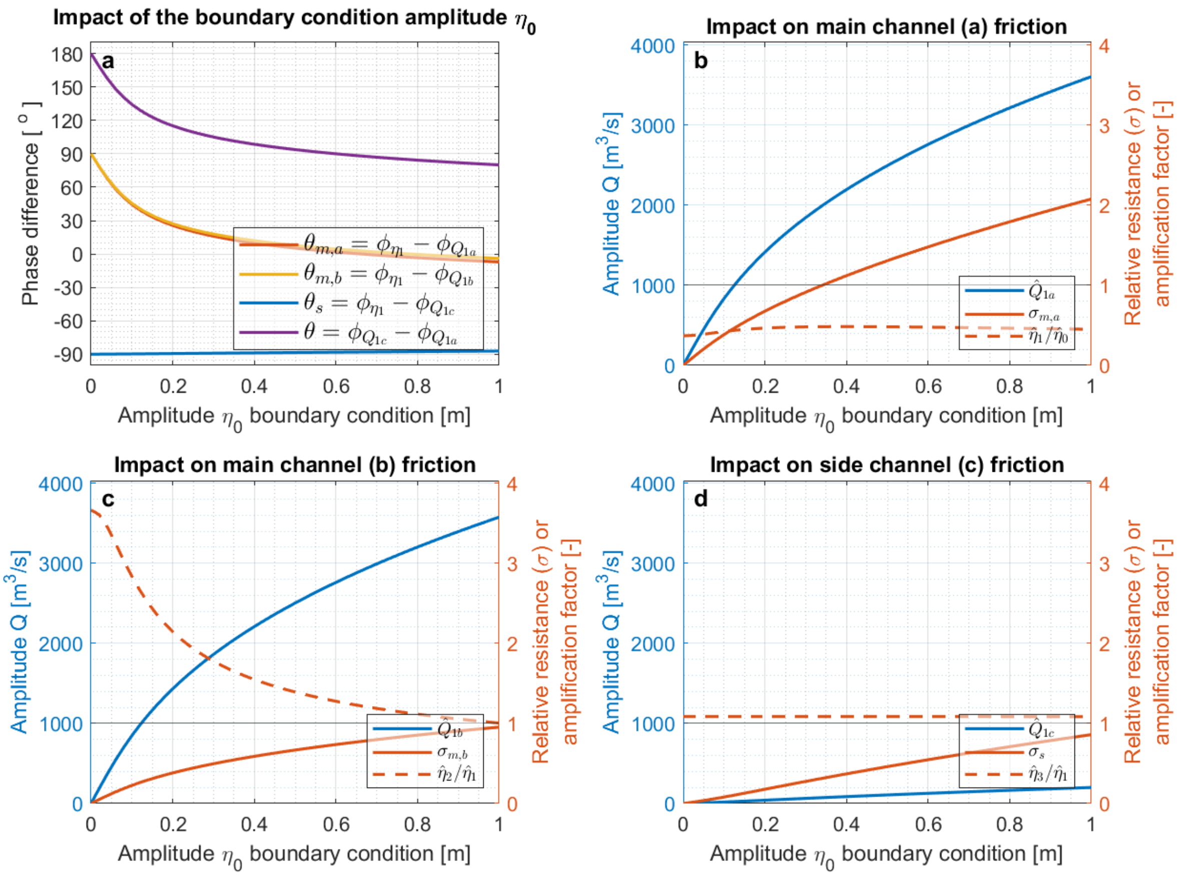

Figure 5.20: Overview of changing parameters for variable water level amplitude at the seaside boundary. **(a)** Overview of variations in phase differences. Including phase differences between water level and discharge for each branch at the junction and the phase difference between the discharges at the main and side channels. **(b)** Overview of variations in discharge amplitude, relative resistance and amplification factor for the section between nodes 0 and 1. **(c)** Overview of variations in discharge amplitude, relative resistance and amplification factor for the section between nodes 1 and 2. **(d)** Overview of variations in discharge amplitude, relative resistance and amplification factor for the section between nodes 1 and 3.

The previously mentioned increased discharge amplitude causes an increase in friction and transforms the wave more towards propagation. In the ratio of the wave systems, this is visible as a decreased ratio for larger tidal amplitudes, see figure 5.21.

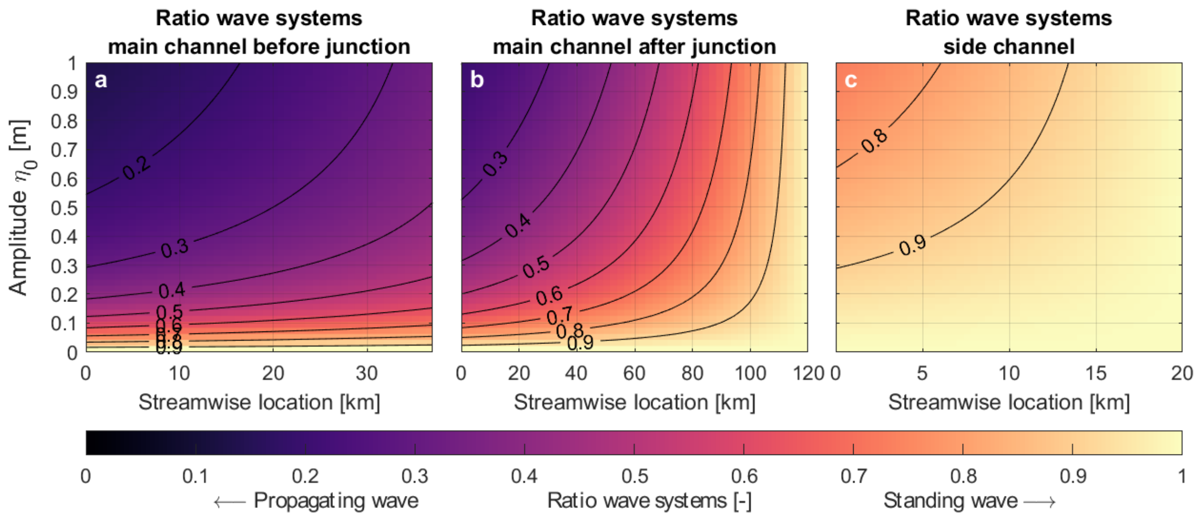

Figure 5.21: Ratio of the two underlying wave systems **(a)** Ratio wave systems between nodes 0 and 1. **(b)** Ratio wave systems between nodes 1 and 2. **(c)** Ratio wave systems between nodes 1 and 3.

5.4.2. Discharge main channel

The positive direction of the system is defined from low number nodes to higher number nodes. Thus an increasingly negative discharge increases the discharge entering the system at the boundary. Furthermore, in the figures related to the discharge amplitude in a section, only the impact on the tidal discharge is shown.

Figure 5.22a shows an increasing discharge reduces the phase difference. The tidal amplitude in the main channel decreases as a larger discharge enters the system, see figure 5.22b. The additional discharge increases the friction in the main channel and works against the tide trying to enter the system.

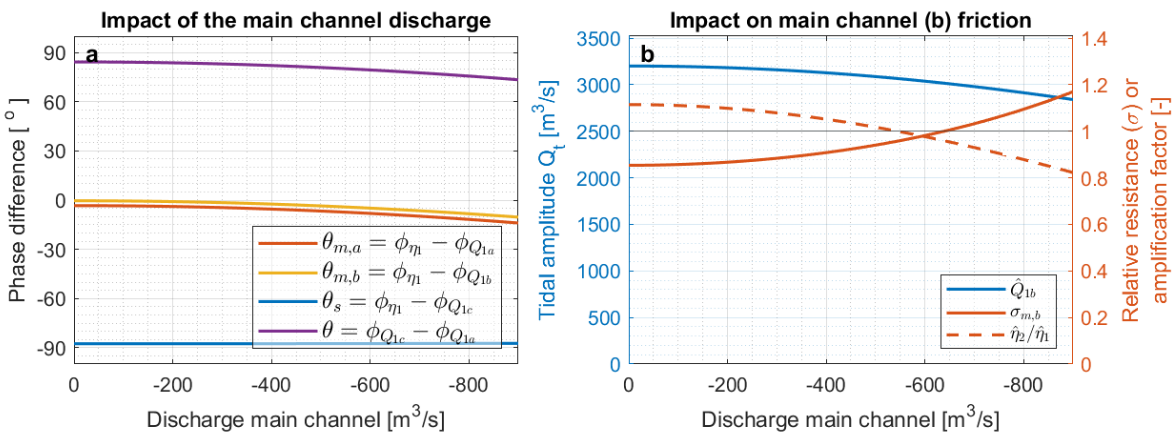

Figure 5.22: Overview of changing parameters for variable discharge at the end of the main channel. **(a)** Overview of variations in phase differences. Including phase differences between water level and discharge for each branch at the junction and the phase difference between the discharges at the main and side channels. **(b)** Overview of variations in discharge amplitude, relative resistance and amplification factor for the section between nodes 1 and 2.

The ratio of the wave systems reduces as the discharge in the main channel increases, see figures 5.23a and b. This can be explained by the increase in relative resistance as the discharge increases. The outgoing wave is more damped and thus the returning wave is also reduced in amplitude.

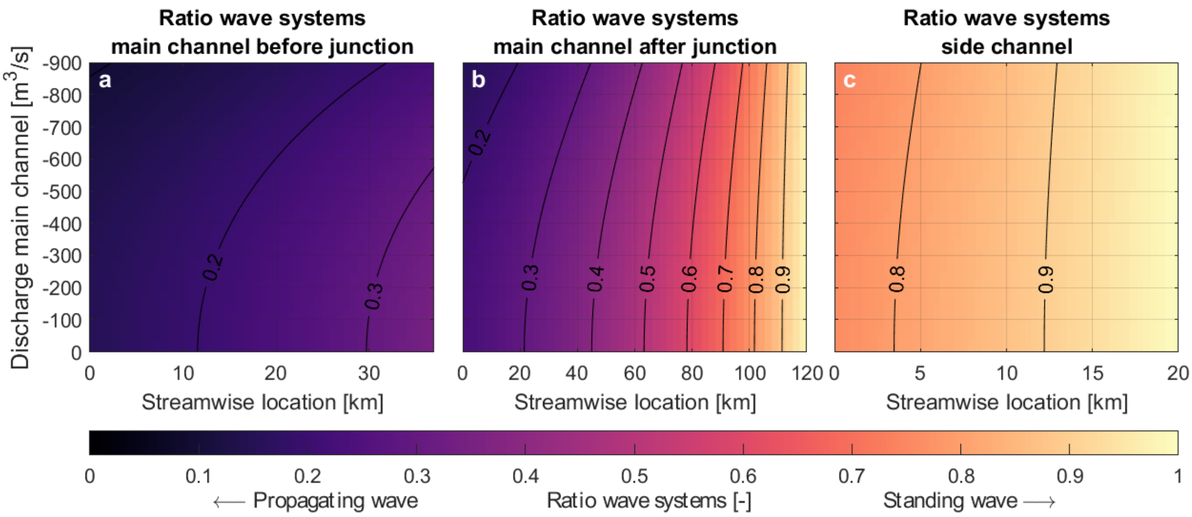

Figure 5.23: Ratio of the two underlying wave systems **(a)** Ratio wave systems between nodes 0 and 1. **(b)** Ratio wave systems between nodes 1 and 2. **(c)** Ratio wave systems between nodes 1 and 3.

5.4.3. Discharge side channel

The impact of the discharge at the end of the side channel on the phase difference is very limited, as shown in figure 5.24a. This is mainly related to the size of the discharge compared to the tidal discharge. The side channel boundary is tested for both extraction and insertion. As parameters like friction are not dependent on the direction of the flow the results are mirrored at the zero discharge line, see figure 5.24b.

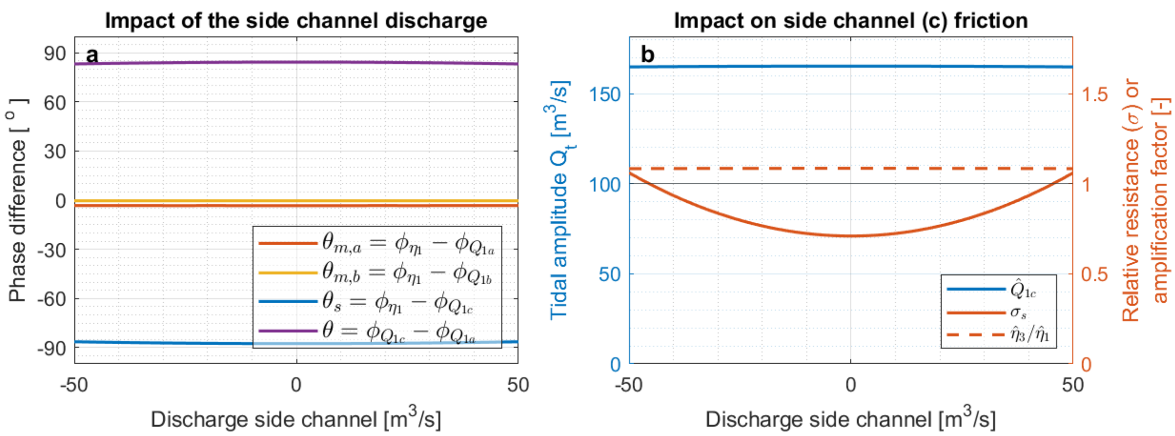

Figure 5.24: Overview of changing parameters for variable discharge at the end of the side channel. **(a)** Overview of variations in phase differences. Including phase differences between water level and discharge for each branch at the junction and the phase difference between the discharges at the main and side channels. **(b)** Overview of variations in discharge amplitude, relative resistance and amplification factor for the section between nodes 1 and 3.

5.5. Impact variable combinations

The impact of the main channel variables has hardly any impact on the phase difference in the side channel, thus a combination between a main channel and a side channel variable does not change the pattern of the phase difference. Figure 5.25 shows that the most interesting cases are the side channel's length combined with the side channel's friction coefficient or depth. It becomes clear that the impact of the width of the side channel is very small (figure 5.25a). The lines of the phase difference almost overlap for different initial widths of the side channel.

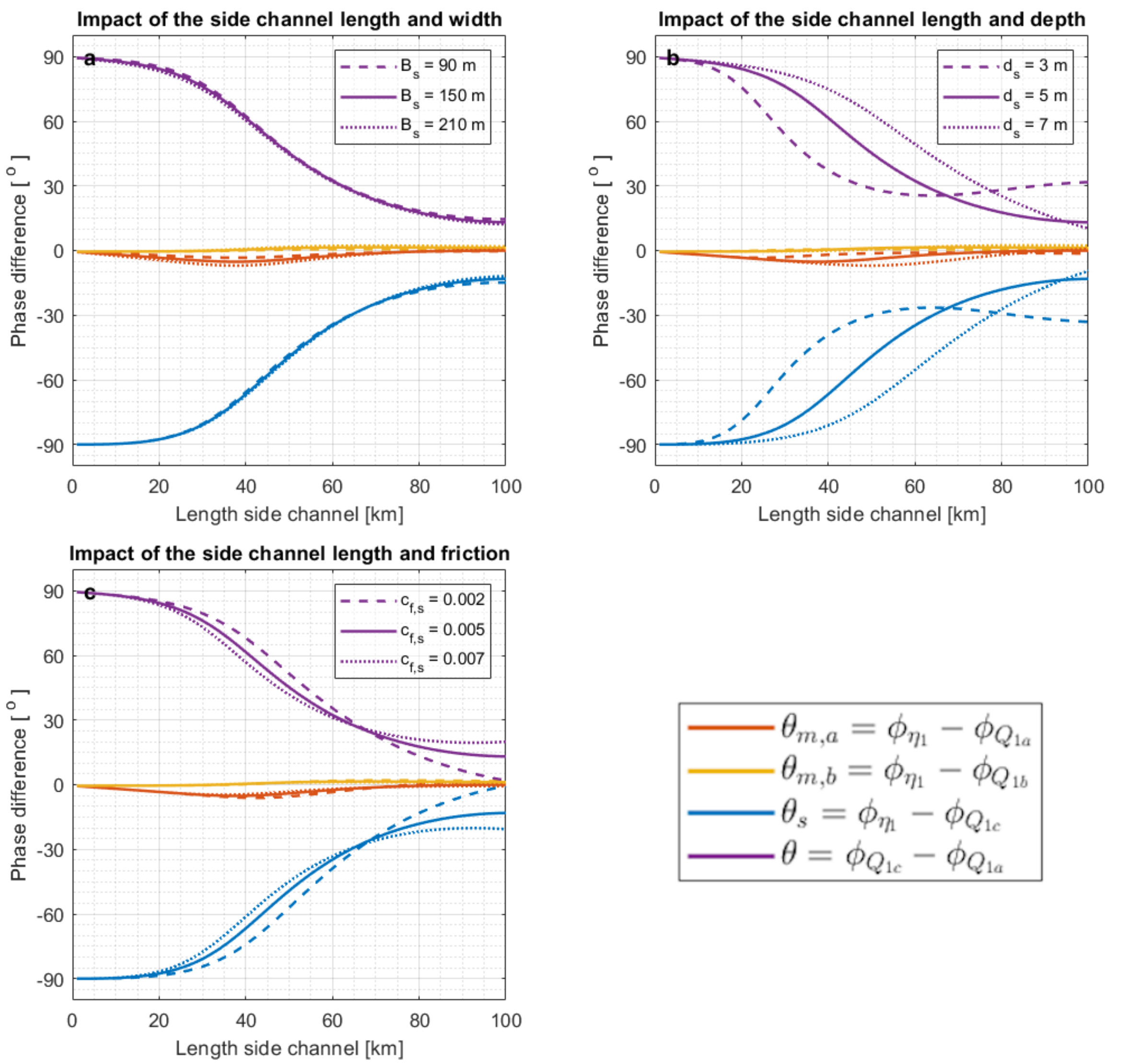

Figure 5.25: Combinations of side channel parameters and their combined impact on the phase differences. **(a)** Impact of side channel length in combination with multiple side channel widths. **(b)** Impact of side channel length in combination with multiple side channel depths. **(c)** Impact of side channel length in combination with multiple side channel friction coefficients.

With increasing depth, the phase difference remains greater as the friction is decreased and the standing wave pattern can exist in longer channels. This is visible in the phase difference of the side channel, which remains around 90° for larger lengths, see figure 5.25b. However, for very long lengths, the phase difference becomes smaller compared to shallower depths. The change in shape can be explained by the occurrence of resonance. The wavelength in a shallow channel of 3 m is 242 km. So, at a quarter wavelength of around 60 km resonance occurs and in figure 5.25b the extreme value is located around this length.

$$\lambda = c \cdot T = \sqrt{g \cdot d} \cdot T = \sqrt{9.81 \cdot 3} \cdot 44700 = 242495 \text{ m} = 242 \text{ km} \tag{5.3}$$

The opposite pattern is visible for the friction coefficient of the side channel, as an increased friction coefficient increases the friction (figure 5.25c). Figure 5.25b further shows that the impact of the depth can be much more significant depending on the side channel length. This makes the depth and friction coefficient a more significant variable compared to the width, which is expected.

The length, depth and friction coefficient are important for the type of wave that can exist in a semi-closed channel. They have a large impact on the relative resistance and thus on the formation of standing or propagating waves.

The impact of a variable on the phase difference is strongly dependent on the initial geometry. Thus, the length of the main channel also determines the impact of the other geometry properties of the main channel. So, adaptations to these variables impact the change in the phase difference and thus the effectiveness of the measure.

5.6. Conclusion

The phase difference of the M2 tide is investigated in a single junction network. The impact of the following variables is investigated, for the side channel: width, depth, length and friction coefficient, for the main channel: width, depth and friction coefficient and for the boundary conditions: tidal amplitude, discharge main channel and discharge side channel.

For the side channel, an increase in width results in an increased discharge amplitude in the side channel. So, the impact of the side channel becomes larger compared to the main channel after the junction, forcing the phase difference towards the current phase difference of the side channel. An increase in depth lowers the friction in the side channel, which transforms the wave in the channel from propagating to standing. It transforms to a standing wave pattern as the wave system is damped less. This process causes an increase in the phase difference. An increase in length causes a decrease in phase difference, as the wave transforms from standing towards propagating. The wave system in the side channel experiences friction along a larger distance, transforming the wave pattern. In addition, the side channel length determines if resonance can occur and the length is the variable with the largest impact on the phase difference. An increase in the friction coefficient transforms the wave from standing to propagating, which reduces the phase difference.

For the main channel an increase in width results in an increase in tidal prism. So, for smaller widths, the side channel becomes more significant. This forces the phase difference of the main channel before the junction towards the phase of the side channel, which decreases the phase difference as the width becomes smaller. An increase in depth results in a decrease in friction. This decreases the phase difference as the wave system in the main channel transforms to standing. This initial main channel length, combined with a depth of around 17 m also allows resonance to occur. An increase in friction coefficient causes an increase in friction transforming the wave from standing towards propagating, which decreases the phase difference.

For the boundary conditions, an increase in tidal amplitude causes an increase in tidal prism. This causes an increase in friction and transforms the wave system in the channels towards propagating, which decreases the phase difference. Both the side and main channel river discharge impact the friction and a larger river discharge increases friction and reduces the phase difference.

Quantitative results have been obtained for all the variables and can be found in this chapter. The actual impact of each variable depends on the initial geometry of the system. Larger changes in the phase difference are expected when changes in the geometry allow for resonance to occur.

Part III

A multi-branch system: The Rhine Meuse Delta

6 Background information RMD

The previous chapter described the general behaviour of the phase difference for a change in the geometry or boundary condition. This chapter shifts the focus to the Rhine Meuse Delta and gives background information regarding forcing conditions, and salt intrusion mechanisms in the Hollandsche IJssel. Furthermore, it presents how a phase difference currently impacts the Rhine Meuse Delta. Section 6.1 presents the discharge distribution in the RMD network for different boundary conditions. Followed by a description of the processes that cause the salinization of the Hollandsche IJssel and the current measures in section 6.2.

6.1. Tides and discharges in the Rhine Meuse Delta

The Rhine Meuse Delta can be seen as a network of channels. The discharges in these channels change significantly depending on the season and weather conditions. Figure 6.1 shows the discharges for multiple river discharges in the RMD.

During high river discharges the transport of water to the Noordzee is well split between the Nieuwe Waterweg and the Haringvliet. Furthermore, the discharge in the Lek increases significantly and causes an increase in discharge through the Nieuwe Maas towards the Nieuwe Waterweg.

During low river discharges, almost all transport to the Noordzee is handled by the Nieuwe Waterweg. The discharge in the Lek reduces to approximately 0 m^3/s and the main route is via the Nieuwe Merwede and the Oude Maas towards the Nieuwe Waterweg. So, the discharge through the Nieuwe Maas is reduced significantly.

A storm surge causes a large inland transport of water in the Nieuwe Waterweg. This continues mostly through the Oude Maas and the Haringvliet. However, a significant part is also transported into the Nieuwe Maas towards the Lek. As the discharge in the Lek is limited the landward transport can continue via the Noord towards the Haringvliet. So, storm surges play an important role in the salinization of the Rhine Meuse Delta as salt water is transported landward.

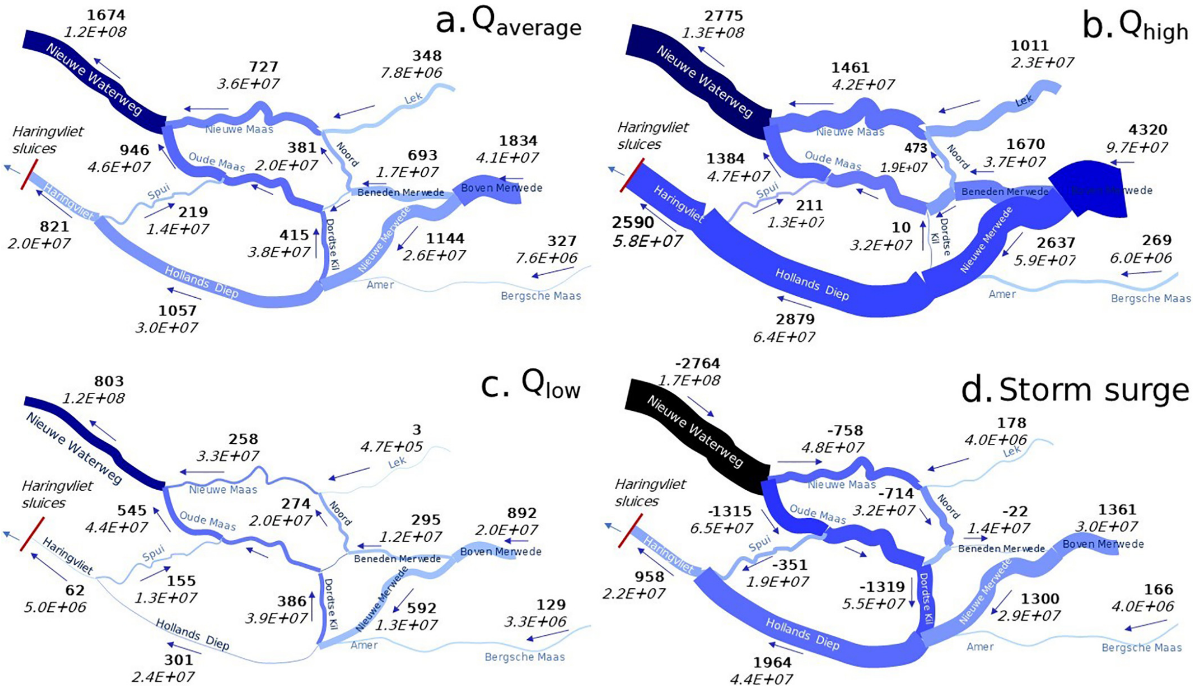

Figure 6.1: For each section the discharge [m^3/s] is shown in bold and the tidal volume [m^3] in italics. The width of the section is proportional to the discharge and the darkness of the section to the tidal volume. The arrows indicate the net flow direction. **(a)** normal tidal conditions with average river discharge. **(b)** normal tidal conditions with high river discharge. **(c)** normal tidal conditions with low river discharge. **(d)** Storm surge with normal river discharge. The values were extracted for two tidal cycles from the SOBEK run for 2013. Figure retrieved from Cox et al. (2021)

6.2. Hollandsche IJssel

The Hollandsche IJssel is a closed side channel of the Nieuwe Maas. The channel is around 20 km long and starts at Gouda and ends at Krimpen aan den IJssel, where it flows into the Nieuwe Maas. At Gouda, the channel is closed off by the pumping station Pijnacker Hordijk and the locks Julianasluis and Waaiersluis. A small side channel in the Hollandsche IJssel is located just before joining the Nieuwe Maas. This side channel, called the Sliksloot, also connects the Hollandsche IJssel with the Nieuwe Maas.

The discharge in the Hollandsche IJssel is the sum of the discharge originating from the regional system surrounding Gouda and the discharges and withdrawals from the inlets along the Hollandsche IJssel. Measurements taken between July and December 2018 show a range of net discharges between -30 m^3/s and 50 m^3/s, as is visible in figure 6.2.

The Hollandsche IJssel is important in the freshwater provision of the area surrounding Gouda. The freshwater inlets along the Hollandsche IJssel should stay fresh, or these inlets cannot be used. This is the main reason why the salinization of the Hollandsche IJssel is unwanted.

The withdrawal of water from these inlets can pull the salt further upstream in the Hollandsche IJssel. During a negative netto discharge or withdrawal of more than 15 m^3/s, the Hollandsche IJssel can salinize completely within days. A netto discharge of 0 – 1 m^3/s requires 10-14 days before the Hollandsche IJssel is fully salinized (Laan et al., 2021).

There are roughly two regimes regarding the salinization of the Hollandsche IJssel. The transport is called advective when it happens with the cross-sectional averaged tidal velocity and dispersive when it is caused by mixing processes like turbulence, wind, density currents, and variations over the width. Near Krimpen aan den IJssel is the transport of salt dominated by tidal advection. In the case of no withdrawal, the salt can only reach the upstream part of the Hollandsche IJssel by dispersive processes, see figure 6.3. The regimes are determined by the distance the tide can travel from the mouth based on the difference in high and low water levels.

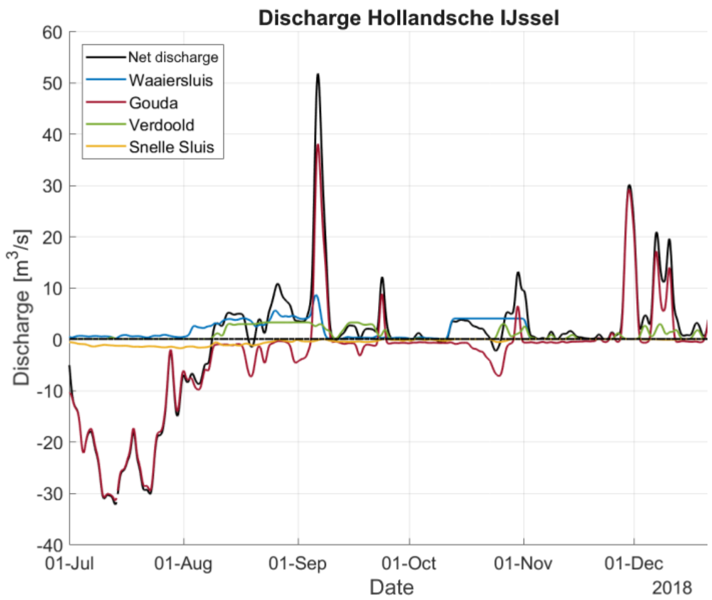

Figure 6.2: Discharges in the Hollandsche IJssel. Positive discharges are directed seaward and negative discharges mean withdrawal. Figure retrieved from Van der Wijk et al. (2019)

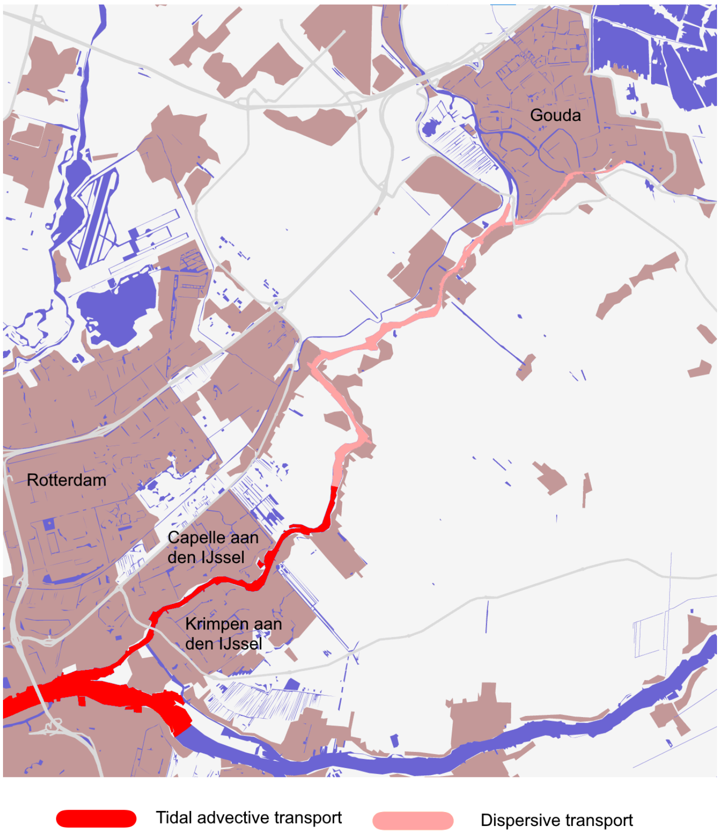

Figure 6.3: Indication of the dominant salt transport mechanism in the Hollandsche IJssel. Red indicates tidal advective transport, and pink indicates dispersive transport

As stated in the introduction Laan et al. (2021) showed that currently, a phase difference between the Nieuwe Maas and Hollandsche IJssel limits the salt intrusion in the Hollandsche IJssel. This is because the phase of the Hollandsche IJssel leads the phase in the Nieuwe Maas. This means that towards the end of the flood, the Hollandsche IJssel starts flowing back into the Nieuwe Maas. So, the highest salt concentrations, which occur at the end of the flood, cannot enter the Nieuwe Maas. However, Laan et al. (2021) found that there are two ways for the Hollandsche IJssel to salinize. The first is due to high salt concentrations during ebb at Brienenoord. The second is due to the contribution of the Sliksloot. Both are explained in the next two sections.

6.2.1. Nieuwe Maas dominated

This type of salt intrusion is related to the salt concentrations in the Nieuwe Maas during ebb tide. The salt concentration in the Nieuwe Maas remains raised during ebb tide compared to the background concentration. So, when the inflow into the Hollandsche IJssel starts with the flood tide, immediately saltier water enters and thus higher salt concentrations are measured at Krimpen aan den IJssel.

This type of salinization of the Hollandsche IJssel results in much higher salt concentrations at Krimpen aan den IJssel, compared to Sliksloot dominated. Nieuwe Maas dominated shows salt concentrations above 1000 mg Cl/l, while Sliksloot-dominated salinization shows peaks up to 500 mg Cl/l.

6.2.2. Sliksloot dominated

The Sliksloot is a small channel connecting the Hollandsche IJssel with the Nieuwe Maas. This second connection has its junction located more upstream in the Nieuwe Maas compared to the Hollandsche IJssel's main link. The impact of this little channel on salt intrusion in the Hollandsche IJssel is explained with the schematization in figure 6.4.

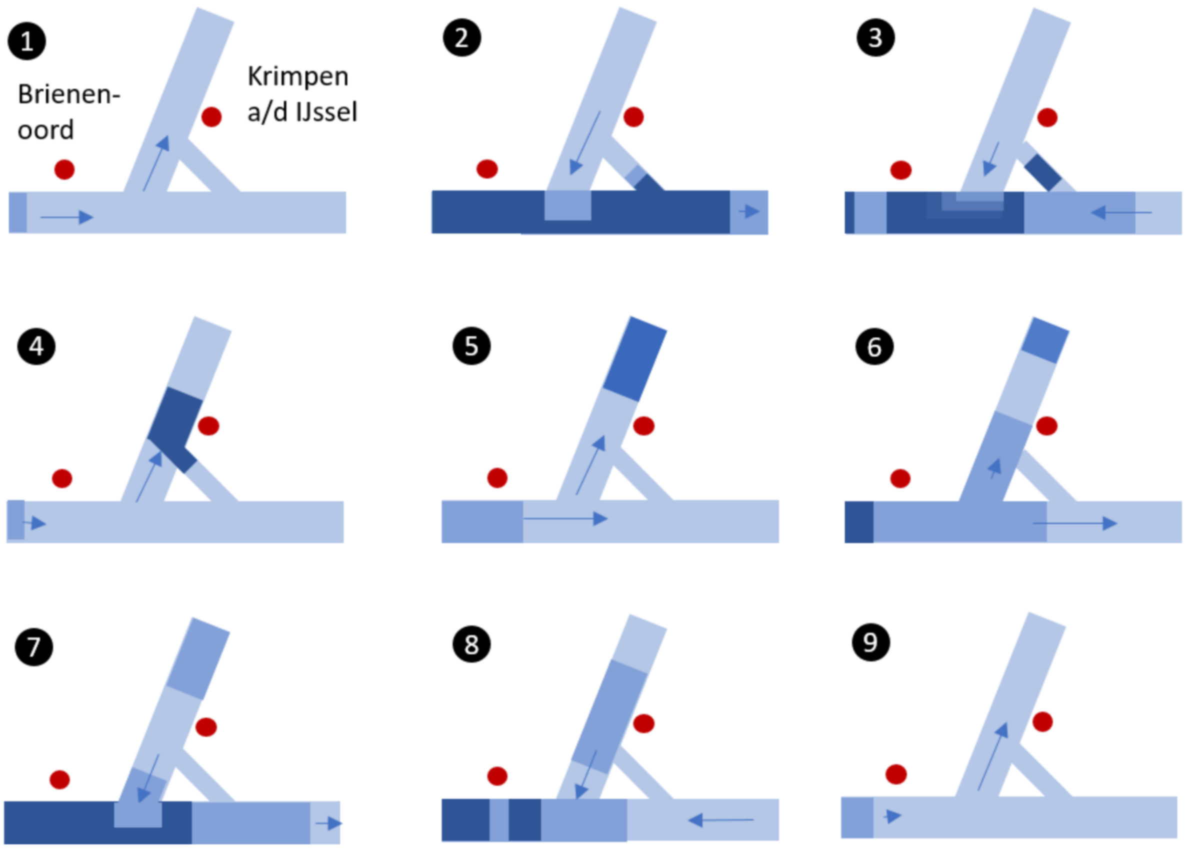

Figure 6.4: Schemetization of salt intrusion in the Hollandsche IJssel. The numbers indicate different moments during two tidal periods. The arrows indicate the flow direction, and the colour blue indicates the salt concentration (darker means saltier). Figure retrieved from Laan et al. (2021)

The flood tide carries saltier water into the Nieuwe Maas, but it has not yet reached the entrance of the Hollandsche IJssel (1). So, the water at Krimpen aan den IJssel stays fresh. The flood tide carries the saltier water further landward, and as the tide turns, it causes an outflow from the Hollansche IJssel into the Nieuwe Maas. This prevents salt from intruding into the Hollandsche IJssel. The flow in the Nieuwe Maas is however not yet reversed, so salt water travels further upstream (2). When the flow in the Nieuwe Maas also reverses, some saltier water gets transported into the Sliksloot. At the same time, the outflow of the Hollandsche causes a freshwater anomaly (3).

The second tidal inflow occurs, but now the water near Krimpen aan den IJssel shows increased salt concentrations (4). As the saltier water in the Nieuwe Maas has not yet reached the junction with the Hollandsche IJssel, the saltier water must originate from the Sliksloot, which was left behind during situation 3. As the inflow continues, the salt water bubble travels further upstream in the Hollandsche IJssel, and the water at Krimpen aan den IJssel becomes fresh again (5). The inflow duration is long enough for saltier water from the Nieuwe Maas to enter the Hollandsche IJssel (6).

When the tide becomes ebb again, the saltier water flows back into the Nieuwe Maas and reduces the salt concentrations at Krimpen aan den IJssel (7). Around halfway through the outflow, the concentration of salt at Krimpen aan den IJssel becomes higher again as the salt bubble from the Sliksloot passes again. However, due to dispersion, the salt concentration has decreased (8). Finally, the flood tide starts again (9) and results in a similar pattern as in situation 1.

The impact of the Sliksloot was further researched in the RMM3D model, as shown in appendix B. In the end, the impact of the Sliksloot was not found in the RMM3D model, while the raised ebb concentrations of the Nieuwe Maas were visible. So, this thesis will not further investigate the impact of the Sliksloot.

6.2.3. Prevention salt intrusion Hollandsche IJssel

Rijkswaterstaat and multiple water authorities developed the Klimaatbestendige Wateraanvoer (KWA, in English: climate-resilient water supply). The KWA is a program to transport fresh water to the Western Netherlands in case the freshwater supply from the Rhine is limited due to drought. With the use of the KWA, freshwater is transported to the Western Netherlands through a network of waterways, weirs and pumping stations.

The KWA can also provide freshwater to counter salinization. Measures for the Hollandsche IJssel include additional upstream water supply via the Waaiersluis and or the krimpenerwaard, see figure 6.5. Both methods require the water of the Lek to be rerouted towards the Hollandsche IJssel (Werkgroep Slim Watermanagement, Rijn-Maasmonding, 2021).

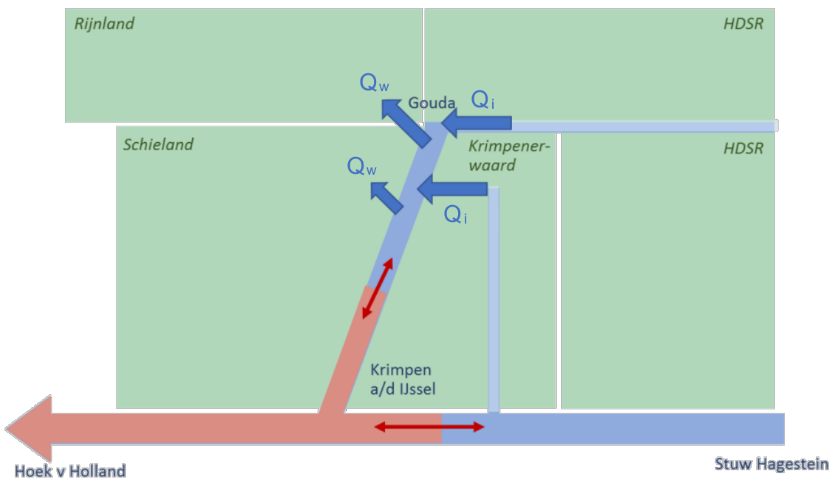

Figure 6.5: Freshwater supply Hollandsche IJssel. Q_i and Q_w show the main inflow and withdrawal locations to prevent salinization of the upstream part of the Hollandsche IJssel. Figure retrieved from Werkgroep Slim Watermanagement, Rijn-Maasmonding (2021)

How much water is needed depends on the required withdrawal in the Hollandsche IJssel and the possibly required surplus. This surplus is used to flush the upstream region clear of salt water or to prevent dispersive processes from bringing salt water upstream. With a netto discharge of 1 – 5 m^3/s, the upstream area can slowly be replaced with fresh water (Laan et al., 2021).

6.3. Conclusion

Salinization of the Hollandsche IJssel is limited due to a phase difference between the Hollandsche IJssel and the Nieuwe Maas. The discharge in the Hollandsche IJssel leads in phase compared to the Nieuwe Maas, which causes the outflow of the Hollandsche IJssel to take place towards the end of the flood in the Nieuwe Maas. At this time, the highest salt concentration occurs in the Nieuwe Maas which cannot enter the Hollandsche IJssel.

However, the phase difference cannot prevent saltier water from entering the Hollandsche IJssel when there are raised salt concentrations during ebb in the Nieuwe Maas. So, the salt concentration in the Nieuwe Maas is already high and significantly increases the salinity in the Hollandsche IJssel. The additional connection with the Sliksloot is expected to also contribute to the salinization of the Hollandsche IJssel, however, this is not the most significant cause.

7

Phase differences in the Rhine Meuse Delta

Chapter 6 shifted the focus to the Rhine Meuse Delta which remains the area of interest in this chapter. In addition, it stated that the phase difference limits the salt intrusion in the Hollandsche IJssel. In this chapter, the phase difference in the Rhine Meuse Delta is determined, based on the results from a numerical model of the RMD (RMM3D). These results are compared to the single junction analytical model, as used in chapter 5. So, we can determine if this model suffices or if a more detailed model of the RMD is needed to research further optimization of the phase difference. First, in section 7.1 the phase difference at the Hollandsche IJssel is determined. Next, the main tidal constituent regarding tidal trapping is established in section 7.2. Finally, in section 7.3 the results from this chapter are compared to the phase difference found in the single junction network of chapter 5.

7.1. Tidal phase difference

To investigate how tidal phase differences influence salt intrusion in the multi-branch Rhine Meuse Delta, the results from a detailed numerical model are used (RMM3D). This model is validated based on low discharge situations from 2011 and 2018 (Van der Kaaij and Chavarrias, 2020; Van der Kaaij et al., 2022). The RMM3D model also includes detailed bathymetry. The boundary conditions are derived from the Noordzeemodel 3D at the seaside (Zijl and Veenstra, 2018; Zijl et al., 2021) and measurement data from DONAR at the riversides (Laan et al., 2023).

The validation run of the RMM3D model, based on data from 2018 is used to study the phase difference in velocities at the junction between the Hollandsche IJssel and the Nieuwe Maas. According to Van der Kaaij et al. (2022), the RMM3D model reproduces the discharge measurements at multiple junctions very well. Furthermore, it reproduces the salinization measurements in the main channels correctly. Two important considerations with the RMM3D model for this study are the lack of model quality of the salinization in the upstream part of the Hollandsche IJssel and the underestimation of the salt concentrations at Krimpen aan den IJssel, with around 1 PSU. However, this research focuses on the processes at the entrance of the Hollandsche IJssel and the pattern of the salinity, so these considerations do not affect this analysis.

Two cross-sections are used to determine the phase difference. These are located in the Nieuwe Maas at the Brienenoord and in the Hollandsche IJssel at Stormpolder, the locations are visible in figure 7.1.

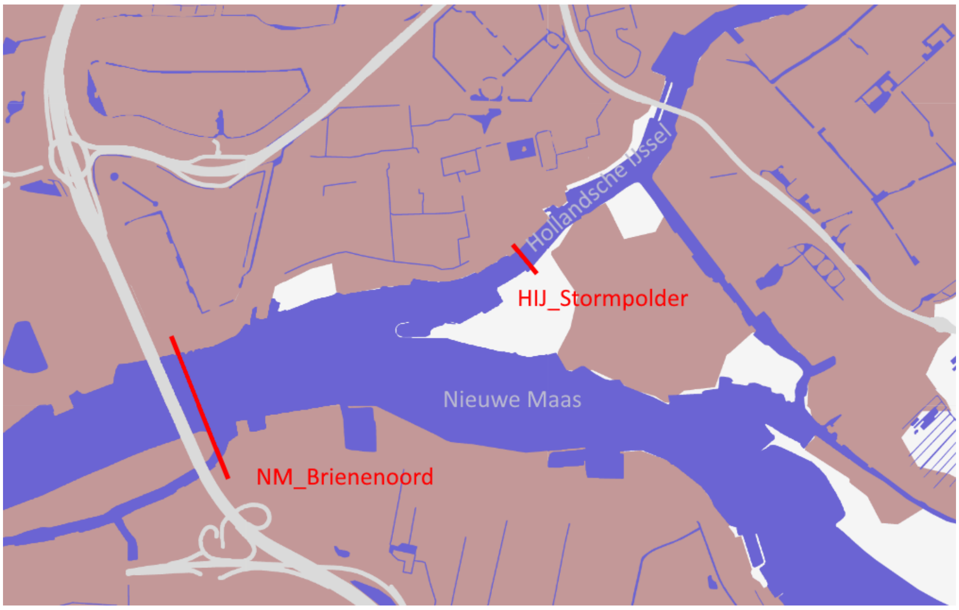

Figure 7.1: Overview of cross-section locations near junction Nieuwe Maas and Hollandsche IJssel given in red.

The phase difference at a junction is resolved in two manners. The first method is based on the time difference between the zero crossings in the Nieuwe Maas and the Hollandsche IJssel. The zero crossings indicate when the flow reverses in the channels. The time between these moments of flow reversal in the Hollandsche IJssel and the Nieuwe Maas is an indication of the phase difference.

The second method consists of a tidal analysis of the discharge signal at both locations. The tidal analysis is done across a moving window of eight tidal cycles for the constituent set of a day. The tidal analysis gives for each constituent the amplitude and the phase. The difference between the phase of a single constituent at two locations gives a tidal phase difference. This tidal phase difference is directly related to the forcing of the system and this is the variable which is investigated.

The amplitude of each constituent determines if the constituent is significant. The significant constituents can be restored into a single velocity signal. This single velocity signal is created with the formula in equation 7.1. This allows a reproduced signal to be compared to the original and determine if the representation is adequate.

$$v(t) = A_0 + \sum_{n=1}^{N} A_n \cdot \sin(\omega_n t - \phi_n) \tag{7.1}$$

Where A_0 is the offset, n is the constituent, N is the total number of constituents, A_n is the amplitude of constituent n, ω_n is the angular velocity of constituent n, t is the time and θ_n is the phase of constituent n.

The results of the tidal analysis are presented as constituents with the notation Di instead of the better-known Mi. The distinction is made as the Di is not a real tidal constituent, but a moving average of the Mi constituent.

7.1.1. Phase difference Hollandsche IJssel

The discharge through the cross-section is taken from the previously mentioned locations near the junction of the Hollandsche IJssel. These discharges are converted to a cross-sectionally averaged velocity by dividing it by its cross-sectional area. The tidal analysis is applied to these cross-sectionally averaged velocity signals. The amplitudes in figure 7.2 show the most significant components from the tidal analysis.

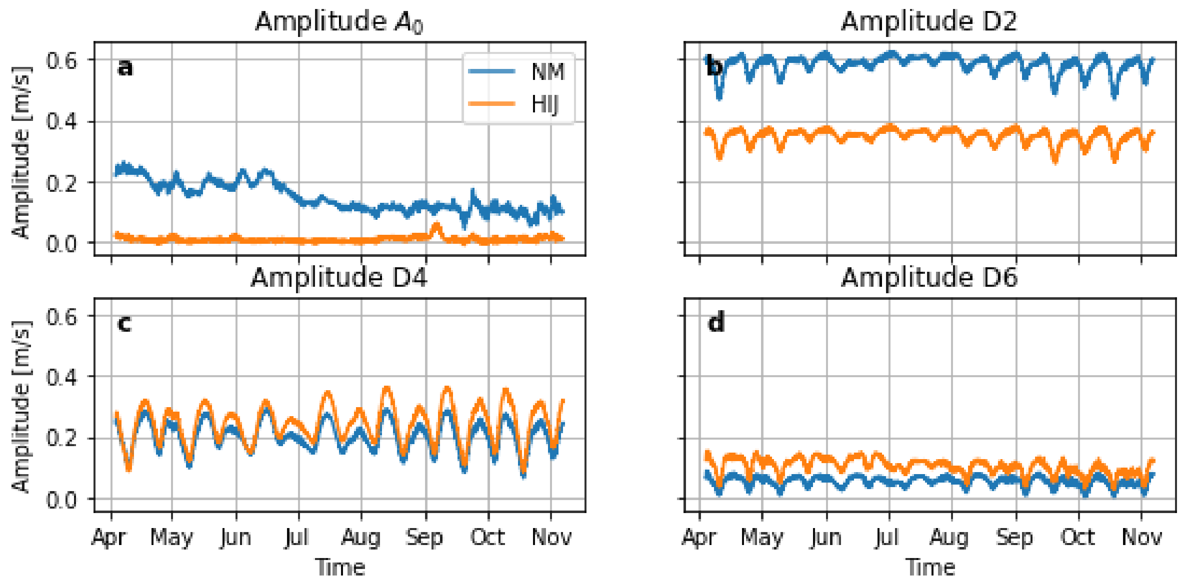

Figure 7.2: Amplitudes of the most significant constituents at Brienenoord in the Nieuwe Maas (NM) and the entrance of the Hollandsche IJssel (HIJ). **(a)** The offset of the velocity signal, due to river discharge and set-up. **(b)** The amplitude of D2. **(c)** The amplitude of D4. **(d)** The amplitude of D6

The constituents D2, D4, D6 and the offset A_0 are combined into a new velocity signal, using equation 7.1. Comparing this to the original velocity signal shows a good reproduction of the signal, see figure 7.3. The reproduced signal only struggles with reproducing the extreme values. In the end, these three constituents are used for determining the phase differences.

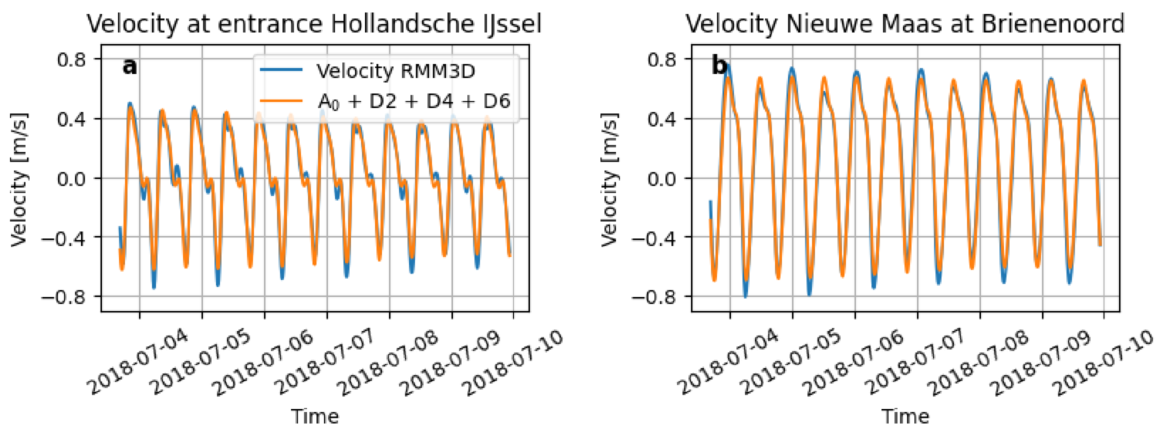

Figure 7.3: Original cross-sectionally averaged velocity compared to the reproduced signal with constituents A_0, D2, D4 and D6. **(a)** Velocity at the mouth of the Hollandsche IJssel **(b)** Velocity at Brienenoord in the Nieuwe Maas

The tidal phase differences for each component are compared to the time difference between flow reversals of the original velocity signal. However, determining the moments of flow reversal in the Hollandsche IJssel is more complex. The velocity shows a second peak during a tidal cycle and this second peak does not always cross the zero line, see figure 7.3. However, if the second peak does not cross the zero line, the most significant part of the outflow is not yet started at the zero crossing and thus the second peak is chosen as the moment of flow reversal. For the remaining cases, the zero crossing after the second peak is chosen.

Figure 7.4 shows that the tidal phase difference of a single constituent does not fully represent the time difference between the moments of flow reversal at the Hollandsche IJssel and the Nieuwe Maas, which was found to be around 75 minutes. However, the time difference between flow reversals of the reproduced signal is adequate. Along with the knowledge that these three constituents are the most significant based on their amplitude, this research can be limited to the constituents A_0, D2, D4 and D6.

The discrepancy between the original and replicated time differences can be attributed to the occurrence of a second peak during a tidal period at the Hollandsche IJssel. As the extremes are not as accurately reproduced, the second peak may not always cross the zero line at the same moment as the original velocity signal. This changes the determined moment of flow reversal and thus the time differences.

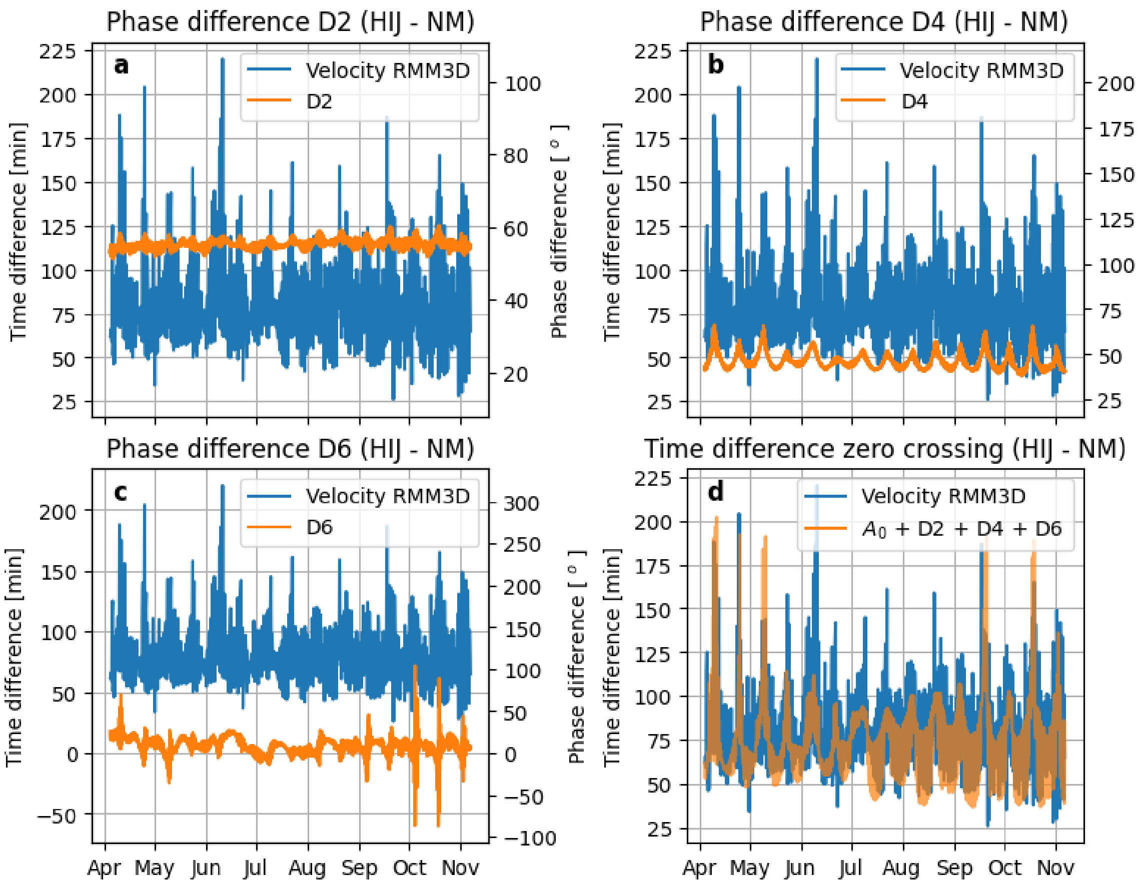

Figure 7.4: Comparison between the tidal phase differences and the time differences derived from the zero crossings of the original velocity signal. **(a)** Phase differences for D2. **(b)** Phase differences for D4. **(c)** Phase differences for D6. **(d)** Time difference determined by zero crossings for original velocity signal and reproduced velocity signal

7.2. Determination significant constituents

The impact of the phase difference on salt intrusion can be estimated with the dispersion coefficient from MacVean and Stacey (2011) and is repeated in equation 7.2. It shows the dependency on the hydrodynamics with three variables: the velocity amplitude in the main channel, the tidal radian frequency and the phase difference. To determine the most significant constituent the ratio velocity amplitude squared to tidal radian frequency is compared for D2, D4 and D6.

$$K_{trap,A} = \frac{\epsilon \hat{U}_m^2}{\omega} \left[\sin\alpha \cos\alpha \left(\frac{3\cos\alpha + 32\sin\alpha}{12\pi} \right) \right] \tag{7.2}$$

The velocity amplitudes are characterized by the most frequently occurring velocity amplitudes. The histograms are given in figure 7.5 and show a velocity amplitude of 0.60 m/s for D2, 0.23 m/s for D4 and 0.051 m/s for D6.

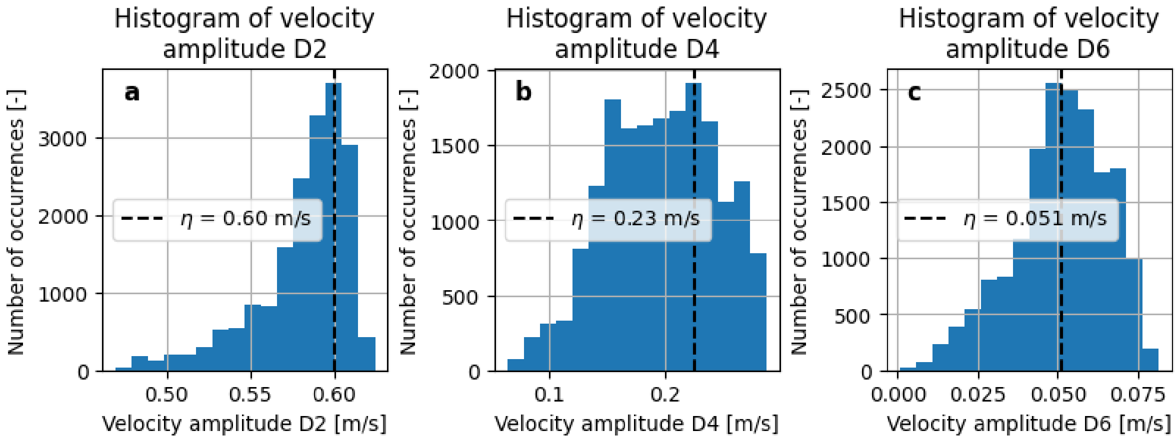

Figure 7.5: Histograms of velocity amplitude in the Nieuwe Maas at Brienenoord. **(a)** Histogram of velocity amplitude D2. **(b)** Histogram of velocity amplitude D4. **(c)** Histogram of velocity amplitude D6

The resulting ratios of velocity amplitude squared to tidal radian frequency are shown in table 7.1 and show the most significant constituent is M2. Thus, it is acceptable for this research to focus on the impact of geometry on the M2 phase difference.

Constituent	Velocity amplitude [m/s]	Tidal period [s]	ratio $\frac{U^2}{\omega}$ [m^2/s]
M2	0.60	44700	2561.12
M4	0.23	22350	188.17
M6	0.051	14900	6.17

Table 7.1: Comparison significance tidal constituent on dispersion coefficient by MacVean and Stacey (2011)

7.3. Comparison to results single junction network

The previous section showed the most significant tidal constituent for tidal trapping is M2. Chapter 5 investigated the impact of the geometry on the phase difference driven by the M2 tide. Thus the single junction analytical model results are about the most significant tidal constituent. However, the phase difference found in this simple model does not come close to the phase differences found in the RMM3D model. The phase difference found in the RMM3D model for the M2 constituent is 55°, while in the single junction network, it is 84°. Thus, in the following chapter, an analytical model is created which closer represents the RMD.

7.4. Conclusion

A tidal analysis with a moving window of eight tidal cycles is used to determine the phase and amplitude of the main tidal constituents M2, M4 and M6. However, as they are determined in a moving window, they are notated as D2, D4 and D6. Additionally, this shows the variations in the amplitude and phase across time. These three constituents combined can represent the time difference between the zero crossings of the Hollandsche IJssel and the Nieuwe Maas adequately. This time difference describes the variation between moments of flow reversal in the Hollandsche IJssel and Nieuwe Maas. The phase of one tidal constituent cannot single-handedly represent this time difference. However, a main tidal constituent regarding tidal trapping is determined with the dispersion coefficient of MacVean and Stacey (2011), which shows that the main tidal constituent is M2.

The found phase difference of 55° in the RMM3D model does not match with the results of the single junction analytical model, which resulted in a phase difference of 84°. Thus, a more detailed network representing the RMD is needed for further use of the analytical model in the Rhine Meuse Delta.

8

Analytical model of the Rhine Meuse Delta

Chapter 7 showed that the phase difference of the analytical model does not match with the results from the RMM3D model. This chapter enhances the analytical model with a more detailed network to better represent the Rhine Meuse Delta. The configuration of the model is stated in section 8.1, followed by a validation of the model in section 8.2. Next in section 8.3, all variations are again investigated in the RMD version of the analytical model and compared to the single junction network from chapter 5. Finally in section 8.4, the connection is made between the analytical model of the RMD and the RMM3D model, which compares known variations in the system.

8.1. Configuration analytical model RMD

A new configuration is created to represent the Rhine Meuse Delta more closely. The lengths and depths of each channel section are retrieved from the RMM3D model. The widths and friction coefficients are retrieved from the SOBEK model of the Rhine Meuse Delta. Figure 8.1 gives an overview of the nodes and sections. The properties of each node and section can be found in appendix C and the boundary conditions are given in table 8.1. The black nodes in the current configuration can serve one of the following purposes. An additional node is added to allow for a geometric change in a long channel, or a node is added to get a realistic channel length and lastly, additional nodes are added as currently the code cannot handle multiple junctions after each other.

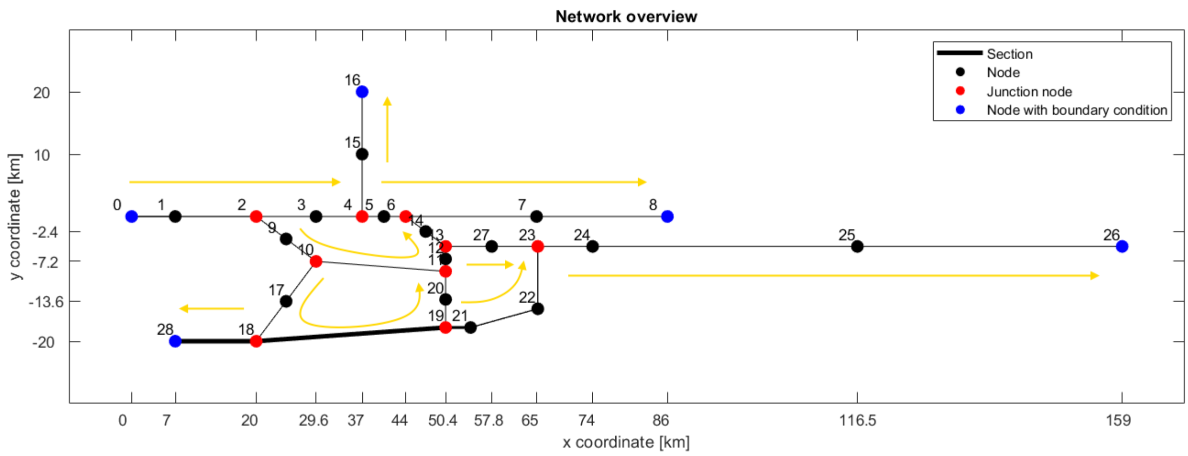

Figure 8.1: Network overview analytical model RMD. The yellow arrows indicate the positive direction

Boundary condition M2	Value	Unit
$\hat{\eta}_0$	0.87	m
$\hat{Q}_8$	0	m^3/s
$\hat{Q}_{16}$	0	m^3/s
$\hat{Q}_{26}$	0	m^3/s
$\hat{Q}_{28}$	0	m^3/s

Boundary condition Q_f	Value	Unit
$\hat{\eta}_0$	0	m
$\hat{Q}_8$	0	m^3/s
$\hat{Q}_{16}$	0	m^3/s
$\hat{Q}_{26}$	-734	m^3/s
$\hat{Q}_{28}$	0	m^3/s

Table 8.1: Boundary conditions the analytical model of RMD network. The left table shows boundary conditions for the M2 tide and the right table the river discharge

8.2. Validation analytical model RMD

The analytical model is validated for the water level amplitudes and discharges. The water levels in the analytical model cannot be compared directly to the water levels in the RMM3D model. This is partly due to the analytical model only using a single constituent as water level forcing. Furthermore, the analytical model does not take bed slopes into account. Thus, this increases the water level upstream with respect to the reference level is not taken into account. However, it is possible to compare the amplitudes at the end of the Hollandsche IJssel and Lek with the RMM3D model.

This requires representative values for the forcing at the two boundaries. These are determined by the most occurring value across the drought period, which starts around the beginning of July 2018. Discharge and water level histograms are given in figure 8.2. The peak in the histogram is chosen as the representative value and is based on the mean of one or two bins.

The amount of bins is determined with Sturge's rule (Scott, 2011). This computes the number of bins from the number of data points, the formula is shown in equation 8.1. The boundary conditions for the analytical model become, according to figure 8.2, a discharge of 734 m^3/s at the Waal and a tidal amplitude of 0.87 m for the M2 tide.

$$n_{\text{bins}} = 1 + \lceil \log_2 (n_{\text{data}}) \rceil = 1 + \lceil \log_2 (18169) \rceil = 16 \tag{8.1}$$

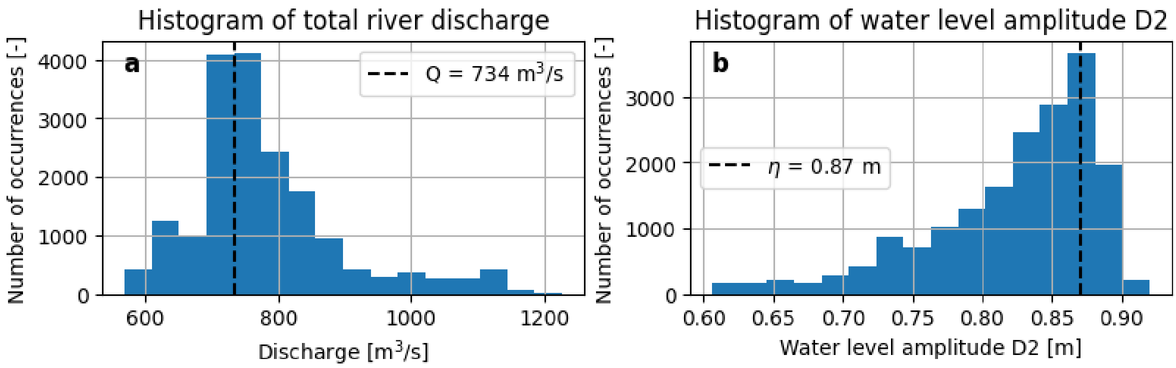

Figure 8.2: Histograms of discharge and water level. **(a)** Histogram of total river discharge in RMD (Waal, Lek and Meuse). **(b)** Histogram of water level amplitude D2.

The comparison between the analytical model and the data analysis of the RMM3D model is done for two locations, the end of the Hollandsche IJssel and the end of the Lek. The comparison in water level amplitudes for a given tidal amplitude is shown in table 8.2. The method of determining the water level amplitudes from the RMM3D results is shown in appendix D. The water level amplitudes of the M2 tide in the analytical model match the RMM3D results well.

Location	Tidal component and amplitude [m]		Water level amplitude RMM3D [m]	Water level amplitude analytical model [m]
End of the Hollandsche IJssel	M2	0.87	0.720	0.757
End of the Lek	M2	0.87	0.680	0.643

Table 8.2: Comparison of the water level amplitudes between the RMM3D results and the analytical model of the RMD for multiple constituents at the end of the Hollandsche IJssel and the Lek

This scenario is further verified with the discharge distribution derived from SOBEK with low river discharges, see figure 6.1. The results of the analytical model can be seen in figure 8.3. The results of SOBEK are in combination with normal tidal conditions, so the analytical model is also run in combination with a 0.87 m M2 tide. The discharges match the results of SOBEK well, except for the south side of the Rhine Meuse Delta. This difference is ascribed to missing boundary conditions: the Meuse discharge and the sinks at the Haringvliet Sluices and the Volkerak. These boundary conditions withdraw water from the south, which lowers the water level. This is compensated by an increased discharge to the south side and lowers the discharges in the north of the RMD. This would align with the results from SOBEK as the discharge in the north of the RMD is slightly too large.

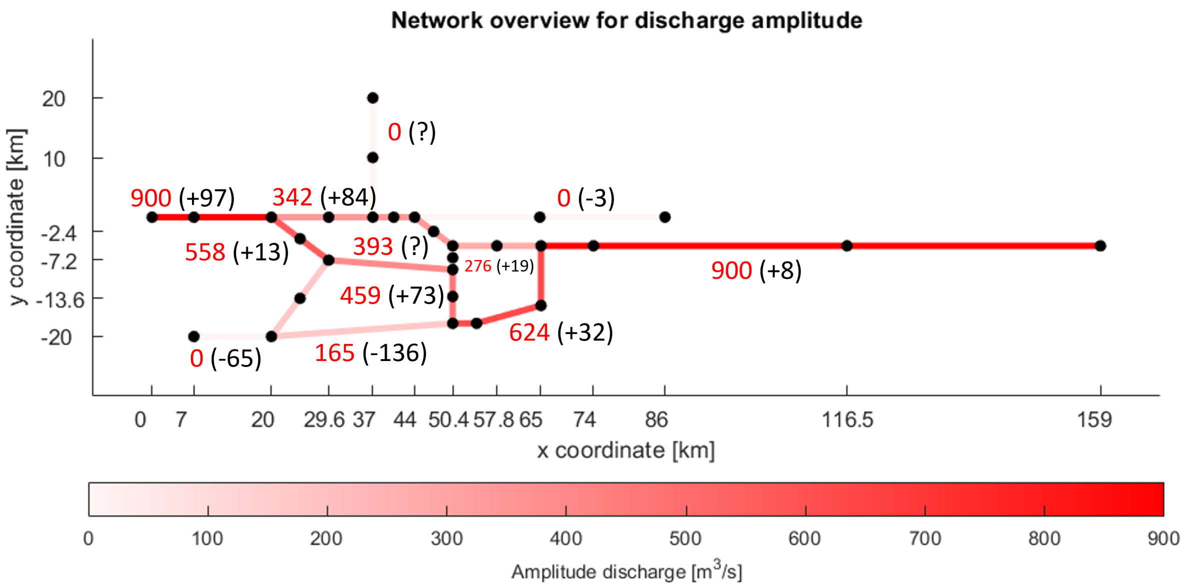

Figure 8.3: River discharge distribution in the analytical model. Red values show results from the analytical model and black values show the difference between the analytical model and the SOBEK results

8.3. Comparison analytical model SJN and RMD

Changes in the geometry of the side channel and the forcing are also investigated in the analytical model of the RMD and compared to the results of the single junction network. Most important the overall shape of the graphs did not change, see appendix E. Thus, the processes responsible for the change in the phase differences can be explained with the SJN analytical model. Additionally, a more accurate prediction of the change in phase difference can be made with a more detailed configuration.

Most variations to the geometry are done across multiple channel sections with changing geometries. However, the absolute difference between channel sections does not change across all variations. A special case is the length of the channel, where the change in cross-section remains at the same currently defined channel length. So, for shorter channel lengths no change in cross-section occurs.

The RMD scenario mainly showed that the current configuration of the Hollandsche IJssel is challenging to improve. All initial values are located in parts of the curves which require a great change to the geometry for a small change in the phase difference, see appendix E. This can be explained by the phase difference between the water level and the discharge of the Hollandsche IJssel, which is already close to 90°. So, to get a significant increase in the phase difference, a large change in the geometry is needed.

In addition to the Hollandsche IJssel, the impact of the geometric variables is also investigated for the Lek. These results are shown in appendix F. Most results showed similar patterns for the phase difference. These results also show that the current geometry of the Lek requires smaller changes to the geometry for significant changes to the phase difference. This is because the phase difference between the water level and discharge in the Lek is not close to 90°.

8.4. Comparison analytical model RMD and RMM3D

The results of the analytical model are compared to the results of the RMM3D model. The impact on the phase difference due to the length of the side channel can be compared to two side channels in the Rhine Meuse Delta, namely the Hollandsche IJssel and the Lek. Furthermore, the impact of the spring neap cycle can be compared to a change in amplitude at the boundary of the analytical model. Laan et al. (2023) showed in their report the impact of a change in depth for two scenarios. Firstly, a uniform lowering of 1 m in the Nieuwe Waterweg and the Nieuwe Maas. Secondly, a uniform lowering of 1 m in the Lek.

8.4.1. Length of side channel

The length of two semi-closed side channels, the Hollandsche IJssel and the Lek are used to compare the analytical model results. The Hollandsche IJssel is a short side channel of 20 km and the Lek is around double the length at 42 km.

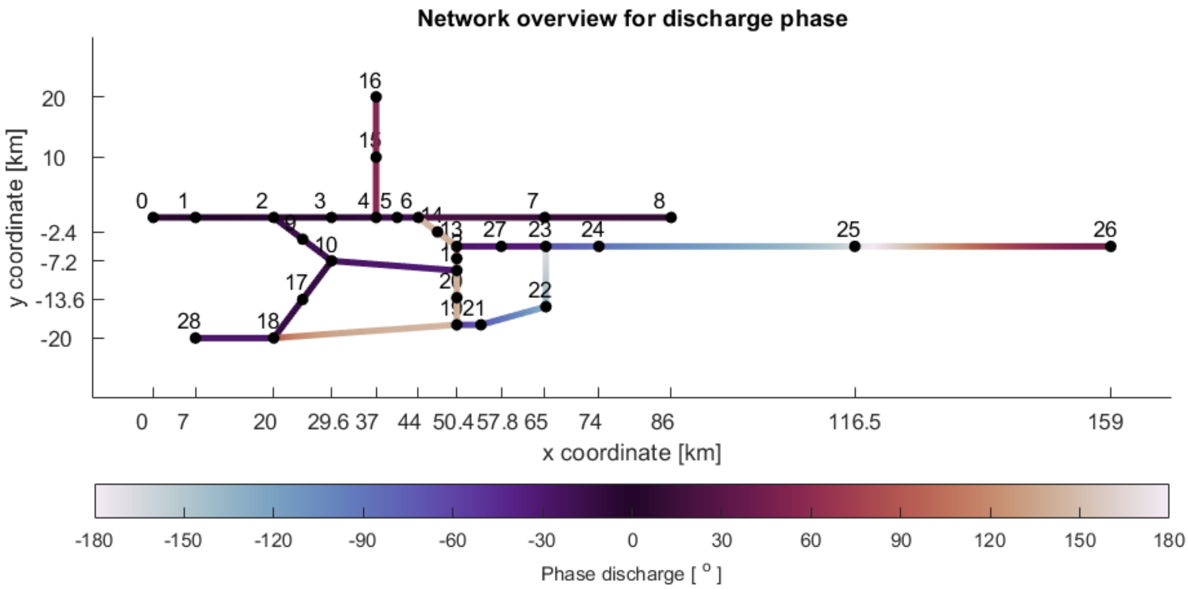

Figure 8.4: Phases discharge in RMD network

The resulting phase differences for the Hollandsche IJssel and the Lek are given in the equation below.

$$\begin{aligned} \theta_{HIJ} &= \phi_{Q_{4c}} - \phi_{Q_{4a}} = 56.82 - -8.39 = 65.21^\circ \\ \theta_{LEK} &= \phi_{Q_{6b}} - \phi_{Q_{6a}} = 23.15 - -18.91 = 42.06^\circ \end{aligned} \tag{8.2}$$

These results are compared to the data analysis from the RMM3D model. For each junction, two locations are chosen and subjected to a tidal analysis with a moving window of eight tidal cycles. This gives, for each location, the amplitude and phase of the D2 constituent, which can be compared to the analytical model.

The phase difference plotted against the amplitude of the D2 tide by Hoek van Holland shows some spread in the results. So, a linear fit through the data is made to get to a single value. Given the amplitude of 0.87 m, the phase difference at the Hollandsche IJssel is 55.34° and at the Lek 31.33°.

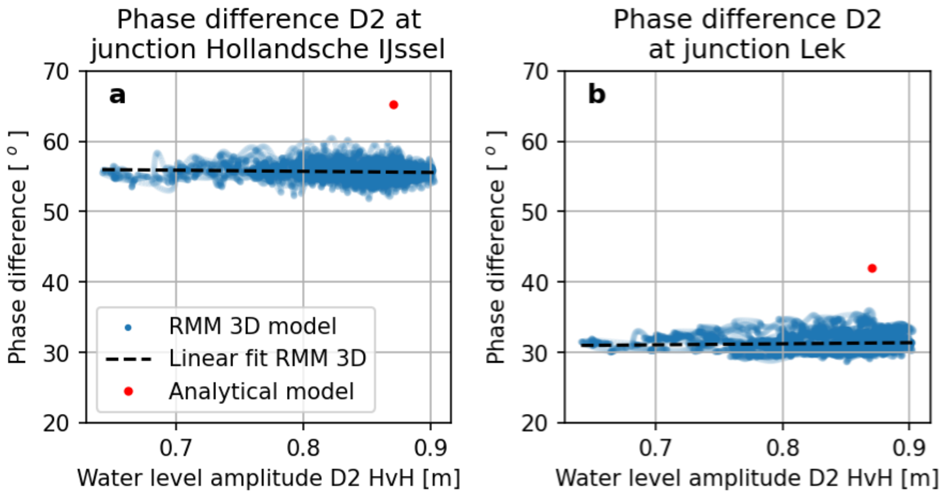

Figure 8.5: Phase differences in RMM3D model in combination with the amplitude of D2 at Hoek van Holland. **(a)** Phase difference at the Hollandsche IJssel **(b)** Phase difference at the Lek

8.4.2. Depth of the main channel in front of the junction

Laan et al. (2023) researched the effect of a bed level lowering in the Nieuwe Maas and Nieuwe Waterweg. The bed level lowering was uniformly applied to the section between the connection of the Maasgeul at Hoek van Holland and the Erasmusbrug. The Erasmusbrug is located around 6 km in front of the junction with the Hollandsche IJssel. In the analytical model, this corresponds to the sections between nodes 0 and 3. For each section, the depth was lowered by 1 m.

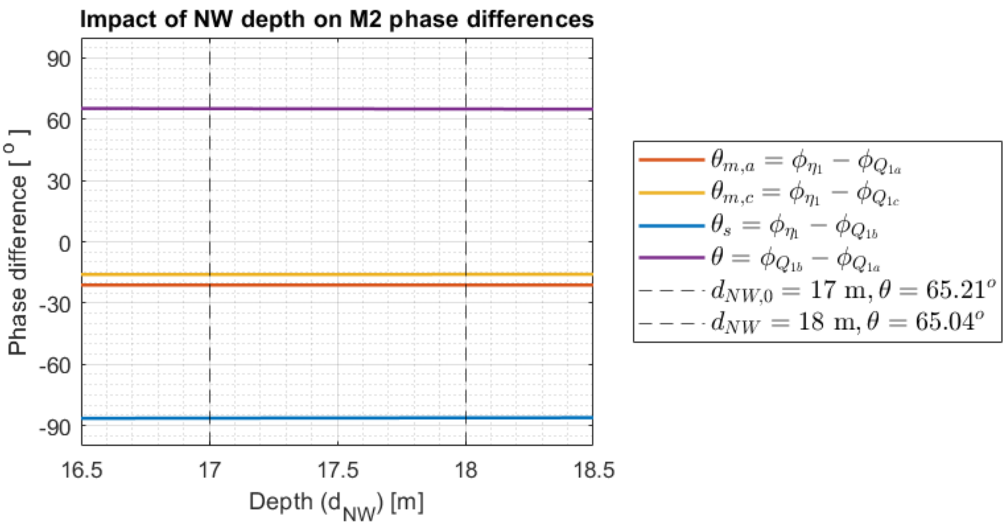

Figure 8.6: Impact uniformly lowering bed level by 1 m in the Nieuwe Waterweg and Nieuwe Maas

As can be seen in figure 8.6, the impact of the bed level lowering is very limited at these larger water depths. The change in phase difference is a decrease of 0.17°. For a M2-tide this results in a change in phase difference of 0.35 minutes. This is in line with the results from Laan et al. (2023), where they found a decrease in phase difference of less than a minute in general.

8.4.3. Depth of Lek

Laan et al. (2023) also researched the impact of a bed level lowering in the Lek on the phase difference at the Hollandsche IJssel. The bed level lowering was uniformly applied across the entire Lek till Hagestein. In the analytical model, this corresponds to the sections between nodes 6 and 8.

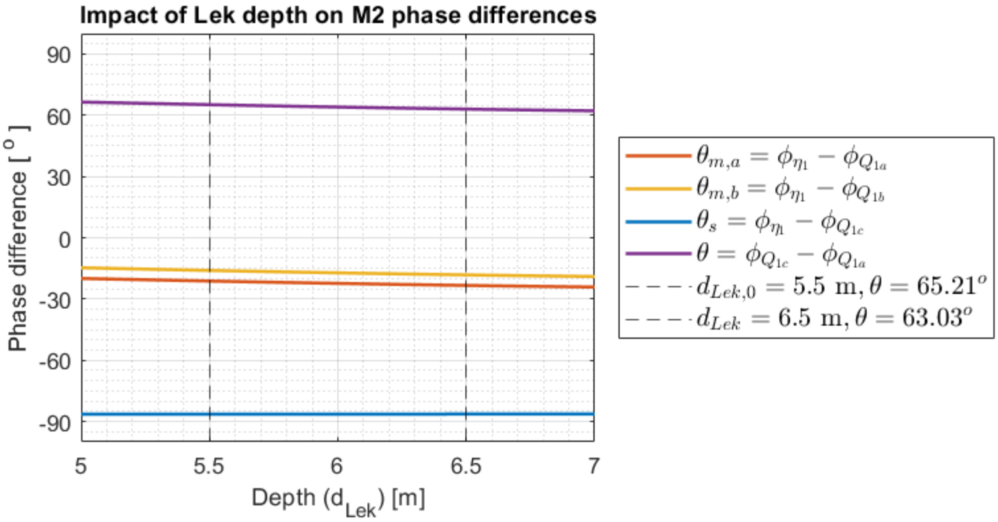

Figure 8.7: Impact uniformly lowering bed level by 1 m in the Lek

Figure 8.7 shows a more significant change in phase difference. The decrease in phase difference is 2.18° or 4.51 minutes for the M2-tide. This is lower, compared to Laan et al. (2023) which found a decrease of roughly 10 minutes, but still the same order of magnitude.

8.4.4. Spring and neap tide

Laan et al. (2023) already showed the impact of spring and neap tide, where the phase difference increases by around 5 minutes during neap tide compared to the spring tide. The representation of spring and neap tide in the analytical model is limited. Only a change to the amplitude can be made. The amplitude of the M2 tide in the RMM3D model varies between 0.6 and 0.9 m. As can be seen in figure 8.8, when the amplitude changes from 0.6 to 0.9 m, the phase differences decrease by 2.71° or 5.61 minutes. Thus, this variation is also in the same order of magnitude.

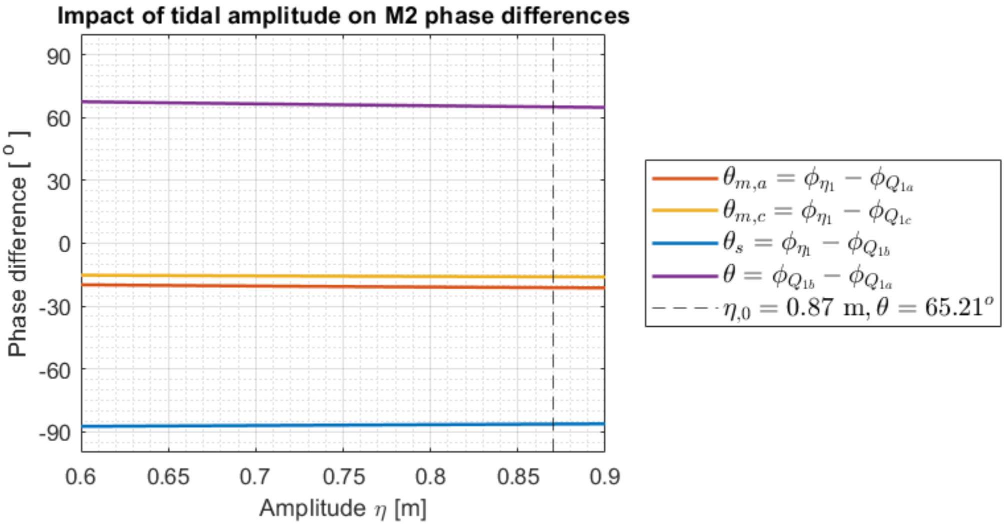

Figure 8.8: Impact water level amplitude tide on phase difference

8.5. Conclusion

The Rhine Meuse Delta is modelled in the analytical model to represent the phase difference at the Hollandsche IJssel. The model is validated for water levels at two locations, the end of the Hollandsche IJssel and the end of the Lek. In addition, the river discharges are validated against a SOBEK simulation. This showed that the analytical model of the RMD can adequately represent the main tidal constituent.

The variations in geometry and forcing in the analytical model of the RMD resulted in the same patterns for the phase difference as were found in chapter 5. Additionally, these results showed that the current geometry of the Hollandsche IJssel is hard to further improve regarding the phase difference, as the current phase difference between the water level and discharge of the Hollandsche IJssel is close to 90°. The current geometry of the Lek was found to have a phase difference between the water level and discharge which is further removed from 90°, meaning significant changes to the phase difference can be obtained with limited geometric adaptations.

The phase difference in the analytical model of the RMD has a value of 65° at the Hollandsche IJssel and 42° at the Lek. Given the simplifications made, the analytical model matches the RMM3D adequately, where the phase differences are 55° at the Hollandsche IJssel and 31° at the Lek. Variations in the depth and spring neap cycle are compared between the RMM3D model and the analytical model of the RMD. The results show that the analytical model can represent the order of magnitude and the sign of the change in phase difference well.

9

Analysis of minimization salt intrusion

Chapter 8 demonstrated that the analytical model of the Rhine Meuse Delta is capable of predicting the order of magnitude and the sign of the change in phase difference for a given change in geometry. In addition, chapter 8 showed the limited possibilities to further alter the Hollandsche IJssel and the possibilities at the junction with the Lek. In this chapter, the analytical model of the RMD is further used to modify the phase difference to minimize salt intrusion in the Hollandsche IJssel and the Lek.

9.1. Alterations phase differences

The optimal phase difference between the main and side channels is hard to determine. The most optimal time to start inflow in the side channel is when the salinity in the main channel has dropped back to background levels. This would extend the period during which freshwater flows into the Hollandsche IJssel and further limit the flow of saltwater into the Hollandsche IJssel. Thus, it is expected that a larger phase difference is required to minimize salt intrusion in the side channel.

The previous chapter mentioned that the phase difference at the Hollandsche IJssel is hard to adjust significantly, given the current configuration. So, to increase the phase difference by 5° or 10 minutes, only one variable can be modified. This is the length of the Hollandsche IJssel, and halving its length would increase the phase difference by 5.29° or 10.94 minutes, see figure 9.1.

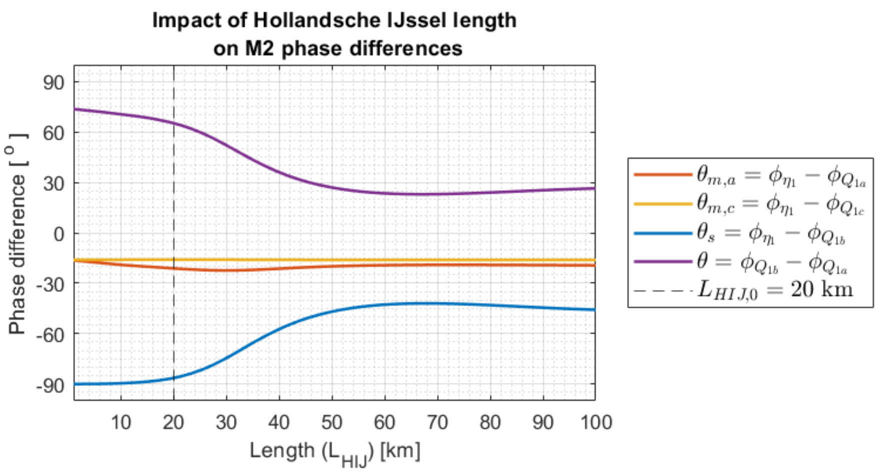

Figure 9.1: Impact length on phase difference at the Hollandsche IJssel in analytical model RMD

It was found that the phase difference at the Lek is easier to improve by modifying the geometry. This is the most visible in the channel length and depth, as the current geometry is located in the region where a small change in the geometry alters the phase difference significantly, see figure 9.2. The required changes in geometry for an increase in phase difference of 10 and 20 minutes are shown in table 9.1.

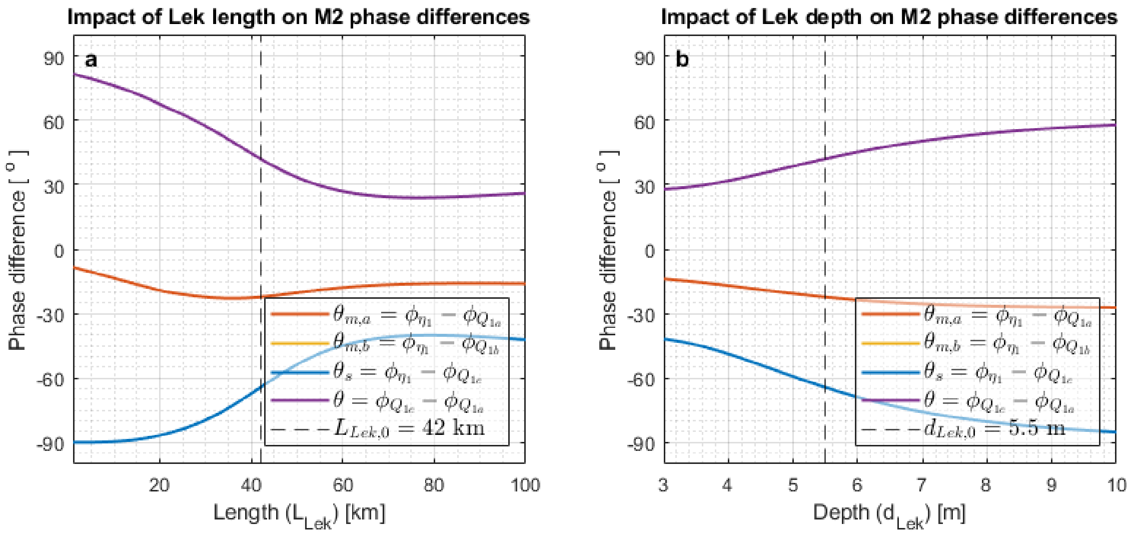

Figure 9.2: Impact geometric variables on phase difference at the Hollandsche IJssel in analytical model RMD. **(a)** Impact of the length of the Lek **(b)** Impact of the depth of the Lek

Variable	**Value**	**Unit**	**△ value**	**Unit**	**△ phase difference**	
					[°]	**[min]**
Length	42	km	0	km	0	0
	38	km	-4	km	+5.12	+10.60
	34	km	-8	km	+10.32	+21.36
Depth	5.5	m	0	m	0	0
	6.35	m	+0.85	m	+5.13	+10.62
	7.45	m	+1.95	m	+10.02	+20.74

Table 9.1: Required changes to length and depth for an increase in phase difference of 10 and 20 minutes

An increase in the depth of the Lek has been investigated before by Laan et al. (2023). They showed that a uniform increase in the depth of the Lek by 1 m results in a slight increase in salinization downstream of the Lek. Additionally, it substantially increases the salinization of the Lek itself. Both are caused by an increase in tidal intrusion. However, the impact downstream is smaller as the Lek mainly forms a connection to the upstream rivers and it has a limited impact on the downstream system (Laan et al., 2023).

9.2. Impact on salt flux in Hollandsche IJssel

Currently, the inflow of the Hollandsche IJssel starts approximately in the middle of two salinity peaks in the Nieuwe Maas, see figure 9.3. A small part of the peak in salinity in the Nieuwe Maas still enters the Hollandsche IJssel. However as this is at the end of the inflow period, the higher concentrations remain near the mouth of the Hollandsche IJssel. The figure further shows that an increase in phase difference should result in an earlier inflow moment for the Hollandsche IJssel and thus it should lower the salt concentration in the Hollandsche IJssel.

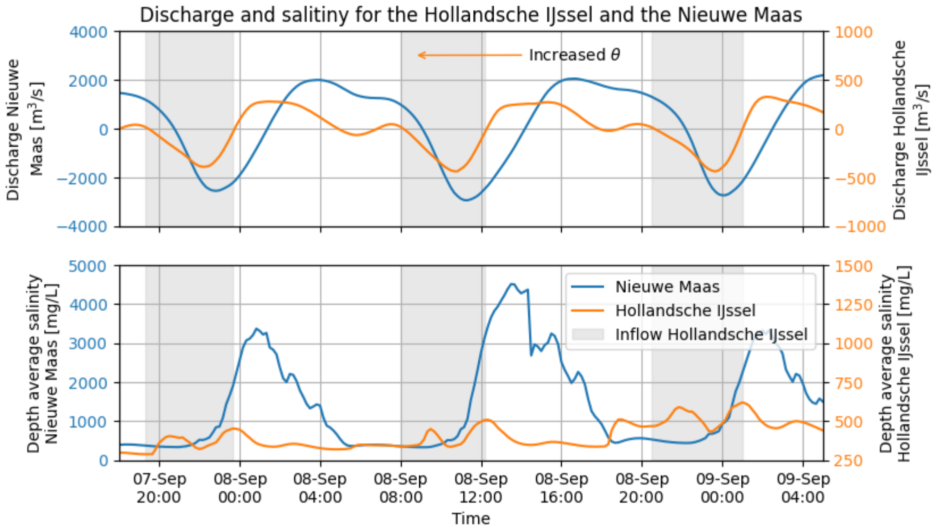

Figure 9.3: Moments of inflow for the Hollandsche IJssel compared to salinity in Nieuwe Maas. The arrow indicates the direction of the shift for the discharge signal of the Hollandsche IJssel for an increased phase difference. Results are retrieved from the RMM3D model

To quantify the impact of an increased phase difference, a first estimate of the impact on the salt flux entering the Hollandsche IJssel is made. The salt flux is defined as the salinity in the Nieuwe Maas times the discharge entering the Hollandsche IJssel, thus $F_s = S_{NM} \cdot Q_{HIJ}$. This first estimate assumes that the change in geometry only causes a shift in the discharge signal of the Hollandsche IJssel. Figure 9.4 shows that an increase of the phase difference by 10 minutes results in a decrease of the inward salt flux of up to 25% on average.

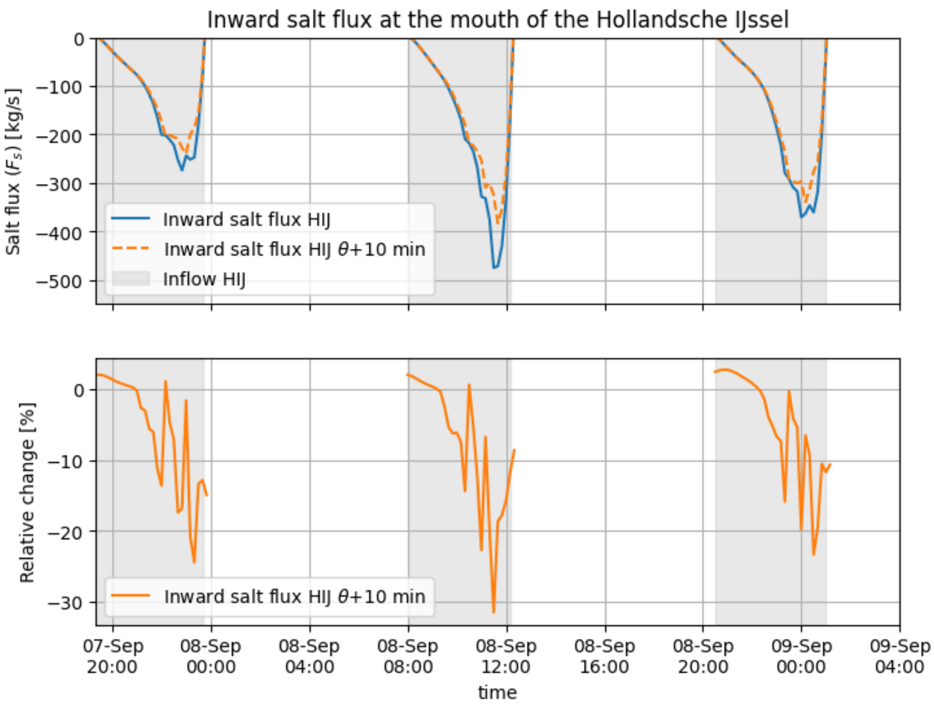

Figure 9.4: Inward salt flux at the Hollandsche IJssel for the current situation and an increased phase difference of 10 minutes

The impact of the change in phase difference on the Nieuwe Maas is estimated with the dispersion coefficient of MacVean and Stacey (2011). For this first estimate, it is assumed only the phase difference is impacted. So, only the term f_θ is of importance, as stated in equation 9.1. The result of a 10-minute shift in the phase difference is shown in figure 9.5, and it results in a decrease in the dispersion coefficient of 4%.

$$K_{trap,A} = \frac{\epsilon \hat{U}_m^2}{\omega} \cdot f_\theta \quad \text{with} \quad f_\theta = \sin\alpha\cos\alpha\left(\frac{3\cos\alpha + 32\sin\alpha}{12\pi}\right) \tag{9.1}$$

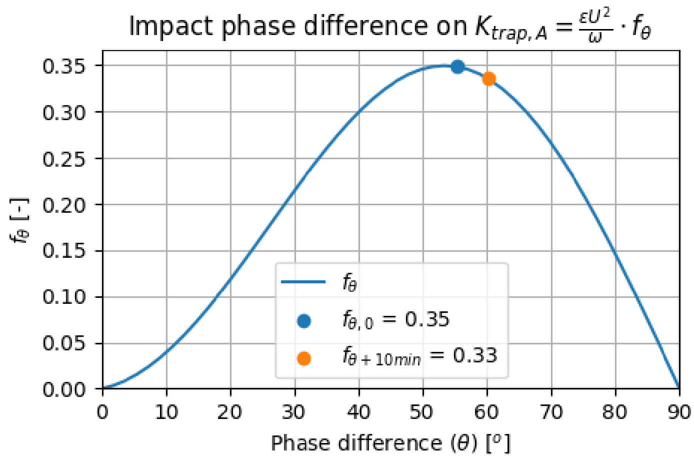

Figure 9.5: Impact of the phase difference on the tidal trapping dispersion coefficient by MacVean and Stacey (2011) at the Hollandsche IJssel

9.3. Impact on salt flux in Lek

The salinity of the Nieuwe Maas at the junction with the Lek is more complex as a second, smaller peak is visible behind the main peak, see figure 9.7. The valley between the two peaks is caused by an earlier outflow of fresher water from the Lek itself, while the flow in the Noord is not yet fully reversed, see figure 9.6. This makes the first estimate of the impact on salt intrusion in the Lek more complex.

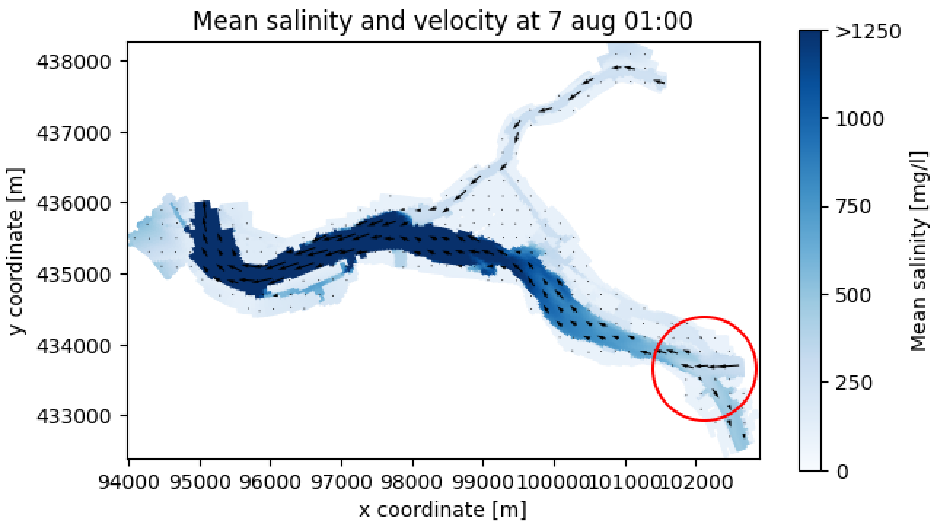

Figure 9.6: Mean salinity in the Nieuwe Maas at 07-08-2018 01:00. Arrows show flow velocity magnitude and direction. The red circle indicates the junction between the Nieuwe Maas, Lek and Noord. Results are retrieved from the RMM3D model

The second peak originating from the Noord reduces the time that the salinity is at the background concentration. An increase in phase difference can still further minimize salt intrusion as the moment of inflow is not yet at the end of the second peak. In addition, the salinity in the Lek will not immediately increase to the concentration in the Nieuwe Maas.

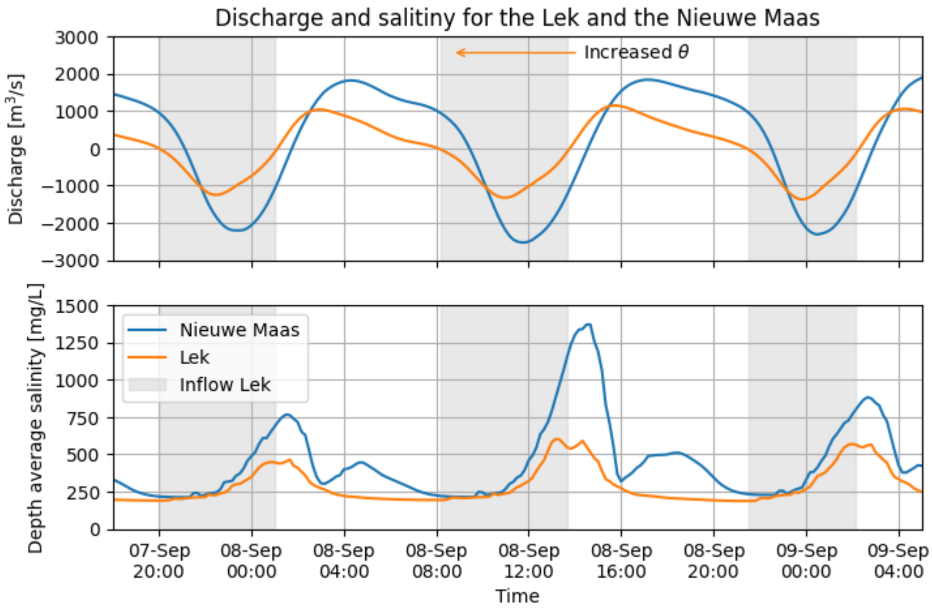

Figure 9.7: Moments of inflow for the Lek compared to salinity in Nieuwe Maas. The arrow indicates the direction of the shift for the discharge signal of the Lek for an increased phase difference. Results are retrieved from the RMM3D model

The same first estimate of salt flux is made for the Lek, as was done with the Hollandsche IJssel. However, as more possible solutions are available, an additional scenario with an increased phase difference of 20 minutes is added. Figure 9.8 shows a decrease of up to 15% and 20% for the inward salt flux, for an increase in 10 and 20 minutes in phase difference, respectively.

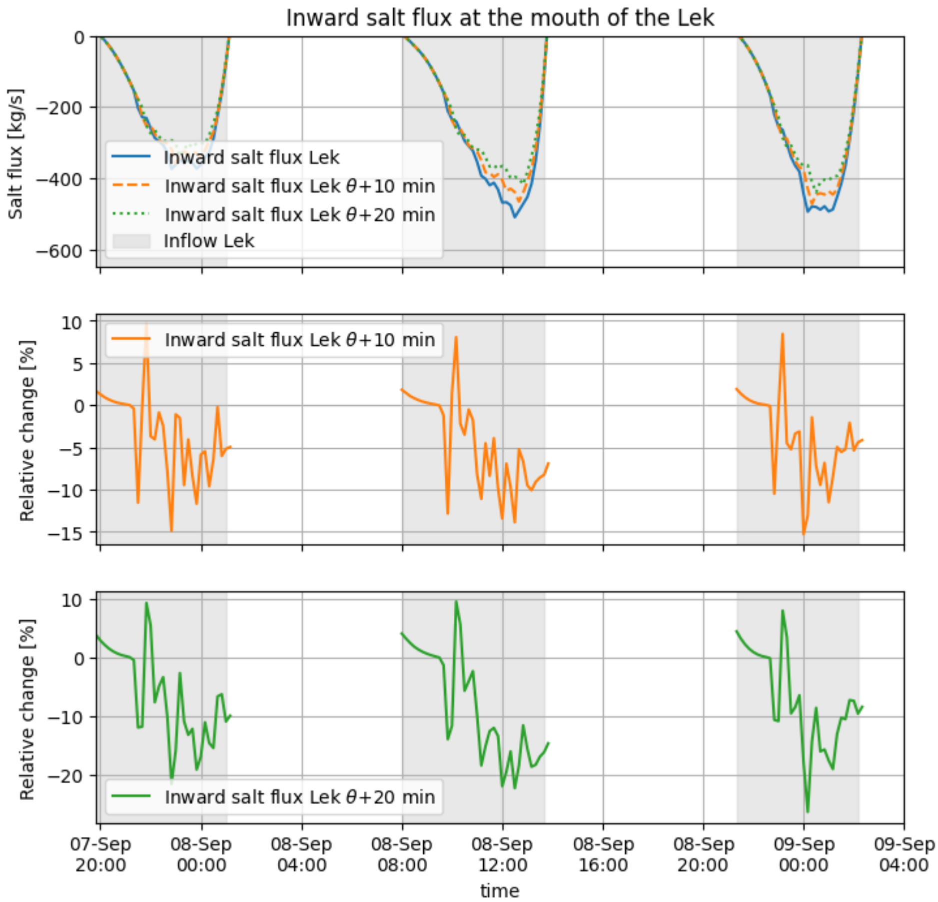

Figure 9.8: Inward salt flux at the Lek for the current situation and an increased phase difference of 10 and 20 minutes

The impact of the increased phase difference on the Nieuwe Maas is calculated based on the dispersion coefficient of MacVean and Stacey (2011). The results are visible in figure 9.9 and show a relative increase in the dispersion coefficient of 19% and 35%, for a phase difference increase of 10 and 20 minutes respectively. So, an increase in phase difference reduces the salt intrusion in the Lek but will increase salt intrusion in the Nieuwe Maas and Noord.

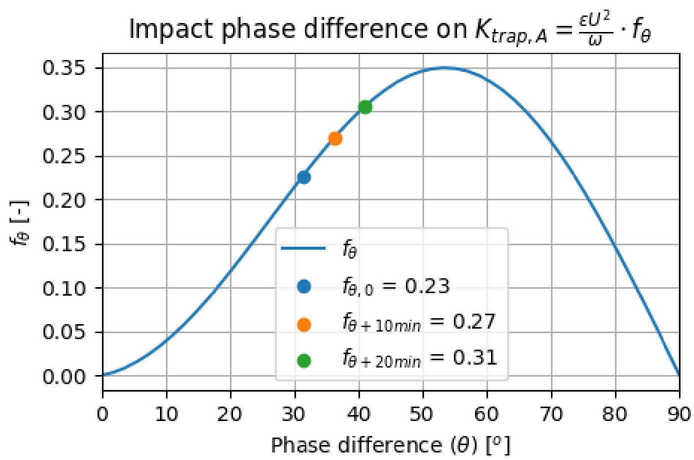

Figure 9.9: Impact of the phase difference on the tidal trapping dispersion coefficient by MacVean and Stacey (2011) at the Lek

9.4. Conclusion

Based on the current salt concentrations in the Nieuwe Maas and the in and outflow patterns of the Hollandsche IJssel and the Lek, an increase in phase difference is expected to result in a decrease in salt intrusion in the side channels. A comparison is made between the Hollandsche IJssel and the Lek, by determining the required change in geometry for a 10-minute increase in the phase difference. For the Hollandsche IJssel, a decrease in length of 10 km can cause an increased phase difference of 10 minutes. The impact of the increased phase difference is quantified by a first estimate of the change in salt flux, by solely shifting the discharge signal. This increase in phase difference would result in a reduction of the salt flux into the Hollandsche IJssel of up to 25% on average. A first estimate of the impact on the Nieuwe Maas is made with the dispersion coefficient of MacVean and Stacey (2011). This showed a decrease in the dispersion coefficient of 4% for a 10-minute increase in the phase difference.

The phase difference at the Lek can be improved to minimize salt intrusion with multiple geometric changes and can be increased by 10 or 20 minutes. The length needs to be decreased by 4 km or the depth needs to be increased by 0.85 m to reach an increased phase difference of 10 minutes, resulting in a decreased salt flux of up to 15% on average. A decrease of 8 km in length or an increase of 1.95 m in depth results in an increased phase difference by 20 minutes and a reduction in the inward salt flux of up to 20% on average. A first estimate is made based on the dispersion coefficient of MacVean and Stacey (2011), which shows that an increased phase difference of 10 and 20 minutes increases the dispersion coefficient by 19% and 35%, respectively.

Part IV

Discussion and conclusion

10 Discussion

In this chapter, we reflect on the methods used and their limitations. In addition, we evaluate the meaning and the implications of the results. This discussion is further split into three sections: the analytical model, phase differences in the Rhine Meuse Delta and the first estimate of salt intrusion. The aforementioned aspects will be evaluated for each section.

10.1. Analytical model

We systematically investigated the impact of the geometry of the side channel on the flow characteristics and the velocity phase difference between the main and side channels. This is done with an analytical model, which describes the propagation of a harmonic wave in a single junction network of prismatic channels.

For this research, an analytical model was chosen as the objective is to acquire additional insights into the processes at play. The analytical model provides additional information about the outgoing and returning waves, which collectively construct the total solution. This model is first used to find general patterns for each variable in a simplified model containing a single junction. The analytical model has a low computational cost, which allows for multiple variables across a large range to be investigated.

First, the abilities and limitations of the analytical model are discussed. The analytical model is a simplified representation of reality, and the impact of these simplifications will be discussed in the following paragraphs. The model neglects certain aspects such as advective acceleration, nonlinear friction, complex geometry and floodplains. However, the analytical model showed it can represent the main tidal constituent well, as the main flow is adequately represented within these simplifications. Higher tidal constituents are not as well represented in the analytical model. A comparison between the RMM3D model and the analytical model is made with the same method as described in chapter 8.2. The results in table 10.1 show that especially for the Lek the higher harmonics are not well represented. The differences can be ascribed to the generation of higher tidal constituents within the network through advection and quadratic friction (Bosboom and Stive, 2021).

Location	Tidal component and amplitude [m]		Water level amplitude RMM3D [m]	Water level amplitude analytical model [m]
End of the Hollandsche IJssel	M4	0.27	0.311	0.282
	M6	0.057	0.100	0.183
End of the Lek	M4	0.27	0.156	0.297
	M6	0.057	0.041	0.130

Table 10.1: Comparison of the water level amplitudes between the RMM3D results and the analytical model of the RMD for multiple constituents at the end of the Hollandsche IJssel and the Lek

The bottom slope in a multi-branch system is not implemented in the analytical model. The impact of the bottom slope becomes more significant the further the research area is located upstream. The bottom slope of the Rhine in the Netherlands varies from 0.11 m/km at Lobith to 0 m/km at the North Sea (Frings et al., 2019). The bed slope in a river causes the formation of backwater curves, with variations in the depth along the channel. This reduces the depth and increases friction, which prevents the tide from reaching as far inland as without a bed slope (Deleersnijder et al., 2019). So, the impact of the bottom slope in the analytical model is expected to have a similar sign as the variations to the friction coefficient in the main channel. Thus, the phase difference would be reduced and brings the results from the analytical model closer to the RMM3D results. It is however not expected that the bed slope is solely responsible for the 10° difference between the analytical and RMM3D model, as this would require a significant increase in effective friction.

The analytical model is validated against river discharge distributions within the Rhine Meuse Delta. Additionally, the water level amplitudes at the end of the Lek and Hollandsche IJssel are compared to the RMM3D model, as these two branches form the main area of interest. Although the results are slightly different for this analytical model, an adequate match was found for both the discharge and the water level amplitude of the main tidal constituent. This provides confidence that the model captures the most important processes and that it can be used for a better understanding of the processes at play and determining the dominant factors affecting the phase difference. Comparison to the RMM3D results showed that the analytical model can predict the order of magnitude and the correct sign of the change in phase difference caused by changes to the geometry.

The agreement between the analytical model and the RMM3D results can be improved by adjusting the number of sections in the network and their initial values. Currently, a representative main value for the width is used, but these values were not available for the depth and friction. So, these variables can be improved to better represent the friction and conveyance cross-sectional area in the prismatic channels. Additionally, more channel sections allow for a better representation of the change in cross-section along the channel. However, this model was not made to represent the RMM3D data as accurately as possible, but rather to acquire insight into the impact of geometry changes on the phase difference. So, the current setup is deemed adequate.

Next, the results from the analytical model are evaluated. The analytical model is used to investigate a total of ten variables. These include four variables of the side channel: width, depth, length and friction coefficient. Furthermore, three main channel variables have been investigated: the width, the depth and the friction coefficient. At last, three boundary conditions are investigated, the tidal amplitude, a river discharge in the main channel and a river discharge in the side channel. The analytical model gave insight into the impact of each variable on the flow characteristics and how this influenced the phase difference.

Although the analytical model is a simplified representation of reality which limits the use of this model, it is competent within these limits. So, the results of this study show which variables are most important regarding changes to the phase difference. It is tried to determine the impact for a general case, however, the impact of each variable is dependent on the initial geometry of the network. Overall the length of the side channel shows the largest impact on the phase difference. The length is directly related to the type of wave which can occur in the channel and the length is the main variable in determining if resonance can occur. The depth is the second most significant variable. It impacts the friction and thus transforms waves towards standing or propagating. Additionally, it impacts the resonance of the side channel, as the friction decreases the channel length for which resonance occurs.

Some of the investigated variables showed significant changes in the phase difference, but they are hard to change in reality, such as the tidal amplitude. It is still useful to know how it impacts the phase difference but it can likely not be used to modify the phase difference in practice.

At last, the implications of the analytical model are discussed. The use of the analytical model is not restricted to only the Rhine Meuse Delta. The analytical model can also be applied to other river deltas. It is a simple method to quickly investigate the impact of the geometry on the phase difference in a multi-branch system. Additionally, the method allows for quantitative results, which give the order of magnitude and sign for the change in phase difference. To achieve these results, a more detailed network of the river delta needs to be modelled.

10.2. Phase differences in the Rhine Meuse Delta

The amplitude and phase of a tidal constituent in the Rhine Meuse Delta is determined with a tidal analysis across a moving window of eight tidal cycles. This is done at two cross-sections near the junctions of interest. Subtracting the phase of the main channel from the side channel results in the phase difference between tidal velocities at the junction. In addition, the main tidal constituent regarding tidal trapping is determined with the dispersion coefficient of MacVean and Stacey (2011).

First, we evaluate the used method. A moving tidal window was chosen to investigate variations in the spring-neap cycle. The spring-neap cycle is caused by the different tidal periods of the M2 and S2 constituents. However, we only investigate a single tidal constituent and with this moving window, the impact of the spring-neap cycle can still be investigated.

The dispersion coefficient by MacVean and Stacey (2011) is not fully applicable for determining the main tidal constituent in the current situation. The dispersion coefficient describes the impact of tidal trapping on the main channel, while this research mainly focuses on the impact on the side channel. However, it is expected that the main tidal constituent regarding the phase difference is the same for the main and side channels.

This research focused on the phase difference of the M2 tide. However, adequately representing the time difference between the inflow of the Hollandsche IJssel and the Nieuwe Maas requires the addition of higher tidal constituents, such as M4 and M6. This thesis is not able to encompass all relevant tidal constituents, so it was chosen to focus on the main constituent.

Adding a higher tidal constituent changes the shape of the discharge signal. Higher harmonics with different phases create asymmetries about the horizontal and vertical axis (Bosboom and Stive, 2021). For tidal trapping, the vertical asymmetry is expected to have the largest impact. Suppose the higher harmonics increase the flood velocities. This will shorten the duration of the flood tide and increase the duration of the ebb tide. In addition, the higher velocities mean the momentum of the flood tide increases, while the momentum of the ebb tide decreases. However, the impact on the phase difference is hard to estimate as it depends on the relative increase in velocity in the main and side channels and how those are impacted by friction. A full numerical model, like Delft3D could be used, to investigate this.

Next, the determined phase differences are interpreted and their implications are evaluated. The most significant variables for modifying the phase difference are the length and depth of the side channel. These variables mainly impact the phase difference between the water level and the discharge of the side channel. Additionally, it is expected that an increased phase difference is needed to limit salt intrusion further. Thus, when the current phase difference between the water level and discharge of the side channel is close to 90°, it can hardly increase anymore. So, this means the phase difference between the side and main channel cannot increase significantly and further limitation of salt intrusion is hardly possible.

The phase differences determined from the RMM3D model results show that the M2 phase of the Hollandsche IJssel was 55° ahead of the Nieuwe Maas and 31° ahead at the Lek. However, the phase difference between the water level and discharge of the Hollandsche IJssel is already close to 90°. Thus, improving the phase difference to further limit salt intrusion is hardly possible, while the Lek has multiple possibilities.

As mentioned before, phase differences of 55° and 31° were found at the Hollandsche IJssel and Lek. The single junction network in the analytical model showed a phase difference of 84°. Thus, it can be concluded that the single junction network in the analytical model is not suitable for quantifying changes to the phase difference by geometric variations. In addition, the analytical model of the RMD can quantify changes to the phase difference by geometry variations, as stated in section 10.1.

So, it can be concluded that the different configurations of the analytical model have different functions. The single junction network is useful in determining the main variables and processes which change the phase difference. In addition, a more detailed network, like the RMD network, can be used to quantify a first-order estimate of the impact of a geometric variable on the phase difference.

10.3. Estimated impact of the change in phase difference on the salt intrusion

A first estimate is made to evaluate how alterations in the phase difference affect salt intrusion in both the main and side channels. It is assumed that the phase difference only causes a shift in the current discharge signal of the side channel. This allows us, to calculate the salt flux entering the side channels and compare it to the original situation. Additionally, it is possible to make a first estimate of the impact on the main channel with the dispersion coefficient of MacVean and Stacey (2011), by solely looking at the change in phase difference.

Exact quantification of the impact of tidal trapping is beyond the scope of this thesis. However, this complex process can be quantified by a first estimate as described above. These first estimates allow us to gauge the impact of a change in phase difference.

First, we discuss the simplifications regarding this first estimate. The estimated impact of the phase difference on the salt intrusion in the side channel is a simplification of reality. It is assumed that the phase difference only causes a shift in the current discharge signal of the side channel. Additionally, it requires the assumption that the discharge of the side channel does not impact the salt concentrations of the main channel. If this is the case, tidal trapping can increase the salt dispersion in the main channel, which delays the moment in time when the salt concentrations in the main channel return to the background concentration. Which in turn can cause raised salt concentrations during the start of the inflow of the side channel, thus increasing salt intrusion on the side channel. At last, it is assumed that the change in configuration of the side channel does not significantly impact the tidal dynamics in the whole estuary.

For these first estimates, no feedback mechanisms are taken into account. However, the impact of the phase difference on the main channel is estimated with the dispersion coefficient for tidal trapping by MacVean and Stacey (2011). For this first estimate, only the changes to the phase difference are taken into account. However, the other variables in this formulation cause additional changes.

Within ϵ in the dispersion coefficient, the ratio of side channel volume to main channel volume is present. The change in length decreases the volume of the side channel, which in turn decreases the dispersion coefficient and can slightly offset the negative effect of the increased phase difference. For the increased depth this ratio gets worse as a depth increase is needed for an increased phase difference, which further increases the dispersion coefficient.

Additionally, ϵ shows that the impact of the Lek is larger than the Hollandsche IJssel, as the volumes of both side channels differ. The volumes of the Lek and Hollandsche IJssel are estimated with the geometry of the analytical model. This gives a volume of the Lek of $46.1 \cdot 10^6$ m^3, compared to the $11.2 \cdot 10^6$ m^3 of the Hollandsche IJssel. This is slightly balanced by the difference in velocity amplitude $\hat{U}_m$ in the Nieuwe Maas, as the velocity amplitude is slightly higher at the junction with the Hollandsche IJssel.

The change in geometry can influence additional processes regarding salt intrusion in the entire system and not only the phase difference. For example, many geometric variables influence the tidal prism. An increased tidal prism, for example by an increased depth, is expected to increase the overall amount of salt transported into the system by tidal intrusion (Laan et al., 2023). However, to significantly change the tidal prism of the Rhine Meuse Delta, a large geometric change is required.

Next, the results are evaluated. This first estimate showed that an increase in the phase difference of 10 minutes at the Hollandsche IJssel, results in a decrease of the salt flux by up to 25% on average. For the Lek, an increase of 10 and 20 minutes of the phase difference resulted in a decreased salt flux of up to 15% and 20% on average, respectively.

The simple salt flux analysis showed a difference between the relative change in salt flux at the Hollandsche IJssel and Lek for the same increased phase difference of 10 minutes. This variation can be attributed to the gradient of the salt concentrations at different locations in the Nieuwe Maas. A steeper gradient is visible at the junction with the Hollandsche IJssel than at the Lek. Thus a shift of the discharge at the Hollandsche IJssel results in a more substantial decrease in the salt concentrations which enter the Hollandsche IJssel, resulting in a larger relative change in the salt flux.

Lastly, the implications of the first estimate are discussed. To achieve the 10-minute increase in the phase difference at the Hollandsche IJssel, the length needs to be decreased by 10 km. This has additional consequences for the current role of the Hollandsche IJssel, as many of the in and outlets of the water authorities are located in the last 10 km (Friocourt and Kuijper, 2015). In general, a reduction in length is anticipated to decrease tidal intrusion, as the tidal prism of the channel decreases. This further reduces salt intrusion, on top of a reduced salt intrusion due to the phase difference.

For the Lek, the decrease in length is less significant and fewer in and outlets are impacted. Again, a reduction in length is expected to reduce tidal intrusion and thus further decrease the salt intrusion in the Lek.

An increased phase difference at the Lek, through an increase in depth, is less suitable. Laan et al. (2023) already investigated a 1 m uniform increase in depth of the Lek and noted that the impact of the increased tidal intrusion is larger than the reduction due to a reduced phase difference.

11 Conclusion

The main objective of this research is to investigate the impact of side and main channel geometry on the phase difference causing tidal trapping, and how this impacts the salt dispersion in the side channels.

How does the geometry of the side channel influence the flow characteristics and the velocity phase difference between the main and side channel?

All these results are based on a single junction network with an initial geometry inspired by the Rhine Meuse Delta. A more detailed model of the RMD showed the same patterns, meaning the processes causing the change in phase difference are well captured by this simple model. The phase difference is the lead of the side channel's discharge phase compared to the phase of the discharge of the main channel. Subsequently, when the phase difference of a certain channel section is mentioned it regards the difference in phase between the water level and the discharge of that channel section.

The geometric variables influence the phase difference through the flow characteristics differently. The geometry of the side channel influences the phase difference as follows. The width mainly impacts the phase difference by changing the discharge amplitude in the side channel, but no significant changes occur to the discharge amplitude in the main channel. The increased discharge amplitude of the side channel increases the significance of the side channel compared to the main channel. This forces the phase difference in the main channel towards the current phase difference in the side channel. Which results in a decrease of the phase difference as the width increases. An increased depth reduces the effective friction in the side channel, which in turn changes the type of wave from propagating towards standing and increases the phase difference. The type of wave changes as the returning wave in a channel section becomes more important as friction decreases, thus the wave becomes more like a standing wave. An increased length transforms the wave pattern from standing to propagating and thus reduces the phase difference. A longer side channel allows the friction to work along a larger distance reducing the impact of the returning wave and transforming the wave pattern towards propagating. Additionally, the length determines if resonance can occur and significantly changes the type of wave in the side channel. The friction coefficient reduces the phase difference as it transforms the wave from standing towards propagating.

The geometry of the main channel impacts the phase difference in the following manner. An increased width increases the tidal prism. Additionally, for a narrow main channel, the relative importance of the side channel increases. This forces the phase difference of the main channel before the junction towards the phase difference of the side channel and thus the phase difference decreases. The depth impacts the phase difference through the friction and an increase in depth leads to a decrease in effective friction, which dominates over the increase in discharge amplitude. This reduces the phase difference, as the wave pattern in the main channel becomes more standing and thus matches the already standing wave pattern in the side channel. Additionally, the depth can introduce resonance, which impacts the phase difference more significantly. Lastly, the friction coefficient increases the friction which decreases the phase difference. The friction transforms the waves in the main channel from more standing to propagating.

At last, the forcing of the system influences the phase difference in the following way. The water level amplitude is a tidal property and directly impacts the tidal prism. An increased tidal amplitude increases the tidal prism. Thus, it increases the discharge amplitude in all channel sections, which increases friction and transforms the wave pattern from standing towards propagating. Overall this leads to a decrease in the phase difference. The river discharge influences the friction to change the phase difference. A larger river discharge increases the friction, thus reducing the phase difference.

How do tidal phase differences influence the salt intrusion in the multi-branch Rhine-Meuse delta?

The phase differences in the Rhine Meuse Delta are determined from the results of the RMM3D model at two locations, the junction between the Hollandsche IJssel and the Nieuwe Maas and the junction between the Lek and the Nieuwe Maas. The phase difference of the M2 tide is used, as it was found to be the most important tidal constituent for tidal trapping, according to the dispersion coefficient of MacVean and Stacey (2011). However, the M2 phase difference does not fully represent the time difference between the flow reversal of the side channel and the main channel.

The phase of the side channel leads the phase of the main channel with 55° at the Hollandsche IJssel and 31° at the Lek. These phase differences were found for the most frequent tidal amplitude and total river discharge of 0.87 m and 734 m^3/s, respectively. The phase difference at the Hollandsche IJssel prevents the saltiest water from entering. It causes the outflow of the Hollandsche IJssel to occur at the end of the flood in the Nieuwe Maas. So, the saltiest water at the end of the flood is not transported into the Hollandsche IJssel.

The impact of the phase difference at the Lek is more complex, as the Lek significantly impacts the salinity concentrations in the Nieuwe Maas. The current phase difference at the Lek prevents the saltiest water from entering at the end of the flood period. However, compared to the Hollandsche IJssel, a larger part of the inflow period occurs during this salinity peak in the Nieuwe Maas. Thus the phase difference at the Lek is not as effective as at the Hollandsche IJssel in preventing saltwater from entering the branch.

Is it possible to minimize salt intrusion by altering the phase differences in the system?

The current salt concentration in the Nieuwe Maas and the inflow pattern of the Hollandsche IJssel and Lek show the possibility of further minimising salt intrusion with an increase in the phase difference. A comparison is made between the Hollandsche IJssel and the Lek to find possible solutions to increase the phase difference by 10 minutes. The possibilities to increase the phase difference at the Hollandsche IJssel are limited to decreasing the length by 10 km, as the phase difference of the Hollandsche IJssel is close to 90°. This resulted in a decrease of the salt flux into the Hollandsche IJssel of up to 25% on average.

For the Lek, there are more possibilities to achieve an increased phase difference. Changes to the length and depth are investigated. An increase of 10 minutes, requires a decrease of 4 km in length or a depth increase of 0.85 m. Furthermore, it is possible to increase the phase difference by 20 min, by shortening the Lek with 8 km or deepening the Lek with 1.95 m. The increase of 10 and 20 min resulted in decreased salt fluxes entering the Lek by up to 15% and 20% on average, respectively. The reductions in salt flux differ due to varying gradients in the salt concentrations in the Nieuwe Maas.

According to the dispersion coefficient for tidal trapping of MacVean and Stacey (2011), both channels impact the salt dispersion in the main channel. However, it is expected that the impact of the Hollandsche IJssel is significantly smaller as the volume of the Hollandsche IJssel is four times smaller than the Lek. For the Hollandsche IJssel, a decrease in the dispersion coefficient of 4% was found when increasing the phase difference by ten minutes. Thus, an increased phase is positive for both the salt dispersion in the Hollandsche IJssel and the Nieuwe Maas. The increase of 10 and 20 minutes at the Lek, resulted in an increased dispersion coefficient of MacVean and Stacey (2011) by 19% and 35%, respectively. Thus, an increased phase difference at the Lek negatively impacts the salt intrusion in the Nieuwe Maas and positively in the Lek.

The acquired results are made as first estimates, which assume solely a shift in the discharge signal of the side channel. Additionally, it is assumed that no feedback mechanisms occur by changing the phase difference and that the salinity in the Nieuwe Maas is not greatly altered by a change in tidal prism due to changes to the geometry.

Bibliography

Battjes, Jurjen A. and Robert Jan Labeur (2017). *Unsteady Flow in Open Channels*. Cambridge: Cambridge University Press. ISBN: 9781107150294. DOI: DOI:10.1017/9781316576878. URL: https://www.cambridge.org/core/books/unsteady-flow-in-open-channels/5CCE099F37BCC5AF4E67B35F15666E7B.

Bosboom, Judith and Marcel JF Stive (2021). *Coastal dynamics*. TU Delft Open. ISBN: 978-94-6366-371-7. DOI: https://doi.org/10.5074/T.2021.001.

Cox, J. R., Y. Huismans, S. M. Knaake, J. R. F. W. Leuven, N. E. Vellinga, M. van der Vegt, A. J. F. Hoitink, and M. G. Kleinhans (2021). "Anthropogenic Effects on the Contemporary Sediment Budget of the Lower Rhine-Meuse Delta Channel Network". In: *Earth's Future* 9.7, e2020EF001869. ISSN: 2328-4277. DOI: https://doi.org/10.1029/2020EF001869. URL: https://agupubs.onlinelibrary.wiley.com/doi/abs/10.1029/2020EF001869.

Deleersnijder, E., A. J. F. Hoitink, K. Kästner, N. S. Ningsih, and P. J. J. F. Torfs (2019). "Propagation of tides along a river with a sloping bed". In: *Journal of Fluid Mechanics* 872, pp. 39–73. ISSN: 0022-1120. DOI: 10.1017/jfm.2019.331. URL: https://www.cambridge.org/core/product/2728C6EAEB2B06F56FBCA61AE60680A1.

Dronkers, J. J., J. C. Schönfeld, and A. Waalewijn (1959). *Tidal computations in shallow water-Report on hydrostatic levelling across the Westerschelde*. Report. Rijkswaterstaat. URL: http://resolver.tudelft.nl/uuid:44f95097-c172-46f2-bd3f-7477fc42c474.

Fischer, H. B. (1976). "Mixing and Dispersion in Estuaries". In: *Annual Review of Fluid Mechanics* 8.1, pp. 107–133. DOI: 10.1146/annurev.fl.08.010176.000543. URL: https://doi.org/10.1146/annurev.fl.08.010176.000543.

Frings, R., G. Hillebrand, N. Gehres, K. Banhold, S. Schriever, and T. Hoffmann (2019). "From source to mouth: Basin-scale morphodynamics of the Rhine River". In: *Earth-Science Reviews* 196. DOI: 10.1016/j.earscirev.2019.04.002.

Friocourt, Y. and C. Kuijper (2015). *Verificatie 3D hydrodynamisch model Hollandsche IJssel voor verziltingsvraagstukken : onderdeel KPP B&O waterkwaliteitsmodelschematisaties 2014*. Report. Deltares. URL: https://kennisbank.deltares.nl/Details/fullCatalogue/1000009376.

Friocourt, Y., K. Kuijper, N. Leung, M. Tiessen, and M. Mens (2020). *Zoutindringing*. Report. Deltares. URL: https://www.stowa.nl/sites/default/files/assets/DELTAFACTS/Deltafacts%20NL%20PDF/Zoutindringing%2020201111.pdf.

Garcia, A. M. P., W. R. Geyer, and N. Randall (2022). "Exchange Flows in Tributary Creeks Enhance Dispersion by Tidal Trapping". In: *Estuaries and Coasts* 45.2, pp. 363–381. DOI: 10.1007/s12237-021-00969-4. URL: https://doi.org/10.1007/s12237-021-00969-4.

Google Earth Pro (2022). *Hollandsche IJssel*. Map. Accesed: 11 August 2023.

Hansen, D. V. and M. Rattray Jr. (1966). "NEW DIMENSIONS IN ESTUARY CLASSIFICATION 1". In: *Limnology and Oceanography* 11.3, pp. 319–326. ISSN: 0024-3590. DOI: https://doi.org/10.4319/lo.1966.11.3.0319. URL: https://aslopubs.onlinelibrary.wiley.com/doi/abs/10.4319/lo.1966.11.3.0319.

Huismans, Y., C. Kuijper, W. M. Kranenburg, S. de Goederen, H. Haas, and N. Kielen (2017). "Predicting salinity intrusion in the Rhine-Meuse Delta and effects of changing the river discharge distributions". In: *Netherlands Centre for River Studies*.

Jay, D. A. (1991). "Green's law revisited: Tidal long-wave propagation in channels with strong topography". In: *Journal of Geophysical Research: Oceans* 96.C11, pp. 20585–20598. ISSN: 0148-0227. DOI: https://doi.org/10.1029/91JC01633. URL: https://doi.org/10.1029/91JC01633.

Kranenburg, W. M., T. Van der Kaaij, M. Tiessen, Y. Friocourt, and M. Blaas (2022). "Salt intrusion in the Rhine Meuse Delta: Estuarine circulation, tidal dispersion or surge effect". In: *Proceedings* *of the 39th IAHR World Congress. June. Granada, Spain*, pp. 5601–5608. DOI: https://doi.org/10.3850/IAHR-39WC2521711920221058.

Kuijper, C. (2015). *Analyse debiet- en zoutmetingen Hollandsche IJssel*. Report. Deltares.

Kuijper, C. (2016). *Analyse van de zoutmetingen in november 2015 langs de Hollandsche IJssel*. Report. Deltares.

Laan, S., V. Chavarrias, Y. Huismans, and R. M. Van der Wijk (2021). *Verzilting Hollandsche IJssel en Lek*. Report. Deltares.

Laan, S., Y. Huisman, R. Socorro, L. Leummens, and W. M. Kranenburg (2023). *Effect bodemligging op verzilting Nieuwe Waterweg, Nieuwe Maas en Lek ten behoeve van de Basisrivierbodemligging (BRL)*. Report. Deltares.

Lindeboom, H. (2002). “The coastal zone: an ecosystem under pressure”. In: *Oceans 2020: science, trends and the challenge of sustainability*, pp. 49–84.

Lorentz, H. A. (1926). *Verslag van de commissie Lorentz (gevolgen afsluiting Zuiderzee op het getij)*. Report. Algemene Landsdrukkerij. URL: http://resolver.tudelft.nl/uuid:f5a4fe20-b26a-4875-9f96-6be04ba16c59.

MacVean, L. J. and M. T. Stacey (2011). “Estuarine Dispersion from Tidal Trapping: A New Analytical Framework”. In: *Estuaries and Coasts* 34.1, pp. 45–59. DOI: 10.1007/s12237-010-9298-x. URL: https://doi.org/10.1007/s12237-010-9298-x.

Mateus, M., J. W. Baretta, and R. Neves (2008). “The continuous challenge of managing estuarine ecosystems”. In: *Perspectives on Integrated Coastal Zone Management in South America*, pp. 15–28.

Mazure, J. P. (1937). “De berekening van getijden en stormvloeden op benedenrivieren”. Thesis. TU Delft. DOI: http://resolver.tudelft.nl/uuid:42258e53-ce1d-4cee-b197-025374e857e6.

Nijs, M. A. J. de, J. D. Pietrzak, and J. C. Winterwerp (2011). “Advection of the Salt Wedge and Evolution of the Internal Flow Structure in the Rotterdam Waterway”. In: *Journal of Physical Oceanography* 41.1, pp. 3–27. DOI: https://doi.org/10.1175/2010JPO4228.1. URL: https://journals.ametsoc.org/view/journals/phoc/41/1/2010jpo4228.1.xml.

Okubo, A. (1973). “Effect of shoreline irregularities on streamwise dispersion in estuaries and other embayments”. In: *Netherlands Journal of Sea Research* 6.1, pp. 213–224. DOI: https://doi.org/10.1016/0077-7579(73)90014-8. URL: https://www.sciencedirect.com/science/article/pii/0077757973900148.

Rijkswaterstaat (2021). *Hollandsche IJsselkering*. Figure. Accesed: 28 Februari 2024. URL: https://www.facebook.com/Rijkswaterstaat/photos/a.396399703720356/4442941179066168/?type=3.

Rijkswaterstaat (n.d.[a]). *Haringvlietsluizen*. Web Page. Accesed: 19 July 2023. URL: https://www.rijkswaterstaat.nl/water/waterbeheer/bescherming-tegen-het-water/waterkeringen/deltawerken/haringvlietsluizen.

Rijkswaterstaat (n.d.[b]). *Rivieren*. Web Page. Accesed: 24 July 2023. URL: https://www.rijkswaterstaat.nl/water/waterbeheer/beheer-en-ontwikkeling-rijkswateren/rivieren.

Schijf, J. B. and J. C. Schönfeld (1953). “Theoretical considerations on the motion of salt and fresh water”. In: *Proceedings Minnesota International Hydraulic Convention*. IAHR. URL: http://resolver.tudelft.nl/uuid:5d1c2eb0-d51c-4b3c-ad77-a77513941c6c.

Scott, D. W. (2011). “Sturges’ and Scott’s Rules”. In: *International Encyclopedia of Statistical Science*. Ed. by Miodrag Lovric. Berlin, Heidelberg: Springer Berlin Heidelberg, pp. 1563–1566. ISBN: 978-3-642-04898-2. DOI: 10.1007/978-3-642-04898-2_578. URL: https://doi.org/10.1007/978-3-642-04898-2_578.

Simpson, J. H. (1997). “Physical processes in the ROFI regime”. In: *Journal of Marine Systems* 12.1, pp. 3–15. DOI: https://doi.org/10.1016/S0924-7963(96)00085-1. URL: https://www.sciencedirect.com/science/article/pii/S0924796396000851.

Tiessen, M., W. M. Kranenburg, J. Ter Maat, Y. Huisman, C. Kuijper, M. Mens, and R. M. Van der Wijk (2016). *Systeemanalyse van de Rijn-Maasmonding voor verzilting*. Report. Deltares. URL: https://www.deltares.nl/expertise/publicaties/systeemanalyse-van-de-rijn-maasmonding-voor-verzilting-synopsis-en-deelrapporten-2016.

TwynstraGudde and HydroLogic (2019). *Handreiking Verzilting*. Report. Rijkswaterstaat. URL: https://www.helpdeskwater.nl/publish/pages/162129/190319_handreiking_verzilting_openbaar.pdf.

Valle-Levinson, A. (2010). *Contemporary Issues in Estuarine Physics*. Cambridge: Cambridge University Press. ISBN: 9780521899673. DOI: DOI:10.1017/CBO9780511676567. URL: https://www.cambridge.org/core/product/5D204C31934B0B3E87EB1B7D0325DA2D.

Van der Kaaij, T. and V. Chavarrias (2020). *D-HYDRO RijnMaasMonding 3D; Zoutindringing in de Nieuwe Waterweg : werkzaamheden 2020*. Report. Deltares.

Van der Kaaij, T., V. Chavarrias, and W. M. Kranenburg (2022). *RMM 3D, een nieuw 3D model van de RijnMaasMonding in D-HYDRO; Vergelijking met zout- en debietmetingen najaar 2018*. Report. Deltares.

Van der Wijk, R. M., T. Van der Kaaij, and W. M. Kranenburg (2019). *Data-analyse verzilting Hollandsche IJssel en Lek droogteperiode 2018*. Report. Deltares.

Werkgroep Slim Watermanagement, Rijn-Maasmonding (2019). *Hollandsche IJssel - Slim Watermanagement Redeneerlijn Watertekort*. Report. HydroLogic. URL: https://open.rws.nl/open-overheid/onderzoeksrapporten/@195399/rijn-maasmonding-slim-watermanagement/.

Werkgroep Slim Watermanagement, Rijn-Maasmonding (2021). *Rijn-Maasmonding: Slim Watermanagement Redeneerlijn Watertekort*. Report. HydroLogic. URL: https://open.rws.nl/open-overheid/onderzoeksrapporten/@195399/rijn-maasmonding-slim-watermanagement/.

Zijl, F., S. Laan, and J. Groenenboom (2021). *Development of a 3D model for the NW European Shelf (3D DCSM-FM)*. Report. Deltares. URL: https://kennisbank.deltares.nl/Details/fullCatalogue/1000004150.

Zijl, F. and J. Veenstra (2018). *The 3D Dutch Continental Shelf Model - Flexible Mesh (3D DCSMFM) : setup and validation*. Report. Deltares.

Part V

Appendix

A

Development and validation analytical model

This appendix continues the matrix set-up of the analytical model for a single junction network and a network containing a loop. Followed by the validation of the implementation in MATLAB.

A.1. Continuation development analytical model

The single junction network is an extension of the two channels in series, see figure A.1. The section c adds only three new equations to the matrix. These are the four-pole equations regarding section c and the water level transition condition. The new water level transition condition combined with the already implemented water level transition condition between sections a and b, fulfils the requirement that all water levels at the junction should be equal. The discharge transition condition for a single junction results in the modification of the already implemented discharge transition condition. As the sum of the discharges at the junction should be zero, the addition of section c introduces an extra term to this sum and not a new equation. This is indicated with a blue square in the matrix.

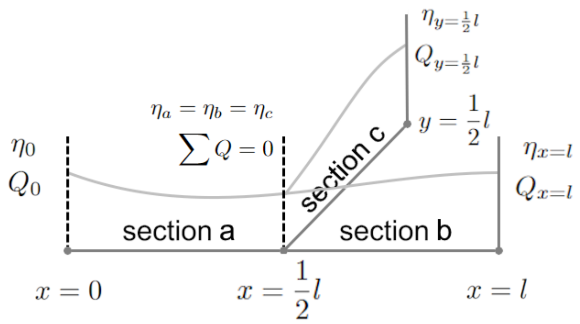

Figure A.1: Analytical model of a single junction network

$$
\begin{array}{c}
\text{section a} \qquad\qquad \text{section b} \qquad\qquad\qquad \text{section c} \\
\begin{bmatrix}
f & f & 0 & 0 & 0 & 0 & 0 & 0 & 0 \\
-f & f & 0 & 0 & 0 & \boxed{-1} & 0 & 0 & 0 \\
0 & 0 & f & f & \boxed{-1} & 0 & 0 & 0 & 0 \\
0 & 0 & -f & f & 0 & 0 & 0 & 0 & 0 \\
1 & 0 & 0 & 0 & -1 & 0 & 0 & 0 & 0 \\
0 & 0 & 0 & -1 & 0 & 1 & 0 & \boxed{-1} & 0 \\
0 & 0 & 0 & 0 & 0 & 0 & f & f & \boxed{-1} \\
0 & 0 & 0 & 0 & 0 & 0 & -f & f & 0 \\
0 & 0 & 0 & 0 & 1 & 0 & 0 & 0 & -1
\end{bmatrix}
\end{array}
\begin{bmatrix}
\tilde{\eta}_{1a} \\ \tilde{Q}_0 \\ \tilde{\eta}_2 \\ \tilde{Q}_{1b} \\ \tilde{\eta}_{1b} \\ \tilde{Q}_{1a} \\ \tilde{\eta}_3 \\ \tilde{Q}_{1c} \\ \tilde{\eta}_{1c}
\end{bmatrix}
=
\begin{bmatrix}
\tilde{\eta}_0 \\ 0 \\ 0 \\ \tilde{Q}_2 \\ 0 \\ 0 \\ 0 \\ \tilde{Q}_3 \\ 0
\end{bmatrix}
\begin{array}{l}
\text{Four-pole equation} \\
\text{Four-pole equation} \\
\text{Four-pole equation} \\
\text{Four-pole equation} \\
\text{Water level transition condition} \\
\text{Discharge transition condition} \\
\text{Four-pole equation} \\
\text{Four-pole equation} \\
\text{Water level transition condition}
\end{array}
\tag{A.1}
$$

Matrix for a single junction network. f indicates parts of the rewritten four-pole equations. The dashed lines indicate which part of the matrix is related to a channel section. The red squares indicate the former righthand side of the rewritten four-pole equations. The blue square indicates the location of the changed transition condition of the discharge.

The channel network which includes a loop is a further extension of the single junction network. The main channel is extended to include a third section and the side channel is continued towards the main channel. This results in the network as shown in figure A.2. The addition of section e introduces 5 additional equations. The first two are the rewritten Four-pole equations for section e. Followed by the water level and discharge transition condition between sections d and e. The last equation is the water level transition condition between sections c and e, to fulfil the requirement that all water levels should be equal at the junction. As section e completes the loop and forms a junction, the discharge transition condition between sections b and c needs to be modified. As the positive direction in section e is from the side channel to the main channel, the addition to the discharge transition condition is positive, as shown in the second blue square in the matrix below.

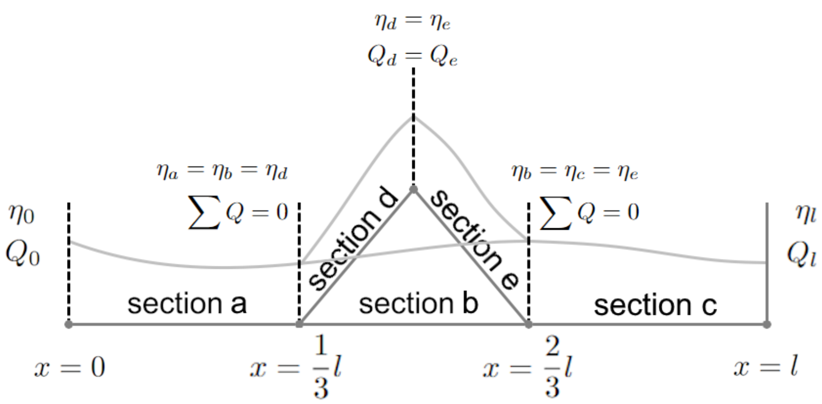

Figure A.2: Analytical model of a network with a loop section a section b section c section d section e

$$
\begin{bmatrix}
f & f & 0 & 0 & 0 & 0 & 0 & 0 & 0 & 0 & 0 & 0 & 0 & 0 & 0 & 0 & 0 & 0 \\
-f & f & 0 & 0 & 0 & \boxed{-1} & 0 & 0 & 0 & 0 & 0 & 0 & 0 & 0 & 0 & 0 & 0 & 0 \\
0 & 0 & f & f & \boxed{-1} & 0 & 0 & 0 & 0 & 0 & 0 & 0 & 0 & 0 & 0 & 0 & 0 & 0 \\
0 & 0 & -f & f & 0 & 0 & 0 & 0 & 0 & \boxed{-1} & 0 & 0 & 0 & 0 & 0 & 0 & 0 & 0 \\
1 & 0 & 0 & 0 & -1 & 0 & 0 & 0 & 0 & 0 & 0 & 0 & 0 & 0 & 0 & 0 & 0 & 0 \\
0 & 0 & 0 & -1 & 0 & 1 & 0 & 0 & 0 & 0 & 0 & \boxed{-1} & 0 & 0 & 0 & 0 & 0 & 0 \\
0 & 0 & 0 & 0 & 0 & 0 & f & f & \boxed{-1} & 0 & 0 & 0 & 0 & 0 & 0 & 0 & 0 & 0 \\
0 & 0 & 0 & 0 & 0 & 0 & -f & f & 0 & 0 & 0 & 0 & 0 & 0 & 0 & 0 & 0 & 0 \\
0 & 0 & 1 & 0 & 0 & 0 & 0 & 0 & -1 & 0 & 0 & 0 & 0 & 0 & 0 & 0 & 0 & 0 \\
0 & 0 & 0 & 0 & 0 & 0 & 0 & -1 & 0 & 1 & 0 & 0 & 0 & 0 & 0 & 0 & 0 & \boxed{1} \\
0 & 0 & 0 & 0 & 0 & 0 & 0 & 0 & 0 & 0 & f & f & \boxed{-1} & 0 & 0 & 0 & 0 & 0 \\
0 & 0 & 0 & 0 & 0 & 0 & 0 & 0 & 0 & 0 & -f & f & 0 & 0 & 0 & 0 & \boxed{-1} & 0 \\
0 & 0 & 0 & 0 & 1 & 0 & 0 & 0 & 0 & 0 & 0 & 0 & -1 & 0 & 0 & 0 & 0 & 0 \\
0 & 0 & 0 & 0 & 0 & 0 & 0 & 0 & 0 & 0 & 0 & 0 & 0 & f & f & \boxed{-1} & 0 & 0 \\
0 & 0 & 0 & 0 & 0 & 0 & 0 & 0 & 0 & 0 & 0 & 0 & 0 & -f & f & 0 & 0 & \boxed{-1} \\
0 & 0 & 0 & 0 & 0 & 0 & 0 & 0 & 0 & 0 & 1 & 0 & 0 & 0 & 0 & -1 & 0 & 0 \\
0 & 0 & 0 & 0 & 0 & 0 & 0 & 0 & 0 & 0 & 0 & 0 & 0 & 0 & -1 & 0 & 1 & 0 \\
0 & 0 & 0 & 0 & 0 & 0 & 0 & 0 & 1 & 0 & 0 & 0 & 0 & -1 & 0 & 0 & 0 & 0
\end{bmatrix}
\begin{bmatrix}
\tilde{\eta}_{1a} \\ \tilde{Q}_0 \\ \tilde{\eta}_{2b} \\ \tilde{Q}_{1b} \\ \tilde{\eta}_{1b} \\ \tilde{Q}_{1a} \\ \tilde{\eta}_{3c} \\ \tilde{Q}_{2c} \\ \tilde{\eta}_{2c} \\ \tilde{Q}_{2b} \\ \tilde{\eta}_{4d} \\ \tilde{Q}_{1d} \\ \tilde{\eta}_{1d} \\ \tilde{\eta}_{2e} \\ \tilde{Q}_{4e} \\ \tilde{\eta}_{4e} \\ \tilde{Q}_{4d} \\ \tilde{Q}_{2e}
\end{bmatrix}
=
\begin{bmatrix}
\tilde{\eta}_0 \\ 0 \\ 0 \\ 0 \\ 0 \\ 0 \\ 0 \\ \tilde{Q}_{3c} \\ 0 \\ 0 \\ 0 \\ 0 \\ 0 \\ 0 \\ 0 \\ 0 \\ 0 \\ 0
\end{bmatrix}
\begin{matrix}
\text{F} \\ \text{F} \\ \text{F} \\ \text{F} \\ \text{W} \\ \text{D} \\ \text{F} \\ \text{F} \\ \text{W} \\ \text{D} \\ \text{F} \\ \text{F} \\ \text{W} \\ \text{F} \\ \text{F} \\ \text{W} \\ \text{D} \\ \text{W}
\end{matrix}
\tag{A.2}
$$

Matrix for a network with a loop. f indicates parts of the rewritten four-pole equations. The dashed lines indicate which part of the matrix is related to a channel section. The red squares indicate the former righthand side of the rewritten four-pole equations. The blue square indicates the location of the changed transition condition of the discharge. The column next to the righthand side indicates the type of equation, F is the rewritten Four-pole equation, W is the water level transition condition and D is the discharge transition condition.

A.2. Validation analytical model

The analytical model results are validated with an example from the lecture slides of CTB3350 Open Channel Flow given by Robert Jan Labeur. The initial situation is a semi-closed channel with the sea at the open end. The system parameters are given in table A.1.

Variable	Value	Unit	Variable	Value	Unit
l	50	km	$\hat{Q}$	1800	m^3/s
B	400	m	c_f	0.005	-
A_c	3600	m^2	$\tilde{\eta}_0$	$0.85 \cdot e^{i\pi/6}$	-
R	12	m	$\tilde{Q}_l$	0	-

Table A.1: System parameters of validation

At first, the analytical model is created for a single channel section and validated with the example. Next, the model is extended to include multiple channel sections. The overall length of the channel is kept equal to the validation conditions, as are the channel properties. This results in an equal outcome for the beginning and the end nodes compared to the validation, as is visible in table A.2.

This is followed by extending the analytical model to include a side channel at the split of the previous scenario. The side channel has the same properties as the validation scenario but has a length of 25 km. The implementation is validated by letting the length of one branch of the junction go towards 0. This creates a network which is similar to the validation, as it becomes almost a split channel. First, the newly added side channel is shrunk to a length of almost 0. Next, the main channel branch after the junction is shrunk to a length of almost 0. The results of the two test cases should return the same results. Furthermore, when both side and main channel behind the junction have the same channel properties, the results at both ends should be equal. As can be seen in table A.2, the results are equal at the expected locations. So, it can be concluded that the implementation of the side channels is done correctly.

The last addition to this model is the possibility to form loops with multiple channel sections. The overall length of the channel sections from beginning to end is still 50 km. The loop is formed by adding a side channel which connects back to the main channel. The length from the beginning to the end via the side channel is also 50 km. All remaining channel parameters are kept equal to the validation. By reducing the cross-sectional area of the side channel towards 0, the network again becomes almost a split channel. Next, only the cross-section of the main channel between the side channel junctions is reduced to almost 0. The results along the nodes should be equal to the previous variation and the beginning and end values should be equal to the validation. Finally, the cross-sectional area of both channels between the junctions is halved. The total flow is split equally between both channels and the results at the beginning and end should be equal to the validation in case the overall friction in the network is kept equal. Table A.2 shows that all these results match the validation data when expected, thus the loop implementation is done correctly.

The constant discharge scenario is validated with the momentum balance. For a constant river discharge the acceleration term is 0, thus the pressure gradient and the resistance should balance each other. The change in water level is calculated in equation A.3 and matches the results in table A.2.

$$\begin{aligned} \frac{\partial Q}{\partial t} + gA_c\frac{\partial \eta}{\partial x} + c_f\frac{|Q|Q}{A_cR} &= 0 \\ d\eta = -c_f\frac{|Q|Q}{A_cR} \cdot \frac{dx}{gA_c} &= 0.164 \text{ m} \end{aligned} \tag{A.3}$$

Type	Variation		node 0		node 1		node 2 and node 4 at $t=0$				node 3	
			$\hat{Q}$ [m^3/s]	θ_Q [rad]	$\hat{\eta}$ [m]	θ_η [rad]	η [m]	Q_a [m^3/s]	Q_b [m^3/s]	Q_c [m^3/s]	$\hat{\eta}$ [m]	θ_η [rad]
Validation	$L=50$ km		2788	-	1.080	0.100	-	-	-	-	-	-
Straight channel	$L=50$ km		2788	1.795	1.087	0.103	-	-	-	-	-	-
	$L_{0,2}=L_{2,1}=25$ km		2788	1.795	1.087	0.103	0.996	-197	-197	-	-	-
Single junction	$L_s \to 0$	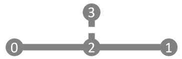	2788	1.795	1.087	0.103	0.996	-197	-197	0	1.015	0.195
	$L_m \to 0$	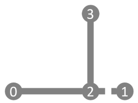	2788	1.795	1.015	0.195	0.996	-197	0	-197	1.087	0.103
	$L_s = L_m$	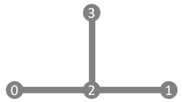	4388	1.517	1.141	-0.175	1.061	455	227	227	1.141	-0.175
Loop	$A_{c,s} \to 0$	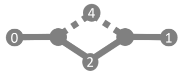	2788	1.795	1.087	0.103	0.996	-197	-197	-	-	-
							-	-	-	-		
	$A_{c,m} \to 0$	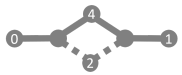	2788	1.795	1.087	0.103	-	-	-	-	-	-
							0.996	-197	-197	-		
	$A_{c,m}=A_{c,s}=\frac{1}{2}A_c$	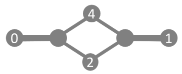	2788	1.795	1.087	0.103	0.996	-98	-98	-	-	-
							0.996	-98	-98	-		
Constant discharge	$L=50$ km		-1000	0	0.164	0	-	-	-	-	-	-

Table A.2: Results for different network types and multiple variations. Subscript s indicates the side channel branch and m indicates main channel branch

B

Salt intrusion Hollandsche IJssel

B.1. Salt intrusion due to raised ebb concentrations

The impact of raised salt concentrations during ebb at Brienenoord is already mentioned in chapter 6. To verify if these results are also visible in the model results of the RMM3D, this process is further investigated.

The RMM3D results show between 1 October and 3 October a raised salt concentration in the Nieuwe Maas during ebb. As can be seen in figure B.1, the 1100 mg/l salt concentration during ebb is a little later visible in the Hollandsche IJssel at Krimpen aan den IJssel. So, this process is well represented in the RMM3D model.

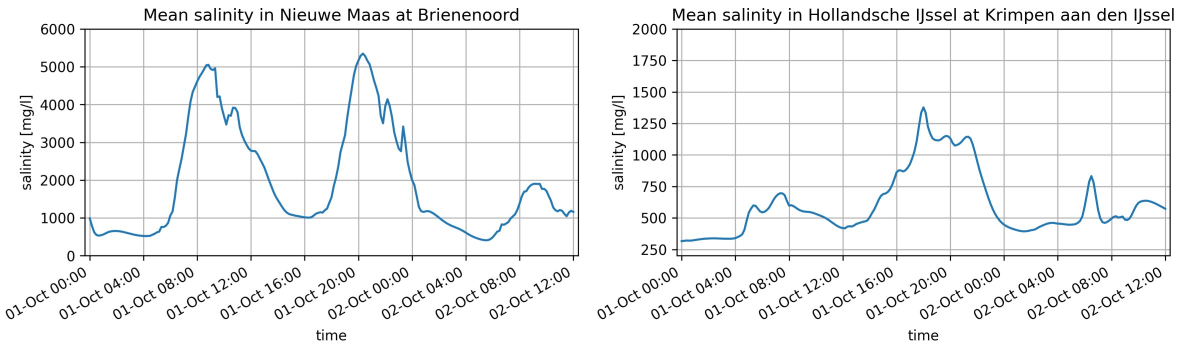

Figure B.1: Salinization Hollandsche IJssel by raised ebb concentrations

B.2. Salt intrusion due to the Sliksloot

The possible impact of the Sliksloot is already stated in section 6. In this section, it will be investigated if the impact of the Sliksloot is also visible in the model results of RMM3D.

The RMM3D model results show on certain occasions salinization of the Hollandsche IJssel before saltier water from Brienenoord has reached the mouth of the Hollandsche IJssel. Next, it is investigated if the Sliksloot causes this or if another process is responsible for the salinization. In figure B.2 is visible that the depth-averaged salt concentrations in the Hollandsche IJssel rise before the depth-averaged salt concentrations in the Nieuwe Maas. Furthermore, the depth-averaged salt concentration in the Sliksloot rises after the concentrations in the Hollandsche IJssel rise. Thus, the saltier water is transported from the Hollandsche IJssel into the Sliksloot, so the Sliksloot is not responsible for this salinization.

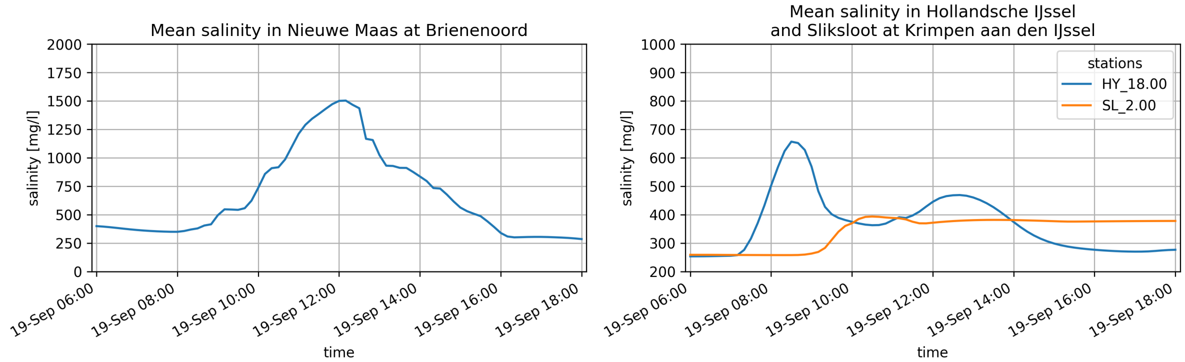

Figure B.2: Salinization Hollandsche IJssel by the Sliksloot. HY_18.00 is located 2 km upstream from the entrance of the Hollandsche IJssel. SL_2.00 is located in the Sliksloot, close to the connection with the Hollandsche IJssel

To get insight into the process behind this salinization case, the salt concentrations and the velocities over the depth are visualized near the mouth of the Hollandsche IJssel. As can be seen in figure B.3, the main salt bubble is located at the bottom of the Hollandsche IJssel. Furthermore, the velocities are at the top of the Hollandsche IJssel directed to the Nieuwe Maas, while the velocities at the bottom are directed into the Hollandsche IJssel. So, the process causing the salinization of the Hollandsche IJssel at this time is an exchange flow, which pulls saltier water into the Hollandsche IJssel and as the flow reverses the salt water bubble gets transported towards Krimpen aan den IJssel.

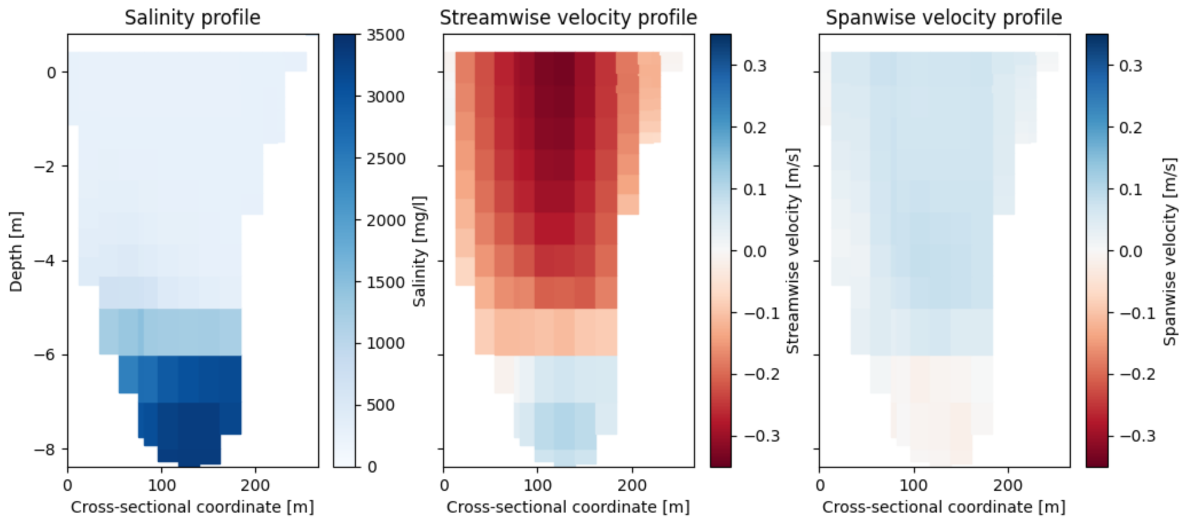

Figure B.3: Salinity and velocity profile at the mouth of the Hollandsche IJssel at 19-09-2018 01:00

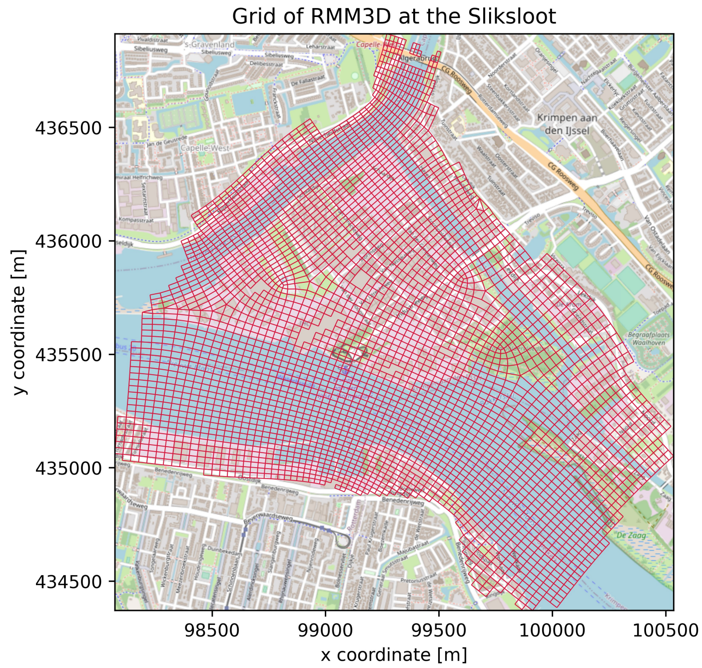

Figure B.4: Grid of the RMM3D model at the Sliksloot

The salinization pattern of the Hollandsche IJssel due to Sliksloot as stated by Laan et al., 2021, was not found in the model results of the RMM3D. To further investigate why the pattern is not visible, the velocities and the model properties in the Sliksloot are further researched. As can be seen in figure B.4, the Sliksloot is a very small channel and in the RMM3D model, it is only represented by one or two grid cells. This makes it more likely that velocities and salt concentrations are not well represented in this channel.

To verify the velocities in the Sliksloot the three main components of the momentum balance are solved roughly. This is based on the water level difference between output point `HY_18.00`, located in the Hollandsche IJssel close to the Sliksloot and `NM_992.00`, in the Nieuwe Maas close to the connection with the Sliksloot. Furthermore, the velocities and changes in velocity are means between output points `SL_1.00` and `SL_2.00`, both are located in the Sliksloot where higher numbers are closer to the Hollandsche IJssel. The friction in the Sliksloot is assumed high as it is a narrow and shallow channel. The result is given in equation B.1 and shows that the order of magnitudes does not always match.

Type	du [m/s]	dt [s]	$d\eta$ [m]	dx [m]	c_f [-]	u [m/s]	η [m]
Hump	0.28	3600	-0.072	2600	0.04	0.14	4
Spike	0.26	1800	-0.005	2600	0.04	0.13	4

Table B.1: Variables momentum balance Sliksloot

$$\begin{gathered}\frac{\partial u}{\partial t} = -g\frac{\partial \eta}{\partial x} - c_f\frac{|u|u}{\eta} \\ \text{Hump: } \mathcal{O}(10^{-5}) = \mathcal{O}(10^{-4}) - \mathcal{O}(10^{-4}) \\ \text{Spike: } \mathcal{O}(10^{-4}) = \mathcal{O}(10^{-5}) - \mathcal{O}(10^{-4})\end{gathered} \tag{B.1}$$

The velocity signal in the Hollandsche IJssel also shows an abnormal pattern. First, a sharp spike in the velocity happens, followed by a more gradual increase and decrease in velocity. The development of

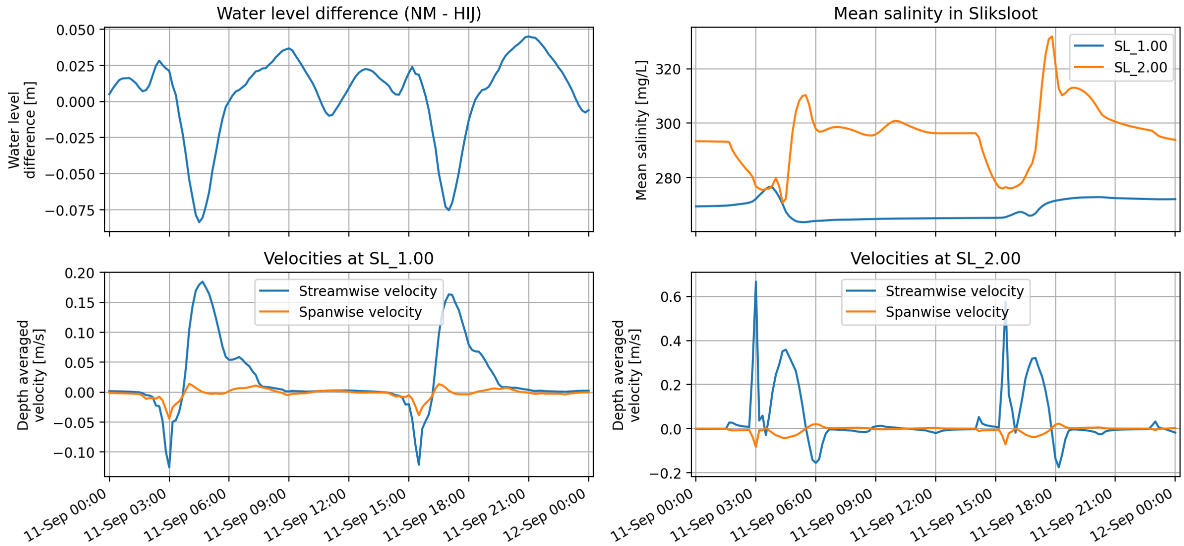

Figure B.5: Velocties in the Sliksloot, where positive velocities mean a flow from the Hollandsche IJssel to the Nieuwe Maas

the spike could not be explained by the momentum balance, as the order of the terms does not sum up to zero. Furthermore, the velocities at locations `SL_1.00` and `SL_2.00` show during these sharp peeks opposite signs, meaning the Sliksloot fills from both sides.

In the end, the statements about the impact of the Sliksloot cannot be verified or debunked, as the RMM3D model does not represent the Sliksloot correctly.

C
Initial values analytical model RMD

The data used to set up the analytical model of the RMD can be found in this appendix. The coordinates of each node can be seen in table C.1 Futhermore, the properties of all sections are given in table C.2.

Node	x [m]	y [m]
0	0	0
1	7000	0
2	20000	0
3	29600	0
4	37000	0
5	40500	0
6	44000	0
7	65000	0
8	86000	0
9	24800	-3600
10	29600	-7200
11	50400	-8800
12	50400	-6800
13	50400	-4800
14	47200	-2400

Node	x [m]	y [m]
15	37000	10000
16	37000	20000
17	24800	-13600
19	20000	-20000
19	50400	-17800
20	50400	-13300
21	54400	-17800
22	65200	-14800
23	65200	-4800
24	74000	-4800
25	116500	-4800
26	159000	-4800
27	57800	-4800
28	7000	-20000

Table C.1: Coordinates of each node in analytical model RMD

Name	Nodes			Length (L) [m]	Width (B) [m]	Depth (d) [m]	Friction coefficient (c_f) [-]
Nieuwe Waterweg	0	-	1	7000	563	17	0.0017
Scheur	1	-	2	13000	469	16.5	0.0015
Nieuwe Maas	2	-	3	9600	391	12	0.0037
Nieuwe Maas	3	-	4	7400	391	12	0.0037
Nieuwe Maas	4	-	5	3500	372	8.5	0.0042
Nieuwe Maas	5	-	6	3500	372	8.5	0.0042
Lek	6	-	7	21000	249	5.5	0.0058
Lek	7	-	8	21000	165	5	0.0089
Oude Maas	2	-	9	6000	299	14	0.0039
Oude Maas	9	-	10	6000	299	14	0.0039
Oude Maas	10	-	11	20861	307	11	0.0048
Oude Maas	11	-	12	2000	294	8	0.0034
Oude Maas	12	-	13	2000	294	8	0.0034
Noord	13	-	14	4000	229	8	0.0031
Noord	14	-	6	4000	229	8	0.0031
Hollandsche IJssel	4	-	15	10000	134	5.5	0.0055
Hollandsche IJssel	15	-	16	10000	96	4	0.0061
Spui	10	-	17	8000	199	7	0.0064
Spui	17	-	18	8000	199	11	0.0056
Haringvliet	18	-	19	30480	1829	10	0.0029
Dordtsche Kil	19	-	20	4500	281	12	0.0023
Dordtsche Kil	20	-	11	4500	281	12	0.0023
Hollands Diep	19	-	21	4000	1170	7	0.0093
Nieuwe Merwede	21	-	22	11209	496	5.5	0.0039
Nieuwe Merwede	22	-	23	10000	496	5	0.0041
Boven Merwede	23	-	24	8800	400	6	0.0026
Waal	24	-	25	42500	304	5	0.0033
Waal	25	-	26	42500	252	4	0.0090
Beneden Merwede	13	-	27	7400	251	6.5	0.0081
Beneden Merwede	27	-	23	7400	251	6.5	0.0081
Haringvliet	18	-	28	13000	1868	9	0.0036

Table C.2: Properties per section in analytical model RMD

D

Water level verification analytical model RMD

The water level amplitude is determined at three locations: the beginning of the Nieuwe Waterweg, the end of the Hollandsche IJssel, and the end of the Lek. The Nieuwe Waterweg determines the amplitude at the beginning of the RMD and the amplitude to use in the analytical model. The Hollandsche IJssel and Lek are further researched, so it is useful to know if the water levels in these branches are represented correctly.

This comparison is made for the three most significant constituents, namely D2, D4 and D6. A linear fit is done through the data of the RMM 3D results, to translate a single amplitude at Hoek van Holland to an amplitude at the end of the Hollandsche IJssel or Lek. If the slope coefficient of the linear fit through the points is greater than 1, the amplitude is amplified in the system and with values below 1 damping occurs.

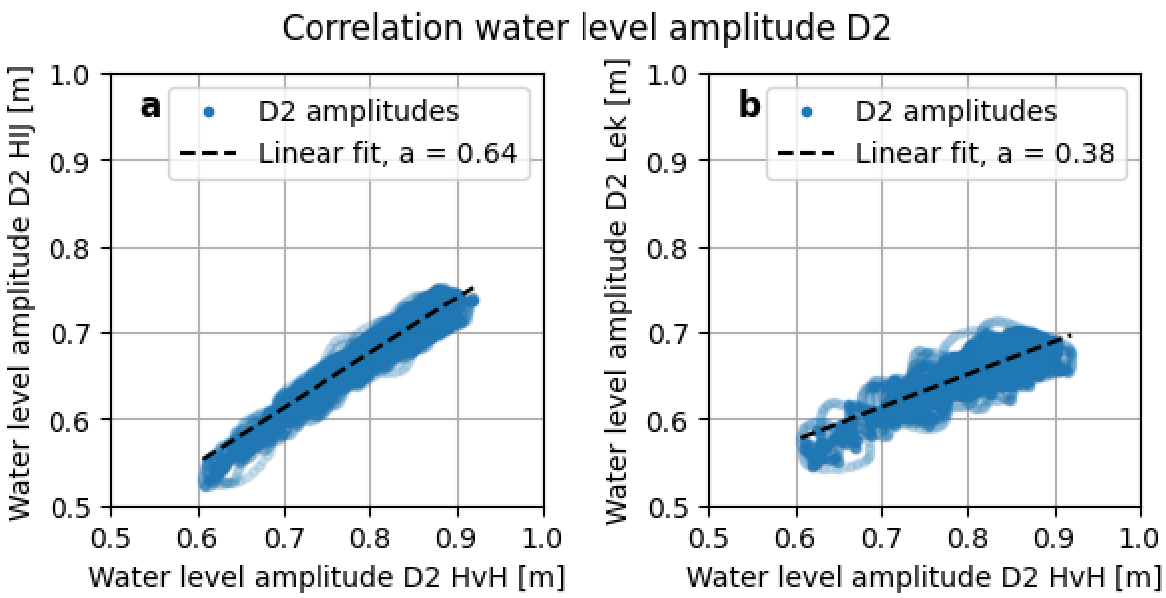

Figure D.1: Correlation between water level amplitudes of D2. **(a)** Amplitudes at Hoek van Holland and the end of the Hollandsche IJssel. **(b)** Amplitudes at Hoek van Holland and the end of the Lek.

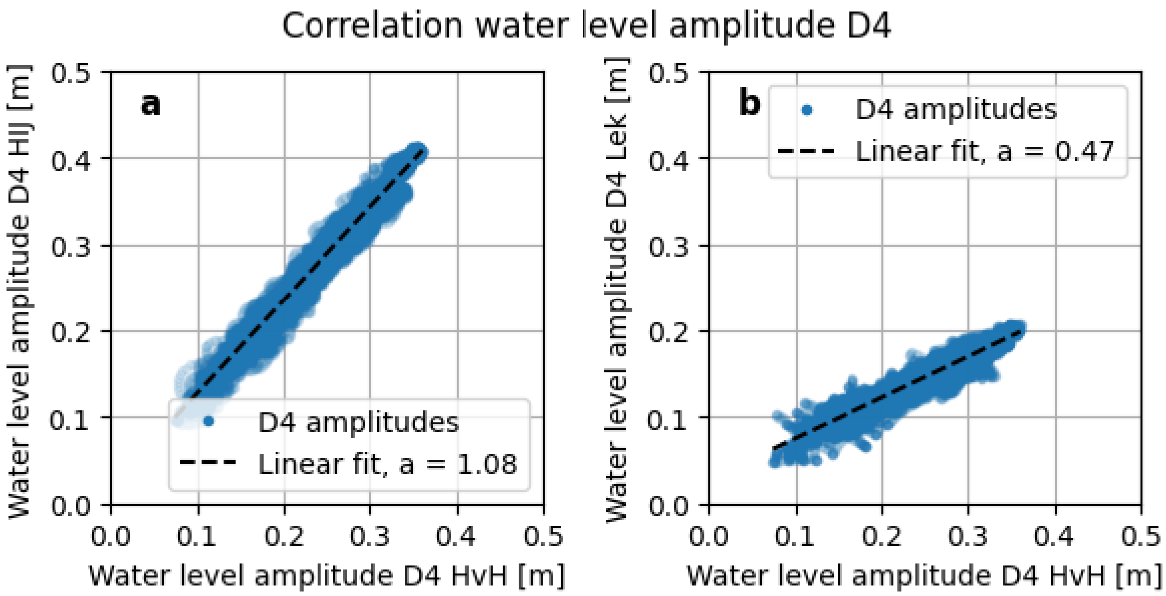

Figure D.2: Correlation between water level amplitudes of D4. **(a)** Amplitudes at Hoek van Holland and the end of the Hollandsche IJssel. **(b)** Amplitudes at Hoek van Holland and the end of the Lek.

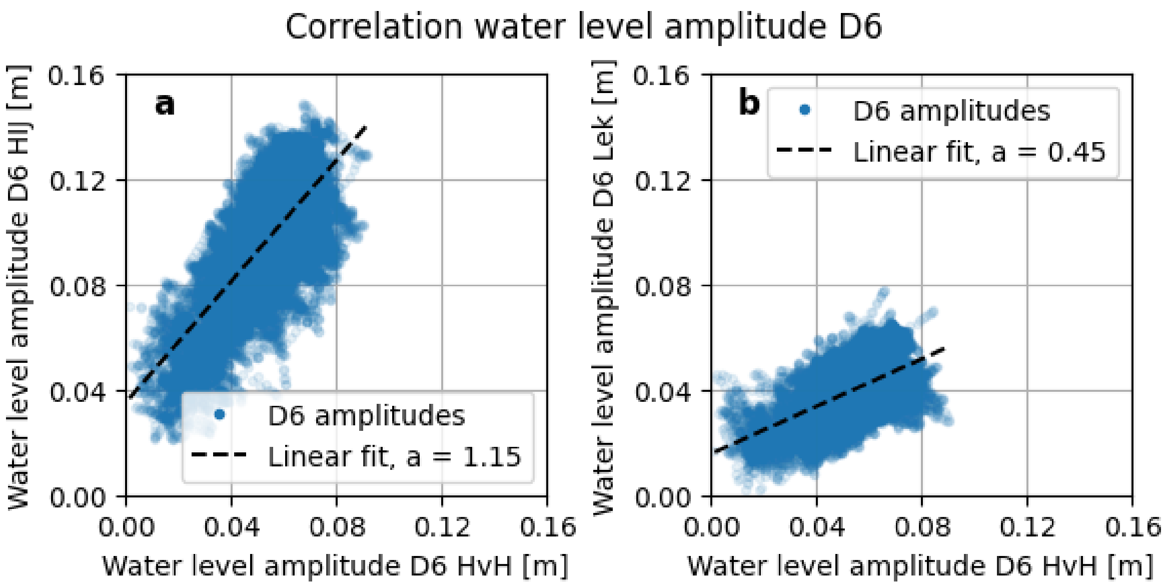

Figure D.3: Correlation between water level amplitudes of D6. **(a)** Amplitudes at Hoek van Holland and the end of the Hollandsche IJssel. **(b)** Amplitudes at Hoek van Holland and the end of the Lek.

E

Phase difference at the Hollandsche IJssel in analytical model RMD

This appendix shows the phase differences at the junction with the Hollandsche IJssel in the RMD scenario of the analytical model.

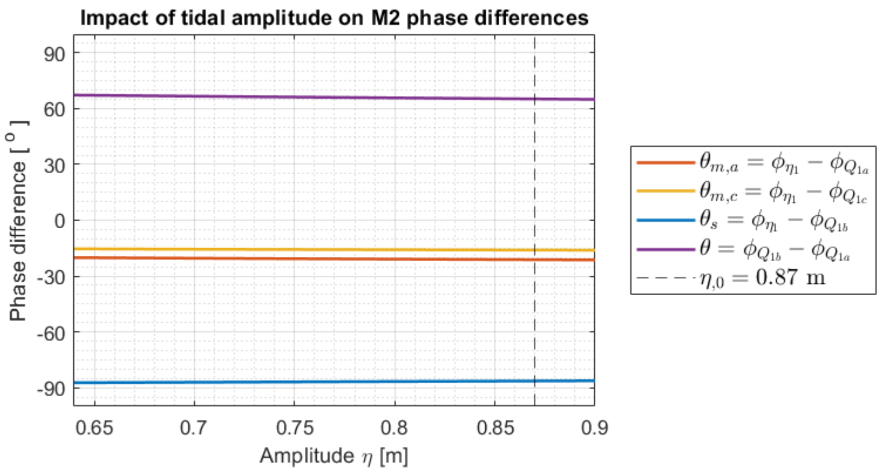

Figure E.1: Impact amplitude tide on phase difference at the Hollandsche IJssel in analytical model RMD

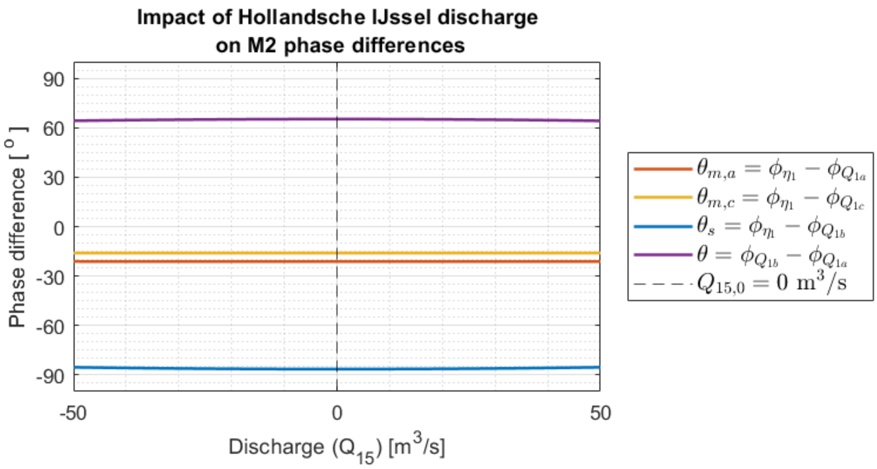

Figure E.2: Impact discharge Hollandsche IJssel on phase difference at the Hollandsche IJssel in analytical model RMD

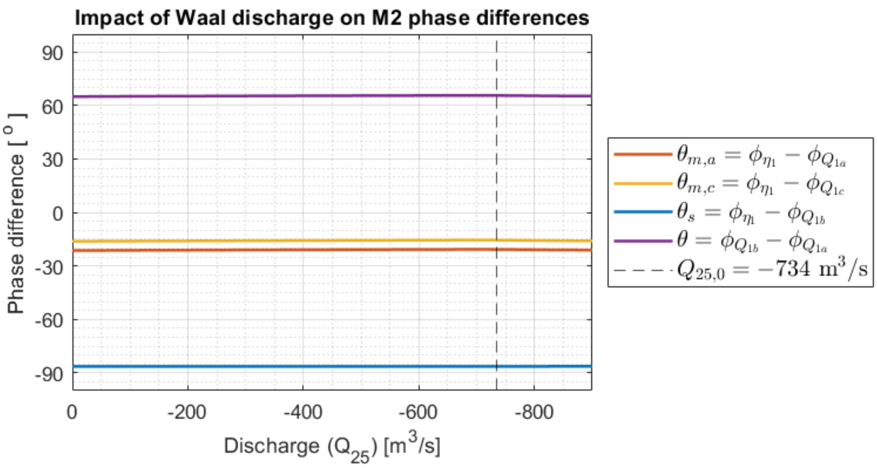

Figure E.3: Impact discharge Waal on phase difference at the Hollandsche IJssel in analytical model RMD

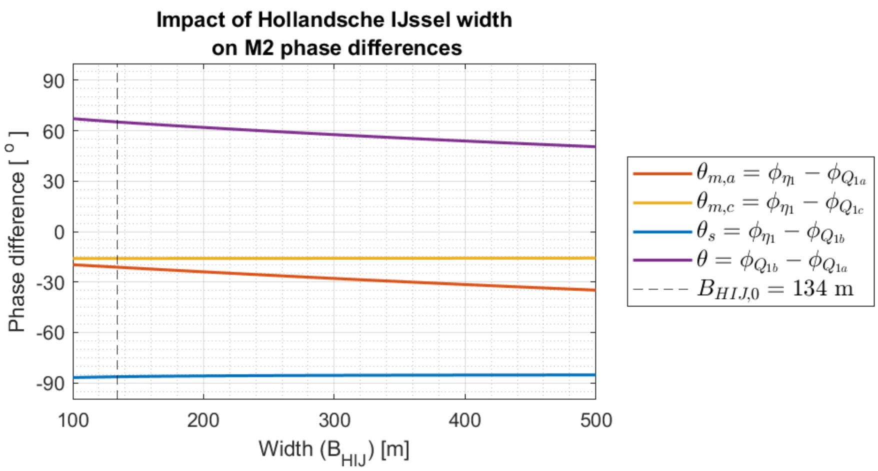

Figure E.4: Impact width on phase difference at the Hollandsche IJssel in analytical model RMD

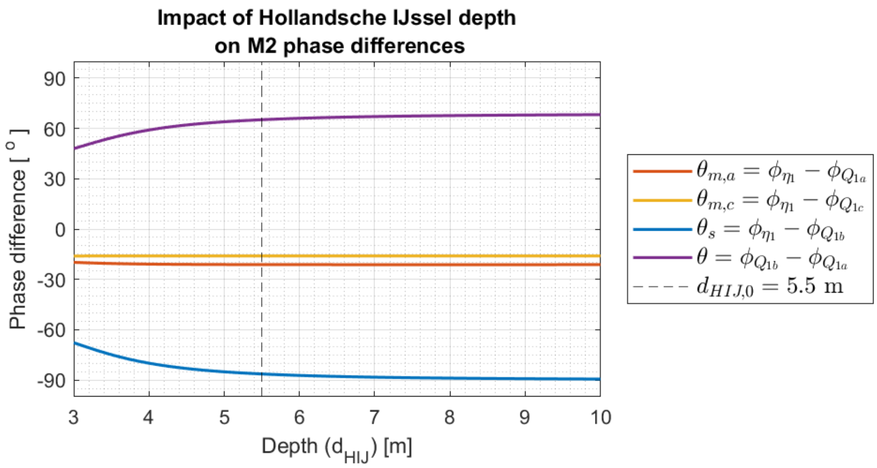

Figure E.5: Impact depth on phase difference at the Hollandsche IJssel in analytical model RMD

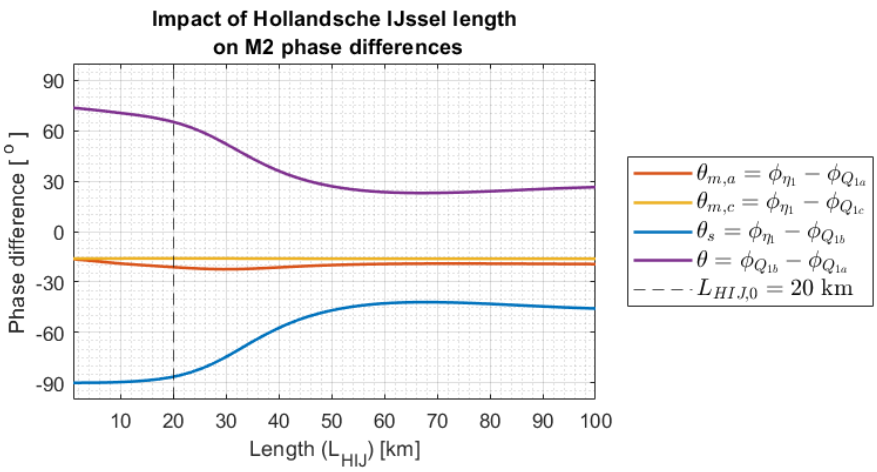

Figure E.6: Impact length on phase difference at the Hollandsche IJssel in analytical model RMD

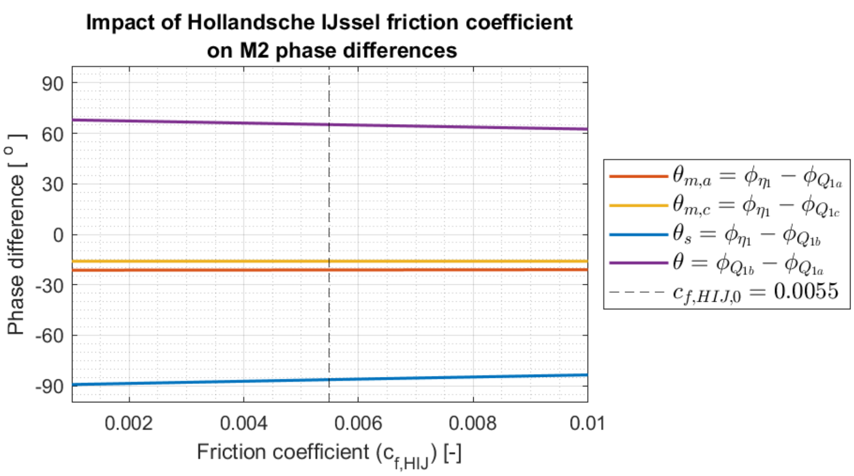

Figure E.7: Impact friction coefficient on phase difference at the Hollandsche IJssel in analytical model RMD

F

Phase difference at the Lek in analytical model RMD

This appendix shows the phase differences at the junction with the Lek in the RMD scenario of the analytical model.

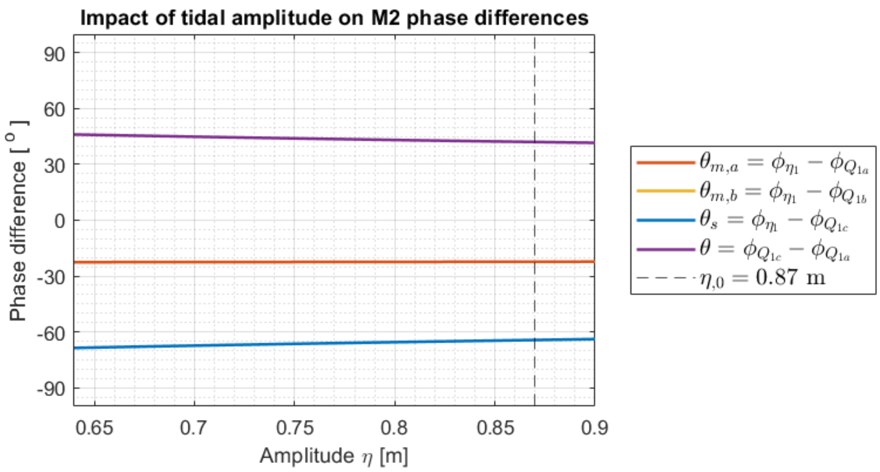

Figure F.1: Impact amplitude tide on phase difference at the Lek in analytical model RMD

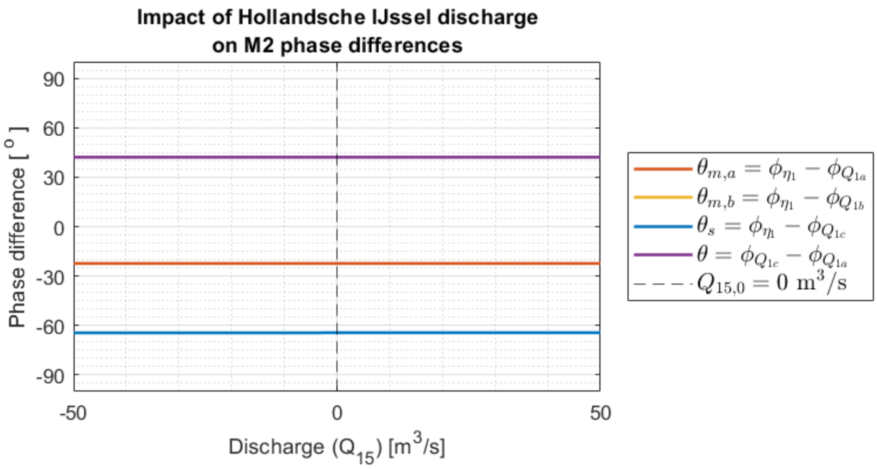

Figure F.2: Impact discharge Hollandsche IJssel on phase difference at the Lek in analytical model RMD

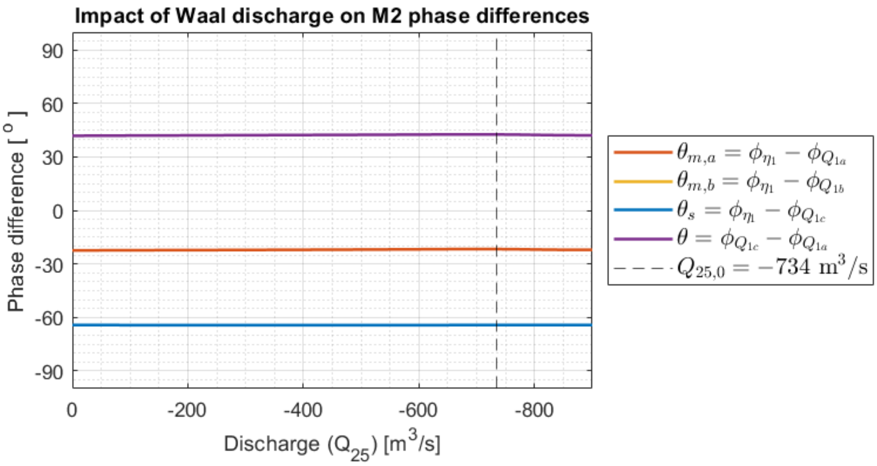

Figure F.3: Impact discharge Waal on phase difference at the Lek in analytical model RMD

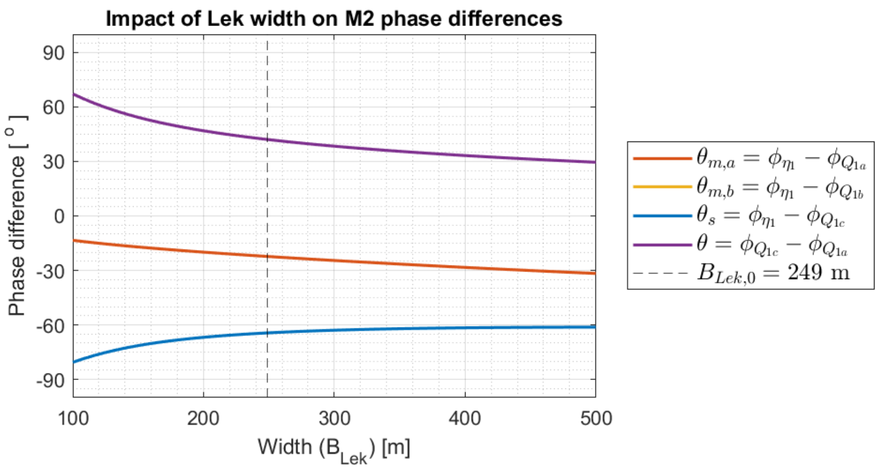

Figure F.4: Impact width on phase difference at the Lek in analytical model RMD

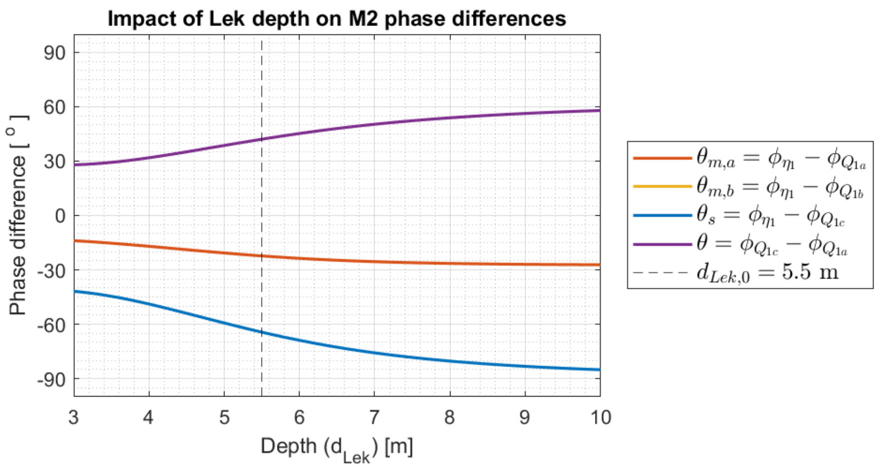

Figure F.5: Impact depth on phase difference at the Lek in analytical model RMD

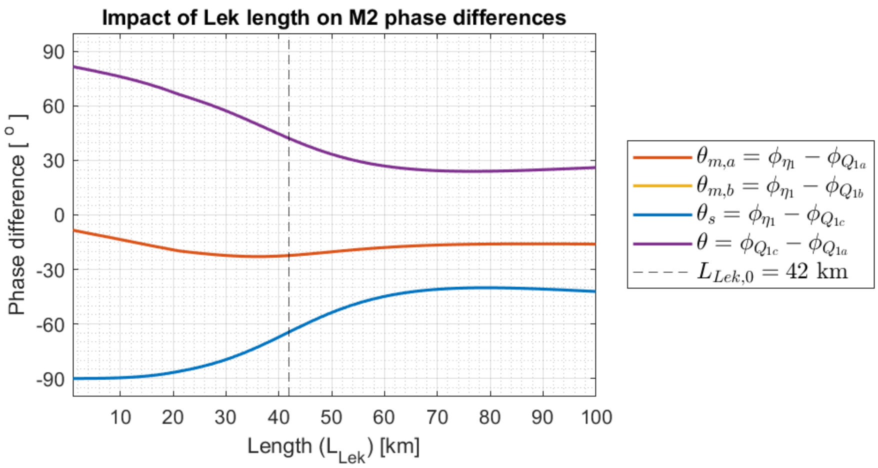

Figure F.6: Impact length on phase difference at the Lek in analytical model RMD

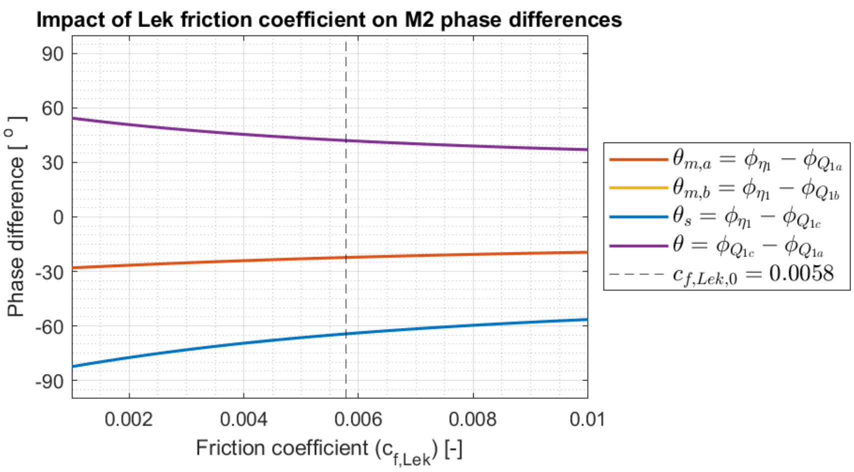

Figure F.7: Impact friction coefficient on phase difference at the Lek in analytical model RMD